



universität
wien

MASTERARBEIT

Titel der Masterarbeit

Time-dependent Galactic Winds

Verfasser

Daniel Steiner, Bakk.rer.nat BSc

angestrebter akademischer Grad

Master of Science (MSc)

Wien, 2012

Studienkennzahl lt. Studienblatt:

A 066 861

Studienrichtung lt. Studienblatt:

Masterstudium Astronomie UG2002

Betreuerin / Betreuer:

ao. Univ.-Prof. Dr. Ernst Dorfi

Abstract

Context. Galactic winds in the Milky Way are probably driven by cosmic ray particles. These particles will modulate the wind by resonant excitation of magnetohydrodynamic waves. A simple physical model based on a flux-tube geometry is introduced for determining the gas pressure, the cosmic ray pressure and the density 1 kpc above the outer disk (referred to as inner boundary of the galactic wind). Furthermore the influence of diffusion is discussed as well as the effect of different initial models.

Aims. The simulation of sequential supernova explosions will lead to a series of subsequent shock waves propagating outwards along the galactic wind. One goal is to investigate the scaleheight, at which the shocks are merging to a single strong shock, which enables particle acceleration by the first-order Fermi mechanism. Another aim is to examine and discuss the various flow features occurring to get a better insight in the physics of galactic winds.

Methods. An implicit hydrodynamical (HD) code will be used to simulate galactic wind flows within an adapted fluxtube geometry. The inner boundary conditions are modelled by using the so-called *Kompaneets approximation*, which is an analytical description of an expanding superbubble in an exponentially stratified atmosphere.

Results. The time-dependent shock structures (forward and reverse shock as well as a contact discontinuity) have been confirmed by using the implicit MHD code. Furthermore the merging scaleheight could be determined to be very close to the inner boundary (approximately 5 kpc). This is important to support the hypothesis of cosmic ray particle acceleration close to the inner boundary (lower halo), which is necessary to explain the observed high particle energies of $10^{17} - 10^{18}$ eV. The time evolution of the various shocks is also discussed in detail and shows clearly the merging process of the flow features. If galactic wind feedback on the properties of the inner boundary is considered, the galactic outflow will terminate as soon as the shocks are too weak to accelerate the gas. Noticeable is that the wind propagates further, if the undisturbed medium is assumed to be hydrostatic.

Conclusions. Supernovae explosions and its subsequent propagating shock waves are very likely to be the key process in understanding the observed cosmic ray (CR) energy spectrum.

Zusammenfassung

Kontext. Galaktische Winde in Galaxien mit normaler Sternentstehungsrate (z.B. die Milchstraße) können vermutlich mit Hilfe kosmischer Strahlung aus der Galaxie ausströmen. Diese Teilchen beeinflussen den Wind durch resonante Anregung von magneto-hydrodynamischen Wellen. Weiters wird ein einfaches auf einer Flussröhrengemetrie basierendes physikalisches Modell verwendet um den Gasdruck, den Druck durch kosmische Strahlung und die Dichte am inneren Rand des galaktischen Winds zu bestimmen. Zusätzlich wird der Einfluss verschieden starker Diffusion als auch die Abhängigkeit von verschiedenen Anfangsmodellen diskutiert.

Ziele. Die Simulation von zeitlich versetzten Supernova-Explosionen führt zur Ausbildung von mehreren aufeinander folgenden Schockwellen, welche sich entlang des galaktischen Windes in Richtung des Halos bewegen. Ein Ziel ist es eine Merging-Skalenhöhe zu definieren, in welcher sich die Schocks verbinden zu einer starken Stoßfront. Dieser Schock ist dann stark genug, um Teilchenbeschleunigung durch den Fermi-Prozess erster Ordnung zu gewährleisten. Ein weiteres Ziel ist die Untersuchung und Diskussion der auftretenden Wind-Features, um ein besseres Verständnis für die involvierte Physik zu bekommen.

Methoden. Ein impliziter hydrodynamischer (HD) Code wird verwendet, um den galaktischen Wind innerhalb einer bestimmten Flussröhrengemetrie zu simulieren. Die inneren Randbedingungen werden mit Hilfe der sogenannten *Kompaneets-Approximation* modelliert, welche eine analytische Beschreibung einer expandierenden Superbubble in einer exponentiell geschichteten Atmosphäre ist.

Ergebnisse. Die zeitabhängigen Schocks (vorlaufender und rücklaufender Schock sowie eine Kontaktdiskontinuität) werden sehr gut aufgezeigt und bestätigt vom verwendeten MHD Code. Weiters konnte die Merging-Skalenhöhe festgelegt werden (ungefähr 5 kpc). Dieses Ergebnis ist wichtig um die These zu stützen, dass die kosmischen Teilchen nahe der galaktischen Scheibe auf die erforderlichen und beobachteten Energien von $10^{17} - 10^{18}$ eV beschleunigt werden. Weiters wird die Zeitentwicklung der einzelnen Schocks ausführlich diskutiert und zeigt ganz klar, dass alle Schockfronten zusammenlaufen und sich zu einer Stoßfront verbinden. Bei Betrachtung der Rückwirkung des

galaktischen Windes auf die innere Randbedingung der Superbubble zeigt sich, dass die Schocks abschwächen und nach einiger Zeit verschwinden, welches ein Abflauen des galaktischen Windes zur Folge hat. Interessanterweise schafft es der Wind im Falle einer hydrostatischen Anfangskonfiguration, weiter auszuströmen als im Falle einer Wind-Anfangsverteilung.

Schlussfolgerung. Supernova-Explosionen und die daraus resultierenden Stoßwellen sind sehr wahrscheinlich der Schlüsselprozess, um die beobachtete Energieverteilung der kosmischen Strahlungspartikel zu verstehen.

Danksagung

Ich möchte mich zuallererst bei meiner Mutter bedanken, welche meine bereits in Kindersjahren erkennbare Faszination für Astronomie von der ersten Minute an gefördert und mich in den weiteren Jahren immer tatkräftig unterstützt hat.

Weiters möchte ich auch dem Betreuer meiner Masterarbeit, ao. Univ.-Prof. Dr. Ernst Dorfi, meinen herzlichen Dank aussprechen. Er hat sich Zeit genommen, meine unzähligen und nicht enden wollenden Fragen zu beantworten und mir damit sehr geholfen, Licht in die teils schwer verständliche Thematik zu bringen.

Im Laufe meines Studiums bin ich einigen Menschen begegnet, welche ich nun zu meinen Freunden zählen darf, und welche mich durch die vielen Diskussionen und Anregungen ein Stück näher zum Verständnis der Astronomie und Physik gebracht haben. Ihnen allen möchte ich hiermit herzlich danken!

Zum Abschluss möchte ich meine Freundin Magdalena erwähnen, welche mich auch während der teils arbeitsintensiven Zeit mit ihrer herzlichen und erwärmenden Art immer unterstützt hat. Ein großes Danke dafür!

Contents

1	Galactic Winds	1
1.1	Introduction	1
1.2	Physical Model for Galactic Winds	2
1.2.1	Interaction between the gas component and the magnetic field . .	3
1.2.2	Interaction between the CR component, gas component and the magnetic field and CR propagation	5
1.2.3	First-Order Fermi mechanism	6
1.3	Kompaneets Approximation	9
2	Physical Equations	19
2.1	Equations in Conservative Form	19
2.2	Equation of state	20
2.3	Continuity equation	21
2.4	Equation of motion	21
2.5	Equation of energy	22
2.6	Transport equation for cosmic rays	24
2.7	Energy exchange equation	24
2.8	Assumptions and simplifications	25
2.9	Galactic Gravitational Potential	26
2.10	Final Set of Equations	29
2.11	Fluxtube geometry	32
3	Numerical method	35
3.1	The grid equation	35
3.2	Artificial Viscosity	38
3.3	Discretization of the physical equations	42
3.3.1	Discretization of the volume term	44
3.3.2	Discretization of the advection term	45

3.3.3	Discretization of the continuity equation	45
3.3.4	Discretization of the equation of motion	48
3.3.5	Discretization of the gas energy density equation	50
3.3.6	Discretization of the cosmic ray energy density equation	50
3.3.7	Discretization of the wave energy density equation	51
3.4	Implicit method	51
3.4.1	Boundary Conditions	54
3.4.2	Structure and Inversion of the Jacobi-Matrix	57
4	Initial Model	61
4.1	Steady-state Initial Model	61
4.2	Pseudo-Variation of Boundaries	64
4.3	Quasi-hydrostatic initial model	66
5	Results	69
5.1	Flow structure	69
5.1.1	Flow features	69
5.2	Dependence on the diffusion coefficient	76
5.2.1	Time evolution of shock fronts	82
5.3	Feedback of the wind on the superbubble	88
6	Numerical difficulties and conclusion	95
6.1	Numerical difficulties	95
6.2	Conclusions	96
	Bibliography	99

1 Galactic Winds

1.1 Introduction

In recent decades galaxies had been popular objects of research. Especially the issue of *galaxy formation and evolution* fascinated astrophysicists and is still not understood in all details. Gravity is responsible for the largest structures one can observe in present days, but on galactic scales, the gravitational force is *not the only important force* to take into account when making models which should explain the various observed features of galaxies. Even inclusion of *cold dark matter* could not explain features like galactic outflows. Nowadays a change of thinking has begun and different physical processes, e.g. *star formation and evolution* or chemical evolution of the interstellar medium (ISM), are taken into account in treating the issues of galaxies. Veilleux et al. (2005) argue that the progress of development of new theoretical and numerical galactic wind models is slow because of the need for comprehensive data (in sensitivity and spatial resolution) of the full electromagnetic spectrum. These data are essential for the further improvement of the models.

When a starburst with large outflows was detected in the galaxy M82 (see Lynds & Sandage (1963)), the topic of galactic winds (GWs) became even more interesting and was since then considered as the *dominant feedback in galaxy formation and evolution* (Veilleux et al. (2005)). From this time on various models have been created, which try to explain these galactic outflows (e.g Burke (1968); Johnson & Axford (1971); Mathews & Baker (1971)), and it was found that mass outflows only occur, if the temperature of the gas is sufficiently high(Breitschwerdt et al. (1991)). The problem is that most of the recent galactic wind models are only treating galactic winds as *single-component-fluids*, saying that just the effects of the ejected gas like *radiative cooling* are taken into account and therefore only the *thermal pressure* is driving the wind. These high-temperature winds are therefore so-called *thermally-driven* winds and are assumed to have flow structures showing that the gas is ejected with high kinetic energy until dense

clumps are formed due to radiative cooling. These dense structures then fall back to the galactic disk (so-called *galactic fountains*, see Kahn (1981), Kahn (1991) and Kahn (1998) for further reading). As a result the halo around galaxies becomes inhomogeneous (see Figure 1.3). However, such winds are only expected to occur in galaxies with *active galactic nuclei* (AGN) or in galaxies with *very high gas temperatures*, e.g. in starburst galaxies.

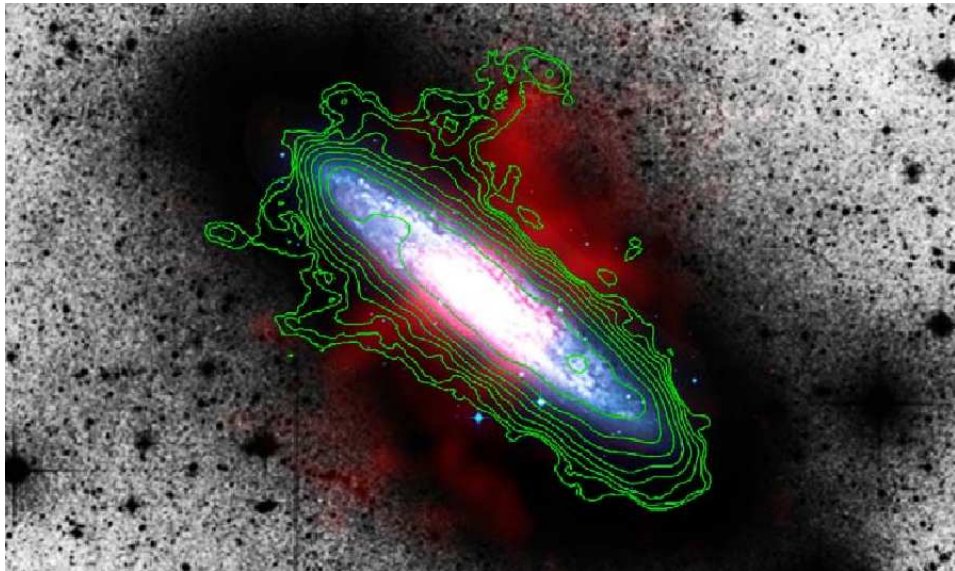


Figure 1.1: *H I* contours over a multi-wavelength picture of the galaxy NGC 253. The contours reveal denser regions (clumps), which were created by a galactic outflow. Several of these clumps are very likely to fall back to the galactic disk as galactic fountains (the picture is taken from Boomsma et al. (2005)).

The next step on the path of a better understanding of galactic winds had been taken, when for the first time the effects of *cosmic rays* (CRs) were included in the dynamical galactic wind equations (Ipavich (1975)). With accounting for this newly considered component, the temperatures needed to drive a wind significantly dropped. This is possible, because CRs can transfer a sufficient amount of momentum to the gas to escape from the galaxy, even if the gas is cold. Nevertheless, the calculations of that model had been carried out in a spherical geometry with the galaxy itself assumed as a point source of mass and energy. Furthermore no coupling between the CRs and the gas had been taken into account. The model used in this thesis picks up the idea of Breitschwerdt et al. (1991); de Aveliz & Breitschwerdt (2005); Dorfi & Breitschwerdt (2012), this means it takes the geometry of the wind-flow structure into account (the so-called fluxtube geometry, see section 2.11) as well as the coupling between the three

main components of the galactic wind, namely the *gas component*, the *cosmic rays* and the *magnetic wave field*. These interactions are briefly reviewed in the following section 1.2.

1.2 Physical Model for Galactic Winds

A justification for incorporating CRs in the galactic wind model can be obtained by consideration of observations of electromagnetic spectra e.g. (of the Milky Way). It has been shown (see Everett et al. (2008) for details) that a cosmic ray driven wind leads to the best fits in explaining the observed spectra (compare with Figure 1.2).

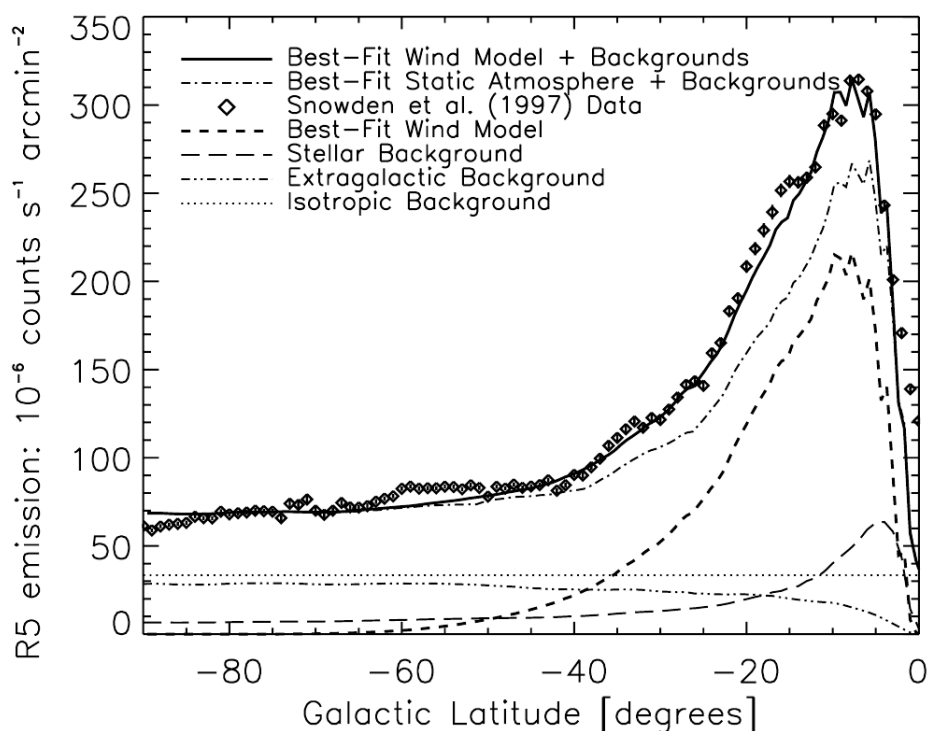


Figure 1.2: *H I* contours over a multi-wavelength picture of the galaxy NGC 253. The contours reveal denser regions (clumps), which were created by a galactic outflow. Several of these clumps are very likely to fall back to the galactic disk as galactic fountains (the picture is taken from Boomsma et al. (2005)).

The magnetic field modulates the gas flow pattern of the (ionized) gas flow, more precisely the plasma and the magnetic field affect each other, therefore galactic winds should be treated magnetohydrodynamicall. Further CRs are charged particles, which start to gyrate along the magnetic field and hence inducing small perturbations to the magnetic

field (so-called *Alfvén waves*), which in turn interact with the CRs and the gas component. In the physical model described in section 1.2, the interaction of the magnetic field on the plasma is not be considered, but the small perturbations of the magnetic field (already introduced as magnetic wave field) are treated as an additional pressure component, which interacts with the CR pressure.

1.2.1 Interaction between the gas component and the magnetic field

The magnetic field is assumed to be 'frozen' in the gas. This is due to the fact, that the *mean magnetic energy density* is much *lower* than the *thermal gas energy density* in large-scale magnetic field structures like in the halo of galaxies (for details see Ehle et al. (1998)). On the other hand the kinetic energy of the galactic wind is dominant with respect to the magnetic energy, which is resulting in frozen magnetic field lines. These magnetic field structured can be traced observationally and therefore are providing a good tool for studying the kinematics of galactic winds.

Close to the galactic mid-plane the magnetic field has a component parallel to the disk. It has been shown in 3D-MHD simulations (for detail, see de Avezil & Breitschwerdt (2005)), that the magnetic field parallel to the galactic disk cannot prevent hot gas (especially created by supernovae) from streaming into the galactic halo. Moreover the simulations showed, that the gas outflow into the halo is nearly as high as it would be without having a magnetic field.

1.2.2 Interaction between the CR component, gas component and the magnetic field and CR propagation

The CR particles are treated as a *rarefied plasma*, which interacts with the magnetic field by gyrating along its field lines. The assumption of considering CRs as a plasma can be explained and justified by taking a process into account named *pitch-angle scattering*. The pitch-angle of CRs is changed, if the magnetic field is perturbed by e.g. motion of the gas (see Figures 1.4 and 1.5). The variation of this pitch-angle can cause the CRs to change their propagation (from parallel to antiparallel and vice versa) along the magnetic field. Because of this it is legitimate to say that the CRs are distributed isotropic with respect to such perturbations of the magnetic field (denoted as 'Alfvén-wave frame' in Breitschwerdt et al. (1991)). Such Alfvén waves are propagating along the magnetic

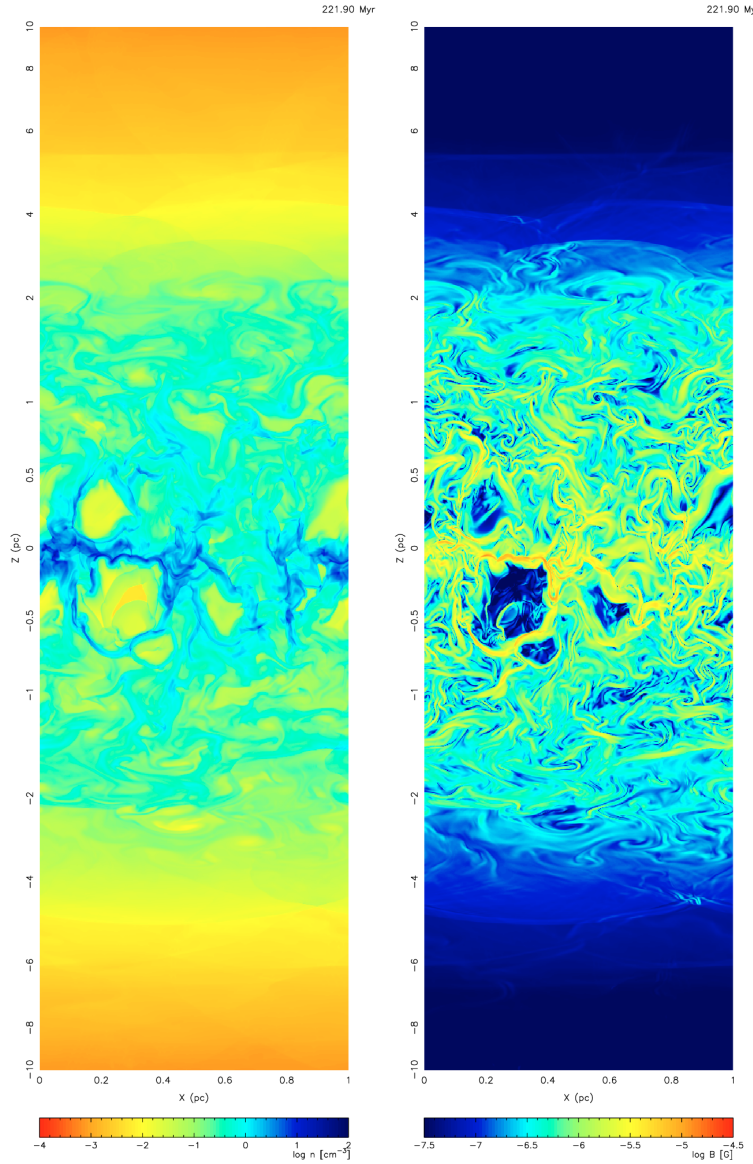


Figure 1.3: The left panel is showing the vertical (perpendicular to the galactic disk) density distribution. Expanding superbubbles can be seen very clearly. The right panel is showing the magnetic field map, which reveals magnetic field structures which also have a component perpendicular to the galactic disk and therefore facilitate outflows like galactic fountains or galactic winds (picture taken from de Avillez & Breitschwerdt (2005)).

field lines with the *Alfvén speed* \mathbf{v}_A (with respect to the motion of the background gas flow \mathbf{u}),

$$\mathbf{v}_A := \frac{\mathbf{B}}{\sqrt{4\pi\rho}}, \quad (1.2.1)$$

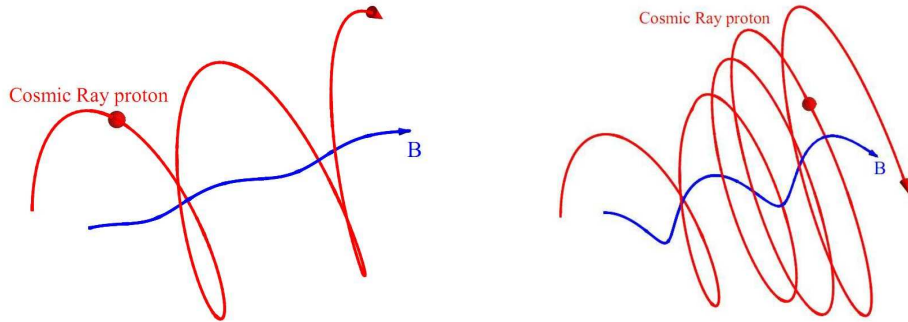


Figure 1.4: CR particle gyrating along a unperturbed magnetic field line (taken from Everett (2009)).

Figure 1.5: Pitch angle of CR particle changes, if the magnetic field is perturbed (taken from Everett (2009)).

where ρ is the gas density. The Alfvén-waves are preferentially propagating away from the galactic disk (outwards). Resonant excitation of Alfvén-waves by the CRs themselves actually leads to a confinement of CRs particles to the Alfvén waves, a so-called *Alfvénic drift* (for details and the derivation of these results see Skilling (1975); Cesarsky (1980)). In other words, one can say that CRs effectively are convected outwards with the speed $(\mathbf{u} + \mathbf{v}_A)$. Furthermore the Alfvén-waves act (as already argued) as the center of pitch-angle scattering processes. Having a cosmic ray pressure gradient ∇p_c , then a fraction of CR flux is also due to diffusion down the gradient. In summary it can be said that one is able to distinguish two different components, which add to the overall CR motion,

- *convective motion* due to confinement of CR particles to the Alfvén wave frame (gas flow + Alfvénic drift),
- *diffusion* down the CR pressure gradient.

cosmic ray particles also are influencing the magnetic field due to the so-called *Parker instability* (Parker (1966)). This instability causes the magnetic field parallel to the galactic disk to inflate and to form Ω -shaped structures. Note that this is a completely different process than the opening of field lines due to gas-flow motion caused by supernovae, nevertheless it facilitates the outflow of gas into the galactic halo.

1.2.3 First-Order Fermi mechanism

The first-order Fermi mechanism is the assumed process to accelerate the CRs which are created by e.g. supernovae up to speeds, which are sufficiently high to drive galactic

winds. The original idea has been developed by Fermi (1949). In the presence of strong shock-waves the first-order Fermi mechanism is also referred to as *diffusive shock acceleration*.

Energy gain of CR particles

Subsequently the diffusive shock acceleration is briefly explained. The following assumptions are necessary for ensuring the applicability of the Fermi process:

- A *strong shock* is assumed (e.g. supersonic shells of expanding supernova remnants), this means that the two densities ρ_1 and ρ_2 before and after the shock ¹ are connected by the following relation (γ_g denotes the adiabatic index of the gas),

$$\frac{\rho_2}{\rho_1} = \frac{\gamma_g + 1}{\gamma_g - 1} . \quad (1.2.2)$$

- The CR particles are assumed to have speeds close to the speed of light c . This ensures that the shock velocity U is much lower than those of the particles.
- Due to the high particle velocity, the gyration radius along the magnetic field lines can be assumed to be *much bigger than the thickness of the shock*, in other words the particles 'feel' the shock-front as an infinitesimally thin layer.
- Turbulent motion on both sides of the shock-front as well as streaming instabilities are taken as the justification for assuming an *isotropic velocity distribution on both sides of the shock*.

With these assumptions, the process (schematically) takes place as sketched in Figure 1.6 (following the explanations in Longair (2011), p. 570):

- a) The velocity of a strong shock is characterized as being *highly supersonic*. In the frame of the shock-wave the gas upstream flows through the shock front with velocity $u_1 = U$. Due to conservation of mass (see section 2.3) the following expression must hold ²,

$$\rho_1 u_1 = \rho U = \rho u_2 . \quad (1.2.3)$$

¹Note that in this section the subscript "1" denotes quantities *upstream* and "2" corresponds to quantities *downstream*.

²In Figure 1.6, the gas velocities are denoted differently, namely $u_{1,2} \rightarrow v_{1,2}$.

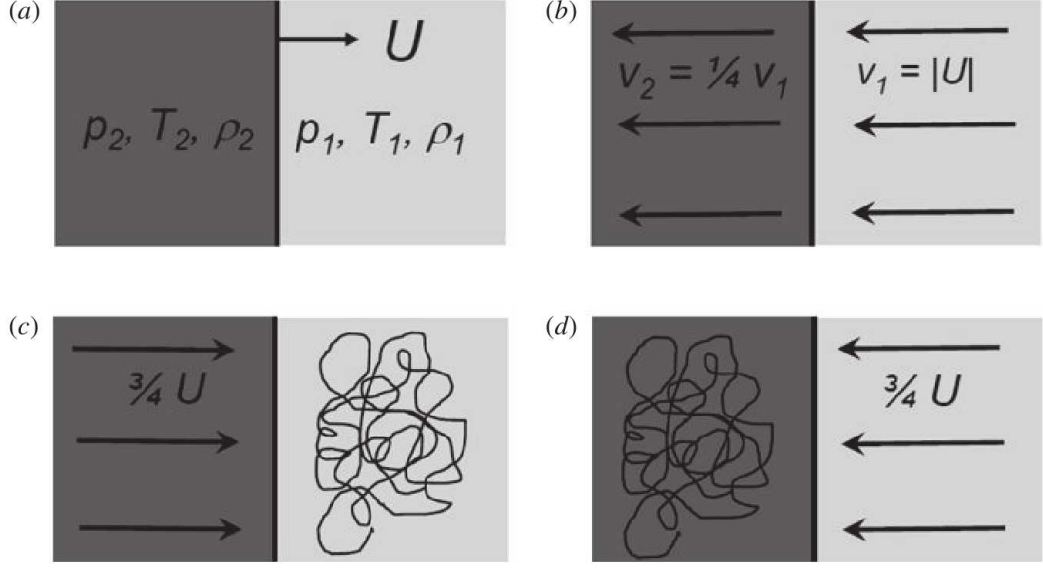


Figure 1.6: Sketch of the First-order Fermi mechanism, when a strong shock wave is assumed (picture taken from Longair (2011)).

- b) For a non-relativistic mono-atomic gas the adiabatic index is $\gamma_g = \frac{5}{3}$. Then, by using the properties of a strong shock (1.2.2), the following relation is obtained,

$$\frac{\rho_1}{\rho_2} = 4, \quad (1.2.4)$$

$$u_2 = \frac{1}{4}u_1. \quad (1.2.5)$$

- c) Now the whole system is again transformed into the system of the particles upstream, where the gas is at rest. Due to the made assumptions, the distribution of CR particles upstream is isotropic. If a particle crosses the shock-front due to scattering, it 'sees' the moving gas downstream as explained in b). This gas moves with $\frac{3}{4}U$ with respect to the material upstream, and therefore the CR particle *gains a small amount of energy*.
- d) Finally a last transformation into the frame of the gas downstream is performed. Due to the same scattering processes as upstream, the CR particles there are distributed isotropic too. In this system of reference the gas upstream flows towards the gas downstream again with a velocity $\frac{3}{4}U$. A particle which crosses the shock-front therefore also gains energy. This is the crucial feature of the first-order Fermi mechanism, because the particles *only gain and never loose energy*, when they are

crossing the shock front.

The energy gain can be calculated by taking into account that the CR particles are relativistic. Then the resulting equation can be written as (see Longair (2011)),

$$p_{CR} = \frac{E_{CR}}{c}, \quad (1.2.6)$$

$$\Delta E = p_{CR} \frac{3}{4} U, \quad (1.2.7)$$

where p_{CR} is the relativistic momentum of the CRs and ΔE is the energy gain after crossing the shock-front. The energy gain clearly also depends on the angle θ of the particles with respect to the shock. Only particles which are scattered into $0 \leq \theta \leq \frac{\pi}{2}$, can cross the the shock. After averaging over all of these possible directions and taking into account, that this energy fraction is gained twice, one obtains,

$$\left\langle \frac{\Delta E}{E} \right\rangle = \frac{U}{c}. \quad (1.2.8)$$

Escape Probability

Another question is, how long the particles are scattered from upstream to downstream and vice versa, before they can escape. For this purpose a result from *classical kinetic theory* is used as it has been proposed by Bell (1978). Then the average number of particles, which are crossing the shock-front on each side, can be estimated by $\frac{1}{4} N c$, where N denotes the number of particles upstream. Because the region downstream is slower than the shock-front by a value of $\frac{1}{4} U$, some of the CR particles are adventured away from the shock region. Then the number of 'lost particles' is clearly determined by the number of particles in the region multiplied by velocity difference, especially it has the value $\frac{1}{4} U N$. Thus the average rate of lost particles with respect to particles, which are crossing the shock-front, takes the value (see Bell (1978); Longair (2011) for details),

$$\frac{\frac{1}{4} N U}{\frac{1}{4} N c} = \frac{U}{c}. \quad (1.2.9)$$

This escape probability per crossing cycle clearly is very low, since the shock velocity is not relativistic.

Finally it should be noted that this is a simplified version of the first-order Fermi

mechanism. A full treatment requires to solve the so-called *Fokker-Planck equation*, which describes the evolution of the CR energy spectrum (see e.g. Axford et al. (1977); Blandford & Ostriker (1978) and Krymskii (1977)).

1.3 Kompaneets Approximation

This section deals with the issue of describing the evolution of a *superbubble*, which is assumed to be the precursor of the cosmic ray driven winds discussed in this thesis. The aim is to develop an approximate theory of an expanding superbubble, which provides *physically motivated initial values* of the gas energy density E_g , the cosmic ray energy density E_c and the initial fluxtube cross-section A_0 . A hydrodynamic treatment of this problem would be far too much effort, since the model could not take any advantages of the improved accuracy and spatial resolution due to the various simplifications (e.g. the 1D-treatment of the problem, the simple fluxtube geometry).

Hence it is sufficient to use an approximate approach as it has been made by Kompaneets (1960). He found an *implicit description* of (adiabatic) shock-waves propagating through a *exponentially stratified* medium,

$$\rho(z) = \rho_0 e^{-z/h_z} , \quad (1.3.1)$$

where ρ_0 is the density at the explosion center of the supernova and h_z is the stratification scaleheight. The following assumptions are made in the Kompaneets approximation:

- A strong, non-radiative (adiabatic) shock is assumed (compare with equation (1.2.2)).
- The post-shock pressure $P_S(t)$ should be uniform all over the surface of the superbubble.
- The atmosphere is hydrostatically (exponentially) stratified.

Then the *Hugoniot conditions* (details e.g. in Anderson (1963)) can be used to determine the *normal component of the expansion velocity of the shock-front* U at every position z above the galactic mid-plane (see Bisnovatyi-Kogan & Silich (1995)),

$$U(z, t) = \sqrt{\frac{\gamma_g + 1}{2} \frac{P_S(t)}{\rho(z)}} \stackrel{(\gamma_g \Rightarrow 5/3)}{\Rightarrow} P_S(t) = \frac{4}{3} \rho(z) U(z, t)^2 . \quad (1.3.2)$$

Using now equation (1.3.1) and the assumption, that P_S shall be uniform all over the shock-front, an expression for the shock velocity U is obtained (compare with Maciejewski W. (1998)),

$$U(z, t) = U_0(t)e^{z/(2h_z)} , \quad (1.3.3)$$

where U_0 denotes the shock-front velocity at the explosion site. Due to the exponential stratification, the velocities $U(z_L, t) := U_L(t)$ and $U(z_H, t) := U_H(t)$ will have different values (z_L and z_H denote the low and high density extrema, respectively; also compare with Figure 1.7). Following the approach of Maciejewski W. (1998), the rate of expansion

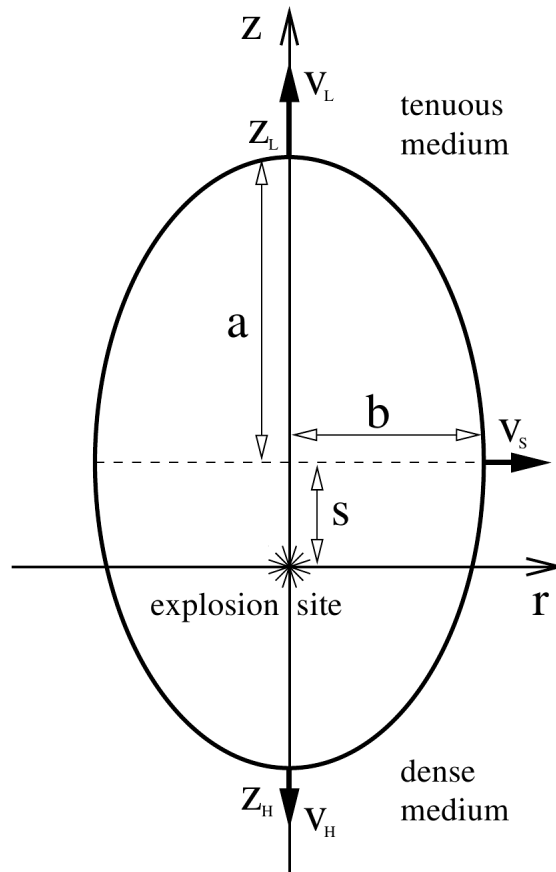


Figure 1.7: Schematic view of the superbubble as assumed in the Kompaneets approximation (picture taken from Maciejewski W. (1998)).

of the superbubble perpendicular to the galactic plane \dot{a} (a denotes the major half-axis)

can be calculated rather easy as the *mean value of the expansion velocities* U_L and U_H .

$$\dot{a} = \frac{U_L + U_H}{2} = U_0(t) \frac{e^{z_H/(2h_z)} + e^{z_L/(2h_z)}}{2} . \quad (1.3.4)$$

Because the expansion of the superbubble is dependent on the height z , a displacement s of the explosion center will occur. The expansion rate \dot{s} can be calculated by straightforward geometrical arguments,

$$\dot{s} = \frac{U_L - U_H}{2} = U_0(t) \frac{e^{z_L/(2h_z)} - e^{z_H/(2h_z)}}{2} . \quad (1.3.5)$$

The expansion of the minor half-axis is determined only by using (1.3.3) and the fact that $z = s$ for b ,

$$\dot{b} = U_0(t) e^{s/(2h_z)} . \quad (1.3.6)$$

Then, by merging (1.3.4), (1.3.5) and (1.3.6), the unknown variable $U_0(t)$ can be eliminated and the following expressions are obtained,

$$\frac{da}{db} = \cosh \frac{a}{2h_z} , \quad (1.3.7)$$

$$\frac{ds}{da} = \tanh \frac{a}{2h_z} , \quad (1.3.8)$$

and after subsequent integration the final relations are given by (compare with Maciejewski W. (1998)),

$$\tan \frac{b}{2h_z} = \sinh \frac{a}{2h_z} , \quad (1.3.9)$$

$$\exp \frac{s}{2h_z} = \cosh \frac{a}{2h_z} . \quad (1.3.10)$$

These equations give some insight about the evolution of the shock-shape, like the flattening b/a or the lateral size b . Nevertheless, the derivation of the shape itself needs some further discussions. In the original paper (Kompaneets (1960)), the form of the shock-wave can be written in cylindrical coordinates (r, ϕ, z) as follows,

$$V(t) = \pi \int_{z_1}^{z_2} r(z, t)^2 dz , \quad (1.3.11)$$

where $r(z, t)$ is the distance from the origin (explosion site) and dependent on the height

z . Kompaneets then succeeded in finding an implicit solution for describing the shape of the superbubble. The implicit nature of the equation is with respect to the dependence on time t , since an integral is needed to get an explicit expression for t (see for details e.g. Bisnovatyi-Kogan & Silich (1995)),

$$r(z, y) = 2h_z \arccos \left\{ \frac{1}{2} \exp \left(\frac{z}{2h_z} \right) \left[1 - \frac{y^2}{4h_z^2} + \exp \left(\frac{-z}{h_z} \right) \right] \right\}. \quad (1.3.12)$$

The variable y is the transformed time variable, which is responsible for the implicit dependence from time and is given by,

$$y(t) = \int_0^t \sqrt{\frac{\gamma_g^2 - 1}{2} \frac{E_0}{\rho_0 V(t')}} dt'. \quad (1.3.13)$$

The resulting shape is plotted afterwards in Figure 1.8 for various values of y and for a stratification scaleheight $h_z = 80$ kpc, revealing the expanding structure of the shock-front. The problem with the time dependence as given in (1.3.13) is the dependence on the volume, which again depends on the time-dependent radius $r(z, t)$ (1.3.12). Hence, obtaining the time which is connected to a certain y requires to *first* choose a value for r and afterwards calculating the time y .

There is a way how to circumvent this problem. The idea is that the shock shape of the Kompaneets approximation is virtually indistinguishable from an ellipsoid (the true shape is a boxy ellipsoid, compare with Figure 1.8), as suggested by Maciejewski W. (1998). Hence the volume of the superbubble $V(t)$ can be approximated by writing,

$$V(t) = \frac{4}{3} \pi a b^2, \quad (1.3.14)$$

where a and b are the major and minor half-axis of the ellipsoid, respectively. Then the post-shock pressure P_S can be written in the following terms (see Bisnovatyi-Kogan & Silich (1995); Maciejewski W. (1998)),

$$P_S = \frac{4\pi\zeta^5}{25} \frac{E}{V(t)}. \quad (1.3.15)$$

In this equation, $\zeta = 2.025$ is a constant which follows from the energy integral of the Sedov-solution (details on this in Sedov (1958)) and E is the energy of the supernova(e). Then, by using equation (1.3.2) and equation (1.3.1) and using the fact that the expan-

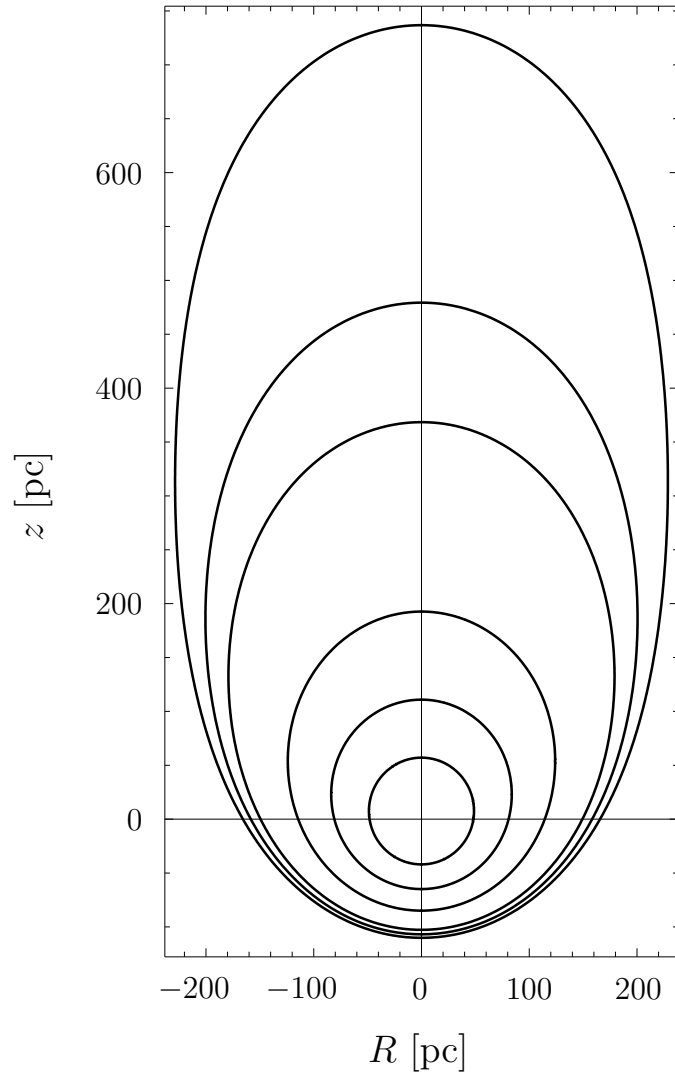


Figure 1.8: Expanding shock-waves according to the Kompaneets solution (plotted with MATHEMATICA).

sion velocity U for $z = s$ is given by \dot{b} (compare with equation (1.3.6) and Figure 1.7), one can write,

$$\rho_0 e^{-s/hz} \dot{b}^2 = \frac{4\zeta^5}{25} \frac{E}{ab^2}, \quad (1.3.16)$$

and by expressing b and s in terms of a (see equations (1.3.5) and (1.3.6)) the final expression for the *explicitly* time-dependent major half-axis is obtained after integration (Maciejewski W. (1998)),

$$t(a) = \zeta^{-5/2} \left(\frac{E}{\rho_0} \right)^{-1/2} (2h_z)^{5/2} I \left(\frac{a}{2h_z} \right), \quad (1.3.17)$$

$$I(x) := \frac{5}{2} \int_0^x dy \frac{\sqrt{y}}{\cosh^2 y} \arctan(\sinh(y)) \approx \frac{3x^{5/2}}{3 + 2x^{5/2}}. \quad (1.3.18)$$

This procedure is only directly applicable for a *fixed supernova energy* E . In this thesis it is assumed that the stars of an OB-association, existing of *more than one star*, are successively exploding and hence supplying energy and momentum to drive the superbubble expansion. For this purpose it is assumed, that the supernovae are exploding in *equidistant* time intervals over a certain period. The expansion of the wind then clearly has to be modified, since the energy is not supplied instantly, but spread over a certain time. The following steps are made for modifying the time evolution of the major half-axis in the case of more than one supernova:

- In the case of one single supernova the superbubble expands according to (1.3.17), until the next supernova explodes after the time dt .
- Two supernovae clearly lead to a greater expansion speed, therefore (1.3.17) is used, but with E being twice the energy of one supernova, namely $E = 2E_{SN}$ (see Figure 1.9).
- This procedure is repeated, until the superbubble has expanded to a certain reference level out of the galactic disk. At this level the quantities E_g and E_c are calculated and used as initial inner boundary values for the galactic wind.

Furthermore it can be seen by analysis of (1.3.17), that $a \rightarrow \infty$ in finite time. This is called *blow-out*, because the superbubble accelerates rapidly due to the exponential stratification of the ambient gas. Hence the application of the procedure above must be handled with special care (it is possible that a blow-out occurs inbetween $[(i-1)dt, i dt]$ and must be taken into account).

Applicable parameters for modelling the Kompaneets approximation for the Milky Way galaxy are chosen as follows,

- scaleheight $h_z = 80 \text{ kpc}$,
- number density of the ambient gas at the explosion site $n_0 = 3 \text{ cm}^{-3}$.

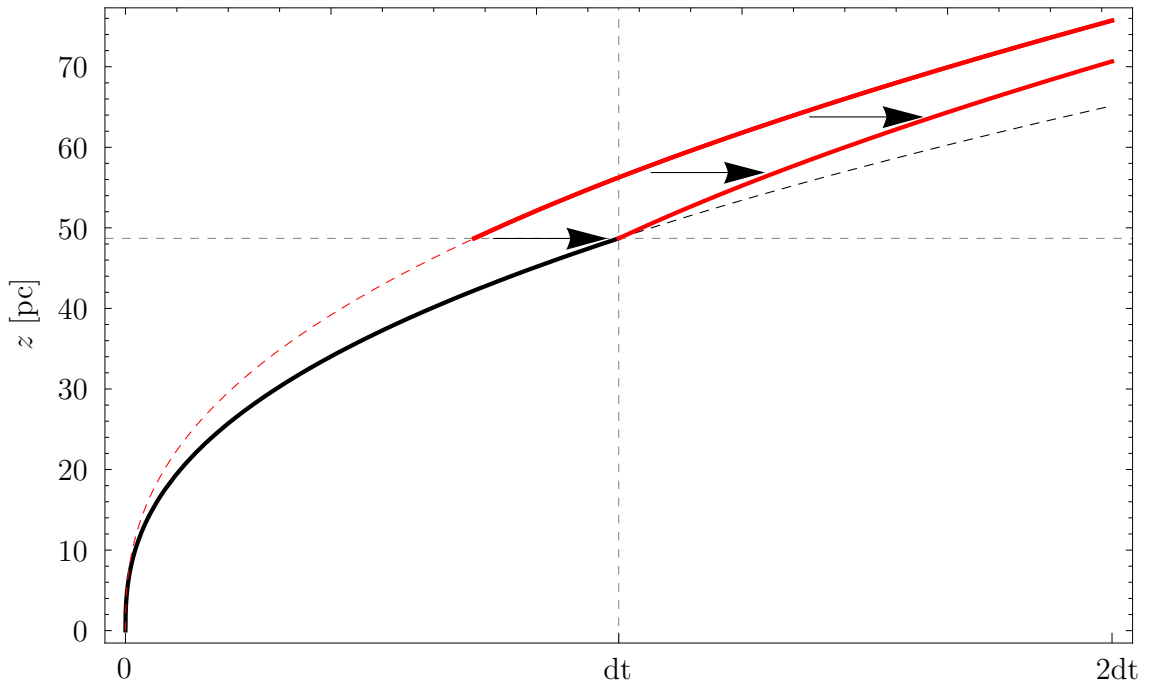


Figure 1.9: The black line corresponds to the expansion of the major half-axis a in the case of a single supernova. The red lines correspond to the expansion in the case of two supernovae. The full lines represent the true expansion, the dashed lines the expansions if there were no successive explosions of supernovae. The arrows indicate, that the red full line must be moved in a way, that the expansion remains continuous. This procedure is repeated for every additional supernova explosion (plotted with MATHEMATICA).

These values are based on the basis of the values taken by other authors for modelling the *Local Bubble*, e.g. in Breitschwerdt et al. (2009). The values taken there are $n_0 = 10 \text{ cm}^{-3}$ and $h_z = 70 \text{ kpc}$, which are of the same order as the values taken in this thesis. The somewhat lower density is chosen after comparison with other results, which suggest slightly lower values for n_0 (compare e.g. with Downes & Guesten (1982)). With the chosen parameters the full expansion diagram for $a(t)$ takes the following form (Figure 1.10).

The fixed value for a after approximately $10.3 dt$ is due to the fact, that from this time on, the galactic wind is assumed to have started and the cavity which has been swept out by the superbubble, is hold constant. This can be justified physically by arguing that before starting the galactic wind the energy provided by the supernova explosions is 'used' to sweep up all the surrounding material, and in later times, after the blow-out, this energy is *advected away* from the galactic disk by a wind. The reference

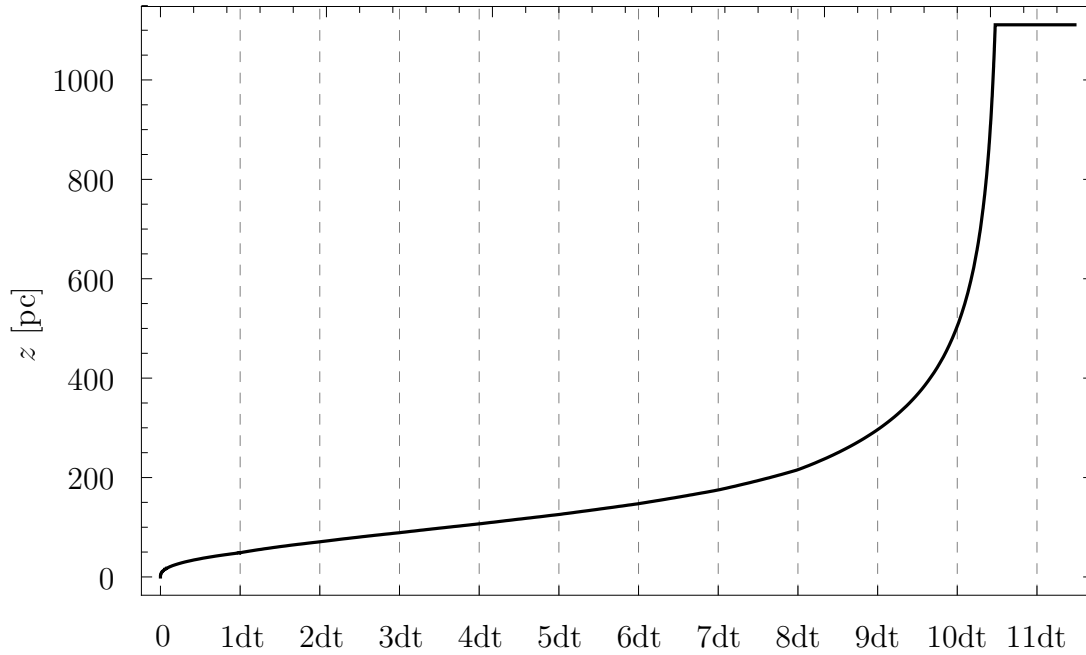


Figure 1.10: Expansion profile for the major half-axis $a(t)$ of the Kompaneets ellipsoid (plotted with MATHEMATICA).

level is given at $z_0 = 1$ kpc, which is in accordance with Breitschwerdt et al. (1991) and Dorfi & Breitschwerdt (2012) (compare with Figure 1.11).

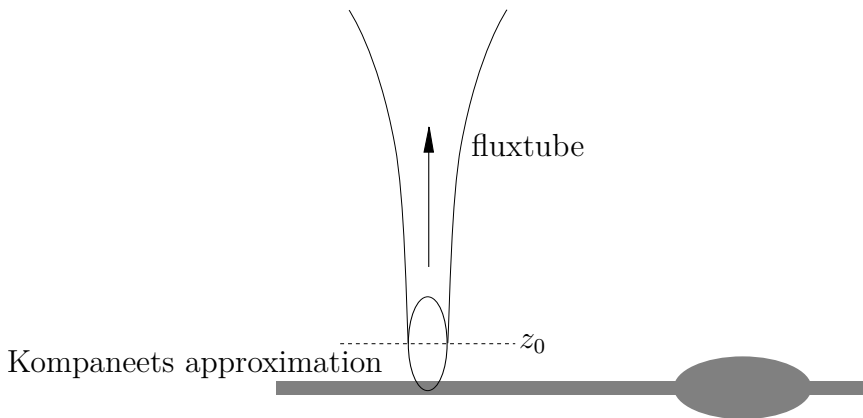


Figure 1.11: Sketch of the connection of Kompaneets approximation and galactic wind. The initial conditions for the wind are calculated at the reference level z_0 .

The Kompaneets superbubble is expanding until the *center of the ellipsoid is reaching the reference level z_0* (the needed time until the superbubble center has reached z_0 is

denoted as t_0), as it is already indicated in Figure 1.11. Doing this also enables one to find a somewhat physically motivated estimate for the fluxtube surface A_0 at the reference level (for details see section 2.11), more precisely A_0 is simply taken as the cross section of the ellipsoid at z_0 , which is just $A_0 = b(t_0)^2\pi$. The values E_g and E_c are then calculated by writing,

$$V(t_0) =: V_0 = \frac{4}{3}\pi a(t_0)b(t_0)^2, \quad (1.3.19)$$

$$E_g(t) = \frac{E_{th}(t)}{V_0}, \quad (1.3.20)$$

$$E_c(t) = \frac{E_{CR}(t)}{V_0}. \quad (1.3.21)$$

In these equations V_0 is the superbubble volume and E_{th} and E_{CR} are the *thermal energy* and the CR energy, respectively. It is assumed that approximately 10% of the total supernova energy E_{SN} are transformed in CRs, which is in accordance with e.g. Berezhko & Völk (2000) and Berezhko & Völk (2006), who constrain the CR energy production to 10 – 40%. It is further assumed that a single supernova produces the (commonly used) energy $E_{SN} = 10^{51}$ ergs. As already mentioned, the supernovae are exploding in equidistant time intervals, thus the energy $E_{SN}(t)$ is a step-function in time (see Figure 1.12). Applying the modified Kompaneets approximation as explained, the final results can be calculated and are presented below,

$$\left\{ \begin{array}{ll} t_{ges} & = 1.2 \cdot 10^7 \text{ yrs} \quad (\text{period of supernova explosions}), \\ dt & = 4.8 \cdot 10^5 \text{ yrs} \quad (\text{time interval between 2 supernovae}), \\ n_{max} & = 13 \quad (\text{number of SNe before GW simulation is started}), \\ t_0 & = 12.2 dt \quad (\text{time until galactic wind simulation is started}), \\ b(t_0) & = 561.3 \text{ pc} \quad (\text{minor half axis at } z = z_0), \\ A_0 & = 98976.4 \text{ pc}^2 \quad (\text{fluxtube crosssection at } z = z_0), \\ V_0 & = 1.466 \text{ pc}^3 \quad (\text{volume of the superbubble at } t_0). \end{array} \right. \quad (1.3.22)$$

These values are sufficient to calculate $E_g(t)$ and $E_c(t)$ in dependence on time. In section 3.4.1 the here derived values are used to model the *time-dependent inner boundary*

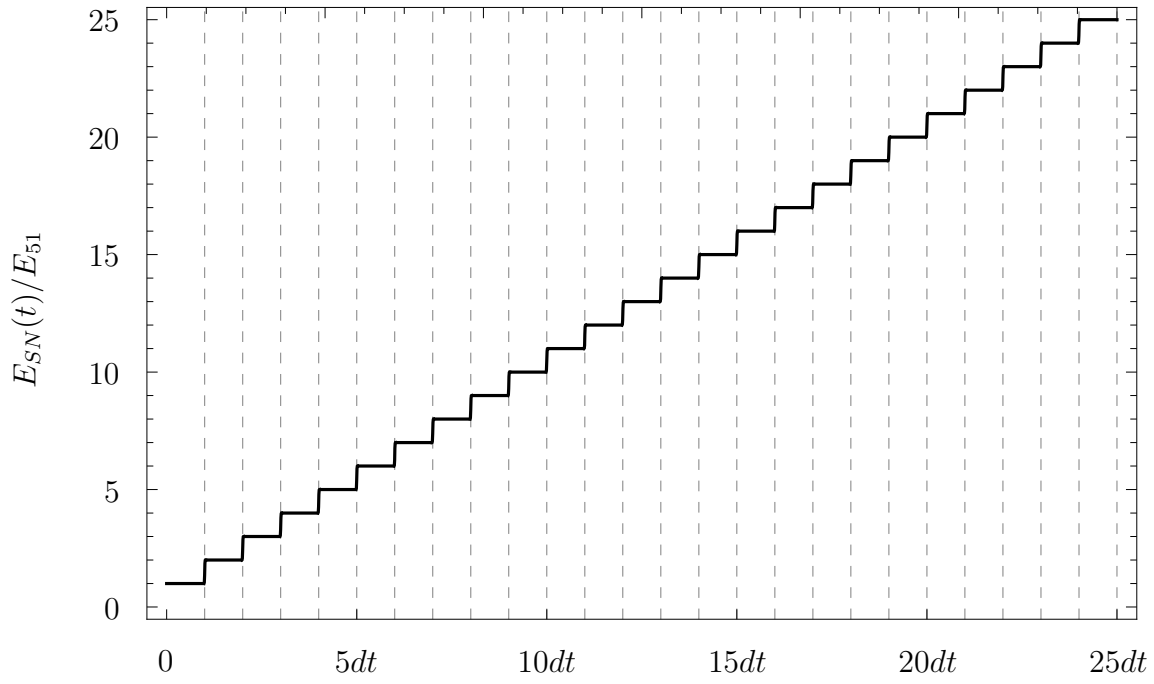


Figure 1.12: Energy input of supernovae exploding in equidistant times dt (plotted with MATHEMATICA).

conditions.

2 Physical Equations

In this section the basic equations of CR hydrodynamics will be explained briefly. These equations describe the behaviour of matter (fluids and gases). It is possible to formulate them in a *conservative form*, meaning each of these equations correspond to a certain *conserved quantity*. In the case of hydrodynamics, there are three of them,

- conservation of mass,
- conservation of momentum and
- conservation of energy.

To obtain a closed system of equations, it is furthermore necessary to formulate an *equation-of-state (EOS)*, which relates the gas-pressure of the system with the inner energy of the gas. Before the equations are presented, the concept of an equation in conservative form will be explained very briefly.

2.1 Equations in Conservative Form

The idea of an equation in conservative form is to extract, which quantities are preserved in a volume element. A conservation law in its general form takes the form (see e.g. in Schnack (2009), p. 43),

$$\frac{\partial U_{ijk\dots}}{\partial t} = -\frac{\partial}{\partial x_m} F_{mijk\dots} , \quad (2.1.1)$$

where $U_{ijk\dots}$ and $F_{mijk\dots}$ are tensors of rank N and $N + 1$, respectively. This form has the advantage, that after integration over the volume V and application of *Gauss' Theorem*, one can write the conservation law as follows,

$$\frac{\partial}{\partial t} \int_V dV U_{ijk\dots} = \oint_{\partial V} dS_m F_{mijk\dots} , \quad (2.1.2)$$

where ∂V and dS_m are the *surface of the volume* V and the *infinitesimal surface normal*, respectively. If $F_{mijk\dots}$ is interpreted as the flux of $U_{ijk\dots}$ in direction x_m , the equation can be interpreted straightforward: Every temporal variation of the quantity $U_{ijk\dots}$ in the volume V must result in an equal flux through the bounding surface ∂V . Therefore $U_{ijk\dots}$ is a conserved quantity. The following conservative equations are special cases of this general conservation law, for $N = 0$ (mass and energy conservation) and for $N = 1$ (momentum conservation).

2.2 Equation of state

The equation of state is necessary to describe the internal structure of the gas. It relates several *thermodynamic quantities* of the gas, such as pressure p and volume V . In the case of an *ideal gas*, the EOS takes the following form,

$$pV = nRT , \quad (2.2.1)$$

where n is the *number of moles*, R the *universal gas constant* and T the *temperature*. This equation can also be written in other terms using the adiabatic index γ and the (internal) energy density E (see e.g. in Stowe (2007), p. 263),

$$p = E(\gamma - 1) . \quad (2.2.2)$$

Another quantity needed in the further thesis is the *specific enthalpy* h . It is a measure for the total energy of the fluid per mass element, and is defined in the following well known way,

$$h = \frac{E}{\rho} + \frac{p}{\rho} . \quad (2.2.3)$$

Now, with use of equation (2.2.2), the enthalpy h can be expressed as

$$h = \frac{\gamma}{\gamma - 1} \frac{p}{\rho} . \quad (2.2.4)$$

2.3 Continuity equation

This equation corresponds to conservation of mass. In conservative form it is written in the following form (see Breitschwerdt et al. (1991)),

$$\frac{\partial \rho}{\partial t} + \nabla \cdot (\rho \mathbf{u}) = q . \quad (2.3.1)$$

In this equation the first term,

$$\frac{\partial \rho}{\partial t} , \quad (2.3.2)$$

clearly describes the temporal variation of density ρ in a certain volume and the latter term,

$$\nabla \cdot (\rho \mathbf{u}) , \quad (2.3.3)$$

corresponds to the mass-flux out of the volume. The term on the right-hand-side (RHS) q is a mass-source/sink-term, which can arise from ionization of neutral atoms (source) or recombination of ionized particles with electrons (sink). Summarizing the continuity equation tells us, that the temporal variation of density in a definite volume must be equal to the net mass-flux out of the volume (apart from sources or sinks).

2.4 Equation of motion

The conservation of momentum in a fluid is described by the equation of motion presented in this section. It can be understood as the second law of Newton for fluids. In conservative form it takes the form (see Breitschwerdt et al. (1991)),

$$\frac{\partial \rho \mathbf{u}}{\partial t} + \nabla \mathbf{P} = \rho \mathbf{F} + \mathbf{m} . \quad (2.4.1)$$

In this equation, \mathbf{P} is the *momentum-flux tensor*, a tensor of second order, and is defined as follows,

$$\mathbf{P} = \rho \mathbf{u} \otimes \mathbf{u} + \left[p + \frac{B^2}{8\pi} \right] \cdot \mathbf{I} - \frac{\mathbf{B} \otimes \mathbf{B}}{4\pi} . \quad (2.4.2)$$

In this formula, p is the scalar pressure, \mathbf{B} is the magnetic field, \mathbf{I} the identity tensor and \mathbf{u} is the gas-velocity. The momentum-flux tensor \mathbf{P} describes the net-momentum outflow of a volume element with also taking the effects of magnetic fields into account. Analogously to the continuity equation, the temporal variation of momentum in a definite volume must be equal (in the absence of sources or sinks) to the net outflow of momentum through the surface of the volume. Nevertheless, in general there can be sources of momentum in a fluid, e.g. an external body force \mathbf{F} like gravity, or other sources, which are all denoted by \mathbf{m} .

The scalar pressure p consists of *three contributions* due to the three components of the plasma, namely the *gas component*, the *mean magnetic field* and the *cosmic ray component* (see section 1.2). All of these components contribute to the overall-pressure. The pressure of the *gas-component* and the *cosmic ray-component* are denoted by p_g and p_c , respectively. Besides these two components there also exists a pressure component caused by fluctuations in the magnetic field induced by resonant pitch-angle scattering of CR particles due to interaction of CRs with the magnetic field (see section 1.2.2). These fluctuations are treated as waves, which propagate down the cosmic ray pressure-gradient. The pressure-component will be denoted as *wave pressure* p_w and can be calculated as follows,

$$p_w = \frac{\langle(\delta\mathbf{B})^2\rangle}{8\pi}. \quad (2.4.3)$$

In fact, the scalar pressure p can be written as a superposition of three pressure-components,

$$p = p_g + p_c + p_w. \quad (2.4.4)$$

Using (2.4.4), the momentum-flux tensor can be expressed in the following form,

$$\mathbf{P} = \rho\mathbf{u} \otimes \mathbf{u} + \left[p_g + p_c + p_w + \frac{B^2}{8\pi} \right] \cdot \mathbf{I} - \frac{\mathbf{B} \otimes \mathbf{B}}{4\pi}. \quad (2.4.5)$$

2.5 Equation of energy

Not surprisingly this equation corresponds to the conservation of energy in a fluid. As before, there also exists a conservative form of this formula (see Breitschwerdt et al.

(1991)),

$$\frac{\partial W}{\partial t} + \nabla \cdot \mathbf{S} = \rho \mathbf{u}(\mathbf{F} + \mathbf{m}) + \mathcal{E} . \quad (2.5.1)$$

Here, W is the *energy density* in a definite volume , \mathbf{S} the *energy-flux density* of the system, and \mathcal{E} corresponds to *energy-sources/sinks*. W and \mathbf{S} are defined in the following way,

$$W = \frac{1}{2} \rho u^2 + \frac{p_g}{\gamma_g - 1} + \frac{p_c}{\gamma_c - 1} + \frac{\langle (\delta \mathbf{B})^2 \rangle}{4\pi} + \frac{B^2}{8\pi} , \quad (2.5.2)$$

$$\begin{aligned} \mathbf{S} = & \left(\frac{1}{2} u^2 + \frac{\gamma_g p_g}{\gamma_g - 1 \rho} \right) \rho \mathbf{u} + \frac{1}{\gamma_c - 1} [\gamma_c p_c (\mathbf{u} + \mathbf{v}_A) - \bar{\kappa} \nabla p_c] \\ & + \frac{\langle (\delta \mathbf{B})^2 \rangle}{4\pi} \left[\frac{3}{2} \mathbf{u} + \mathbf{v}_A \right] + \frac{\mathbf{E} \times \mathbf{B}}{4\pi} . \end{aligned} \quad (2.5.3)$$

The energy density W can be understood as the amount of energy in a finite volume of the fluid, and exists of the *kinetic energy density* (first term), the energy densities of the *gas-component* and the *CR component* (second and third term, respectively, compare with (2.2.2)), the energy density in the volume due to the *Alfvén-waves* (third term) and the *magnetic energy* (fourth term).

The energy-flux density \mathbf{S} can be interpreted as the energy per volume which flows out through the surface of the volume-element. The first term in brackets is the flow of the energy density of the gas-component, consisting of the kinetic part and the enthalpy of the gas (compare with (2.2.4)). The second bracketed term corresponds to the energy-flow of the CR component of the gas which is composed of the enthalpy of the system and the diffusion component with diffusion coefficient κ . The diffusion part has negative sign, because CR particles diffuse into the direction of negative CR pressure gradient. The third term corresponds to the energy-flow of the Alfvén-waves through the volume element and the fourth term is the well-known Poynting-vector, which describes the electromagnetic energy flow through the volume.

Apart from these basic conservation laws of magnetohydrodynamics, two more equations are needed to ensure on the one hand a hydrodynamical description of the cosmic ray component and on the other hand to describe the exchange of energy between the background flow, the CRs and the Alfvén waves.

2.6 Transport equation for cosmic rays

The equation discussed here is the *transport equation for CRs* (2.6.1), which describes the advective and diffusive transport of CR particles.

$$\frac{\partial}{\partial t} \left(\frac{p_c}{\gamma_c - 1} \right) + \nabla \cdot \left[\frac{\gamma_c}{\gamma_c - 1} (\mathbf{u} + \mathbf{v}_A) p_c - \frac{\kappa}{\gamma_c - 1} \nabla p_c \right] = (\mathbf{u} + \mathbf{v}_A) \cdot \nabla p_c + Q . \quad (2.6.1)$$

In this equation the term in square brackets is the *cosmic ray flux density* \mathbf{F}_c , which consists of the convective flux, which flows with velocity $\mathbf{u} + \mathbf{v}_A$ (the Alfvén velocity is defined relative to the gas-flow velocity), and the diffusive flux, which flows down the cosmic ray pressure gradient ∇p_c ,

$$\mathbf{F}_c := \frac{\gamma_c}{\gamma_c - 1} (\mathbf{u} + \mathbf{v}_A) p_c - \frac{\kappa}{\gamma_c - 1} \nabla p_c . \quad (2.6.2)$$

On the RHS of equation (2.6.1) the term $\mathbf{u} \nabla p_c$ corresponds to the rate of work done on the gas flow, $\mathbf{v}_A \nabla p_c$ is the CR energy density loss due to the generation of Alfvén waves and Q stands for all other energy gains and/or losses.

2.7 Energy exchange equation

In the following equation the energy transfer between the CR component and the Alfvén waves is described,

$$\frac{\partial}{\partial t} \left(\frac{\langle (\delta \mathbf{B})^2 \rangle}{4\pi} \right) + \nabla \cdot \left[\frac{\langle (\delta \mathbf{B})^2 \rangle}{4\pi} \left(\frac{3}{2} \mathbf{u} + \mathbf{v}_A \right) \right] = \mathbf{u} \cdot \nabla p_w - \mathbf{v}_A \cdot \nabla p_c + L , \quad (2.7.1)$$

where p_w is defined in (2.4.3). In analogy to the equation of state (2.2.2) the wave energy density also will be defined as

$$E_w := \frac{p_w}{\gamma_w - 1} , \quad (2.7.2)$$

which leads after comparison with (2.7.1) to the value $\gamma_w = \frac{3}{2}$.

The first term $\mathbf{u} \nabla p_w$ on the RHS of equation (2.7.1) takes the interaction of the Alfvén waves with the gas flow into account, more precisely it gives the work of p_w on the flow.

The term $\mathbf{v}_A \nabla p_c$ gives the rate of newly generated waves by scattering of CR particles at the magnetic field \mathbf{B} . Finally the term L corresponds to all sorts of other wave-energy losses or gains.

2.8 Assumptions and simplifications

This section deals with the various simplifications and assumptions made in this galactic wind model.

The gas dealt with in this thesis is assumed to be *perfectly conductive*. This means, that Ohm's law takes the form,

$$\mathbf{E} + \mathbf{v} \times \mathbf{B} = 0. \quad (2.8.1)$$

Further it is assumed, that the mean-magnetic field \mathbf{B} is *constant in time*. Faraday's law can be with help of (2.8.1) written as,

$$\frac{\partial \mathbf{B}}{\partial t} = -\nabla \times (\mathbf{v} \times \mathbf{B}). \quad (2.8.2)$$

If the magnetic field \mathbf{B} is constant in time, then $\frac{\partial \mathbf{B}}{\partial t} = 0$. Consequently, it must hold that $\mathbf{v} \times \mathbf{B} = 0$. This means, that the gas velocity \mathbf{v} is always parallel to the magnetic field \mathbf{B} . Considering (2.8.1) one can see immediately that $\mathbf{E} = 0$. In other words, assuming constant \mathbf{B} is equivalent to neglecting all electromagnetic forces (see Breitschwerdt et al. (1991)).

Further we neglect all sources or sinks of momentum and mass, especially $q = 0$ and $\mathbf{m} = 0$ (compare equations (2.4.1) and (2.5.1)). Because these simplifications have been already extensively discussed in Breitschwerdt et al. (1991), only the major arguments are mentioned here.

- Supernovae and stellar winds provide sources of momentum and mass, sinks can occur due to condensation of gas into clumps. Nevertheless it is very unlikely, that these sources or sinks are able to influence the gas in the fluxtube due to the magnetic field which acts to some extent like a shield,
- the inner boundary of the fluxtube is located sufficiently high above the mid-plane, such that most of the possible sources of energy and momentum are below the fluxtube and therefore only play a minor role. All of the sources caused by

supernovae are covered by using a *time-dependent inner boundary condition* (see sections 1.3 and 3.4.1).

A further simplification is made by neglecting the galactic rotation. This movement would lead to moving magnetic field lines in the region close to the disk and therefore cause a motion relative to the gas-flow. This would result in a much more complicated treatment of the galactic wind problem.

Finally all external sources or sinks of CR energy density ($Q = 0$) and wave energy density ($L = 0$) will be neglected.

2.9 Galactic Gravitational Potential

The gravitational potential ϕ used in this thesis consists of *two* components (strictly following Breitschwerdt et al. (1991)), namely the

- Bulge-Disk component, and the
- Halo component.

The Bulge-Disk component $\phi_{B,D}$ is defined as follows (for details, see Miyamoto & Nagai (1975)),

$$\phi_{B,D}(R, z) = - \sum_{i=1}^2 \frac{GM_i}{\sqrt{R^2 + (a_i + \sqrt{z^2 + b_i^2})^2}} . \quad (2.9.1)$$

The index $i = 1$ corresponds to quantities of the bulge, $i = 2$ consequently for quantities of the disk. M_i are the masses of the bulge/disk components, a_i and b_i are fitting parameters, z is the height above the galactic mid-plane, G is the gravitational constant and R is the distance from the galactic center.

The halo component can be evaluated using the approach of Innanen (1973), who approximated the gravitational potential of the dark-matter halo ϕ_H in the following way,

$$\phi_H(R, z) = \frac{GM_H}{R_b} \left[\ln \left(1 + \frac{\sqrt{R^2 + z^2}}{R_b} \right) + \frac{1}{1 + \frac{\sqrt{R^2 + z^2}}{R_b}} \right] - \phi_0 , \quad (2.9.2)$$

where R_b is a fitting parameter, M_H is halo-mass, ϕ_0 is a reference potential and the other parameters are like in (2.9.1). The gravitational potential ϕ is then,

$$\phi(R, z) = \phi_{B,D} + \phi_H \quad (2.9.3)$$

As one can see, the potential $\phi_H \rightarrow \infty$, if $z \rightarrow \infty$, which is not the case in the real world, in fact the halo has a certain size and then the gravitational potential ϕ tends to zero. To capture this behaviour, a cut-off height z_g is introduced for the gravitational potential, above which the gravitational acceleration $g = -\frac{\partial\phi(R, z)}{\partial z}$ has the expected behaviour $g \propto \frac{1}{z^2}$,

$$\phi(R, z) = \begin{cases} \phi_{B,D}(R, z) + \phi_H(R, z) & \text{if } z < z_g \\ g(R, z_g) \frac{z^2}{z} & \text{if } z \geq z_g \end{cases} \quad (2.9.4)$$

Furthermore the potential should be continuous at z_g , which fixes ϕ_0 because at the height $z = z_g$ the condition of continuity requires that,

$$\phi(R, z_g) = \phi_{B,D}(R, z_g) + \phi_H(R, z_g) = g(R, z_g)z_g . \quad (2.9.5)$$

The gravitational potential $\phi(R, z)$ and the corresponding gravitational acceleration $g(R, z)$ are visualized for the Milky-Way galaxy in Figure 2.1 and Figure 2.2, respectively. Appropriate parameters for the Milky-Way galaxy are the following (see Ramberger (2008), p. 24),

a_1 [kpc]	a_2 [kpc]	b_1 [kpc]	b_2 [kpc]	M_1 [M_\odot]	M_2 [M_\odot]
0	7.258	0.495	0.52	$2.05 \cdot 10^{10}$	$2.547 \cdot 10^{11}$
M_b [M_\odot]	R_b [kpc]	z_g [kpc]			
$1.35 \cdot 10^{11}$	13	100			

Table 2.1: Parameter set for the grav. potential described in Miyamoto & Nagai (1975) .

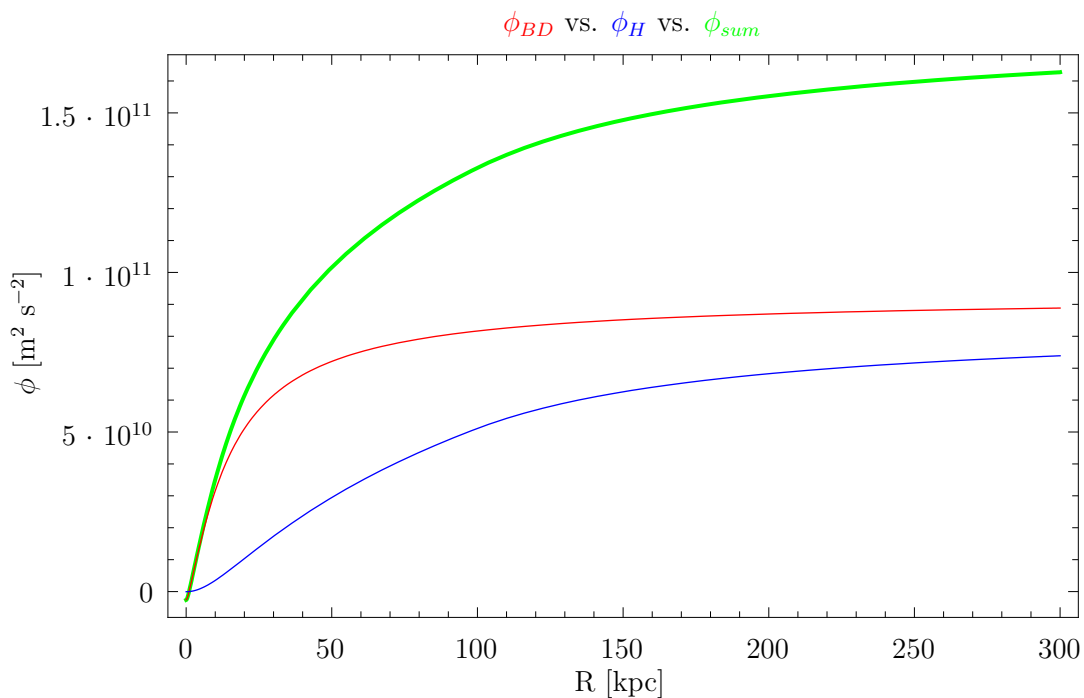


Figure 2.1: The gravitational potential ϕ for the Milky Way. The green full line corresponds to the sum of the bulge/disk component $\phi_{B,D}$ (red dashed line) and the Halo contribution ϕ_H (blue dashed line).

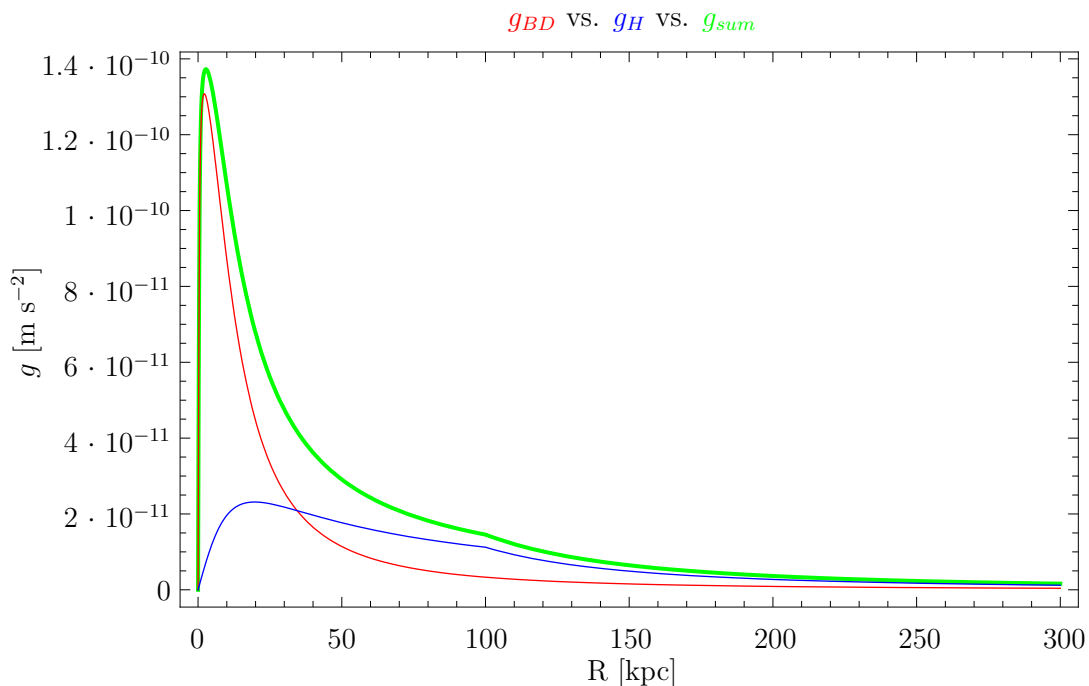


Figure 2.2: The gravitational acceleration g for the Milky Way. The green full line corresponds to the sum of the bulge/disk component $g_{B,D}$ (red dashed line) and the Halo contribution g_H (blue dashed line).

2.10 Final Set of Equations

In this section the final set of equation is written down again for the sake of clarity in this thesis. First, not surprisingly the gravitational force will be used as an external force F in equation (2.4.1),

$$\mathbf{F} = -\nabla\phi, \quad (2.10.1)$$

where ϕ is the gravitational potential as defined in (2.9.3). To obtain the equation in the form in which they are discretized, some algebraic manipulations must be done yet. First, substituting the momentum-flux tensor \mathbf{P} (2.4.5) in (2.4.1) and using the simplification that \mathbf{B} is constant in time, the equation of motion takes the following form,

$$\frac{\partial\rho\mathbf{u}}{\partial t} + \nabla \cdot (\rho\mathbf{u} \otimes \mathbf{u}) + \nabla(p_g + p_c + p_w) + \rho\nabla\phi = 0. \quad (2.10.2)$$

Obtaining the desired form of the energy-balance equations needs some more manipulations. First of all one should note, that the transport equation for CRs (2.6.1) and the exchange equation (2.7.1) are equivalent to conservation of CR energy and wave-energy, respectively. Furthermore, the equation of energy (2.5.1) is a conservation law for the *total energy* and therefore already contains the CR energy and wave-energy. Consequently the remaining contribution to the total energy (the gas pressure) also is conserved. Because the total energy conservation law is problematic if used in the numerical code, the conservation laws for the gas energy density E_g , the CR energy density E_c and the wave energy density E_w are used.

The equation of energy (2.5.1) takes, after inserting the energy density W (2.5.2) and the energy-flux density \mathbf{S} (2.5.3), the form,

$$\begin{aligned} \frac{\partial E_g}{\partial t} + \frac{\partial E_c}{\partial t} + \frac{\partial E_w}{\partial t} + \frac{1}{2} \frac{\partial(\rho u^2)}{\partial t} + \nabla \cdot \left(\frac{1}{2} \rho u^2 \cdot \mathbf{u} \right) + \nabla \cdot (\gamma_g E_g \mathbf{u}) \\ + \nabla \cdot (\gamma_c E_c (\mathbf{u} + \mathbf{v}_A)) - \nabla \cdot (\kappa \nabla E_c) + \nabla \cdot \left(E_w \left(\frac{3}{2} \mathbf{u} + \mathbf{v}_A \right) \right) = -\rho \mathbf{u} \cdot \nabla \phi + \mathcal{E}. \end{aligned} \quad (2.10.3)$$

This form of the energy equation also contains the *kinetic energy density* of the gas component. Using the equation of motion, the kinetic energy contribution can be eliminated.

For this purpose, the equation of motion is multiplied by \mathbf{u} , which leads to

$$\frac{\partial \rho \mathbf{u}}{\partial t} \cdot \mathbf{u} + \nabla \cdot (\rho \mathbf{u} \otimes \mathbf{u}) \cdot \mathbf{u} + \nabla (p_g + p_c + p_w) \cdot \mathbf{u} = -\rho \mathbf{u} \cdot \nabla \phi. \quad (2.10.4)$$

Substituting now (2.10.4) into (2.10.3), the following equation is obtained,

$$\begin{aligned} & \frac{\partial E_g}{\partial t} + \frac{\partial E_c}{\partial t} + \frac{\partial E_w}{\partial t} + \underbrace{\frac{1}{2} \frac{\partial (\rho u^2)}{\partial t} + \nabla \cdot \left(\frac{1}{2} \rho u^2 \cdot \mathbf{u} \right) - \frac{\partial \rho \mathbf{u}}{\partial t} \cdot \mathbf{u} + \nabla \cdot (\rho \mathbf{u} \otimes \mathbf{u}) \cdot \mathbf{u}}_{\textcircled{1}} \\ & + \underbrace{\nabla \cdot (\gamma_g E_g \mathbf{u}) - \nabla p_g \cdot \mathbf{u}}_{\textcircled{2}} + \underbrace{\nabla \cdot (\gamma_c E_c (\mathbf{u} + \mathbf{v}_A)) - \nabla p_c \cdot \mathbf{u}}_{\textcircled{3}} - \nabla \cdot (\kappa \nabla E_c) \\ & + \underbrace{\nabla \cdot \left(E_w \left(\frac{3}{2} \mathbf{u} + \mathbf{v}_A \right) \right) - \nabla p_w \cdot \mathbf{u}}_{\textcircled{4}} = \mathcal{E}. \end{aligned} \quad (2.10.5)$$

The term $\textcircled{1}$ is now written down in component notation,¹

$$\begin{aligned} \textcircled{1} &= \frac{1}{2} (\partial_t (\rho u_i u_i) + \nabla_i (\rho u_j u_j u_i)) - \partial_t (\rho u_i) u_i - \nabla_i (\rho u_i u_j) u_j \\ &= \frac{1}{2} (\partial_t \rho) u_i u_i + \underbrace{\frac{1}{2} (\nabla_i \rho u_i) u_j u_j}_{=0 \text{ (Continuity equation)}} + \cancel{\frac{1}{2} (\partial_t u_i) \rho u_i} + \cancel{\rho u_i (\nabla_i u_j) u_j} \\ & \quad - \underbrace{(\partial_t \rho) u_i u_i - \nabla_i (\rho u_i) u_j u_j}_{=0 \text{ (Continuity equation)}} - \cancel{\rho u_i (\partial_t u_i)} - \cancel{\rho u_i (\nabla_i u_j) u_j} = 0. \end{aligned} \quad (2.10.6)$$

After showing that $\textcircled{1}$ vanishes, the next term of interest is $\textcircled{2}$. Therefore the EOS (2.2.2) is used,

$$\begin{aligned} \textcircled{2} &= \nabla \cdot (\gamma_g E_g \mathbf{u}) - \nabla p_g \cdot \mathbf{u} \\ &= \gamma_g \nabla \cdot (E_g \mathbf{u}) - \nabla \cdot (p_g \mathbf{u}) + p_g \nabla \cdot \mathbf{u} \\ &= \gamma_g \nabla \cdot (E_g \mathbf{u}) - (\gamma_g - 1) \nabla \cdot (E_g \mathbf{u}) + p_g \nabla \cdot \mathbf{u} \\ &= \nabla \cdot (E_g \mathbf{u}) + p_g \nabla \cdot \mathbf{u}. \end{aligned} \quad (2.10.7)$$

¹Note that $\partial_t \equiv \frac{\partial}{\partial t}$.

The terms ③ and ④ are calculated analogically (with using $\gamma_w = 3/2$),

$$\begin{aligned}
 \textcircled{3} &= \nabla \cdot (\gamma_c E_c(\mathbf{u} + \mathbf{v}_A)) - \nabla p_c \cdot \mathbf{u} \\
 &= \nabla \cdot (\gamma_c E_c(\mathbf{u} + \mathbf{v}_A)) - \nabla \cdot (p_c \mathbf{u}) + p_c \nabla \cdot \mathbf{u} \\
 &= \nabla \cdot (\gamma_c E_c(\mathbf{u} + \mathbf{v}_A)) - (\gamma_c - 1) \nabla \cdot (E_c \mathbf{u}) + p_c \nabla \cdot \mathbf{u} \\
 &= \nabla \cdot (E_c(\mathbf{u} + \gamma_c \mathbf{v}_A)) + p_c \nabla \cdot \mathbf{u} .
 \end{aligned} \tag{2.10.8}$$

$$\begin{aligned}
 \textcircled{4} &= \nabla \cdot \left(E_w \left(\frac{3}{2} \mathbf{u} + \mathbf{v}_A \right) \right) - \nabla p_w \cdot \mathbf{u} \\
 &= \nabla \cdot \left(E_w \left(\frac{3}{2} \mathbf{u} + \mathbf{v}_A \right) \right) - \nabla \cdot (p_w \mathbf{u}) + p_w \nabla \cdot \mathbf{u} \\
 &= \nabla \cdot \left(E_w \left(\frac{3}{2} \mathbf{u} + \mathbf{v}_A \right) \right) - \left(\frac{3}{2} - 1 \right) \nabla \cdot (E_w \mathbf{u}) + p_w \nabla \cdot \mathbf{u} \\
 &= \nabla \cdot (E_w(\mathbf{u} + \mathbf{v}_A)) + p_w \nabla \cdot \mathbf{u} .
 \end{aligned} \tag{2.10.9}$$

Using all of these manipulations, the energy equation can be expressed in the following form,

$$\begin{aligned}
 &\frac{\partial E_g}{\partial t} + \nabla E_g \cdot \mathbf{u} + p_g \nabla \cdot \mathbf{u} + \\
 &\frac{\partial E_c}{\partial t} + \nabla E_c \cdot (\mathbf{u} + \gamma_c \mathbf{v}_A) + p_c \nabla \cdot \mathbf{u} + \\
 &\frac{\partial E_w}{\partial t} + \nabla E_w \cdot (\mathbf{u} + \mathbf{v}_A) + p_w \nabla \cdot \mathbf{u} = \mathcal{E} .
 \end{aligned} \tag{2.10.10}$$

Finally, the external energy sources and sinks \mathcal{E} , which are likely to be present in galactic winds are *additional heating* Γ and *cooling* Λ .

Comparison with (2.6.1) and (2.7.1) shows that the additional factor $\mathbf{v}_A \cdot \nabla p_c$ has to be added in the energy balance equations for the CRs and wave-energy.

The final set of equations to be solved then takes the following form,

$$\frac{\partial \rho}{\partial t} + \nabla \cdot (\rho \mathbf{u}) = 0 , \quad (2.10.11)$$

$$\frac{\partial \rho \mathbf{u}}{\partial t} + \nabla \cdot (\rho \mathbf{u} \otimes \mathbf{u}) + \nabla (p_g + p_c + p_w) + \rho \nabla \phi = 0 , \quad (2.10.12)$$

$$\frac{\partial E_g}{\partial t} + \nabla \cdot (E_g \mathbf{u}) + p_g \nabla \cdot \mathbf{u} = \Gamma - \Lambda , \quad (2.10.13)$$

$$\frac{\partial E_c}{\partial t} + \nabla \cdot (E_c (\mathbf{u} + \gamma_c \mathbf{v}_A)) + p_c \nabla \cdot \mathbf{u} - \mathbf{v}_A \cdot \nabla p_c = \nabla \cdot (\kappa \nabla E_c) , \quad (2.10.14)$$

$$\frac{\partial E_w}{\partial t} + \nabla \cdot (E_w (\mathbf{u} + \mathbf{v}_A)) + p_w \nabla \cdot \mathbf{u} + \mathbf{v}_A \cdot \nabla p_w = 0 . \quad (2.10.15)$$

2.11 Fluxtube geometry

Throughout this thesis, all calculations are performed in a 1D-fluxtube geometry. For this purpose the equations have to be reformulated, which is done in this section.

The fluxtube used here is explained and motivated in more detail in Breitschwerdt et al. (1991). Using this geometry has the following main advantages,

- the magnetic field lines are characterizing the flow geometry, assuming that there exist *locally open field lines*, which make a transition from plane-parallel (close to the disk) to spherical geometry (far away from the disk, see also section 1.1). This has been confirmed by recent 3D-hydrodynamical simulations (see e.g. Kulpa-Dybel et al. (2011)), which shows that initially arbitrary shaped magnetic fields are evolving to a quadrupole-like structure with respect to the galactic plane, and
- the model can be described as a 1D-model, which has obvious numerical advantages.

All unknown quantities depend on the *projected distance z from the galactic plane* (compare with Dorfi & Breitschwerdt (2012), p. 3). The transition can be achieved by specifying the fluxtubes' cross-section A dependent on z (see Breitschwerdt et al. (1991) and Dorfi & Breitschwerdt (2012)),

$$A(z) = A_0 \left[1 + \left(\frac{z}{Z_0} \right)^2 \right] , \quad (2.11.1)$$

where A_0 is the cross-section for $z = 0$, and Z_0 represents the *typical scale* of the transition from plane-parallel to spherical geometry (compare with Figure 2.3).

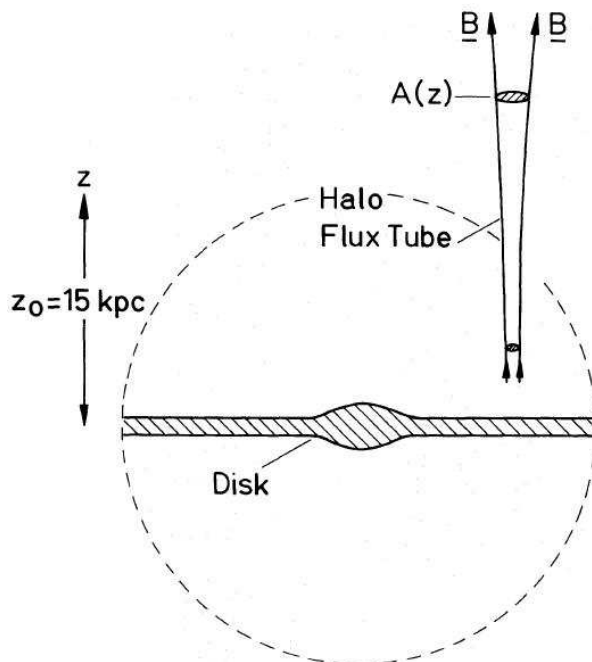


Figure 2.3: Schematic view of an fluxtube, arising above the galactic mid-plane and then making a transition from plane-parallel to spherical geometry (see Breitschwerdt et al. (1991), p. 5).

This geometry can be described by a metric tensor, which is important how to define the differentiation operators like divergence and gradient. For this purpose, adapted *cylindrical coordinates* (z, φ, R) are introduced, where z is the height above the mid-plane and R and φ are the radial and angular coordinate in the plane of $A(z)$, respectively. Usual Cartesian coordinates (x, y, z) can be written in terms of the new coordinates as follows,

$$A_0 =: R^2 \pi, \quad (2.11.2)$$

$$r(z) := \sqrt{\frac{A(z)}{\pi}} = \sqrt{\frac{A(z)}{A_0}} R, \quad (2.11.3)$$

$$z = z, \quad (2.11.4)$$

$$x = r(z) \cos(\varphi), \quad (2.11.5)$$

$$y = r(z) \sin(\varphi). \quad (2.11.6)$$

The term $r(z)$ takes into account that the radial coordinate scales with $\sqrt{A(z)}$. Following the usual procedure in defining a *basis vector system* $(\mathbf{e}_R, \mathbf{e}_\varphi, \mathbf{e}_z)$,

$$\mathbf{e}_z = \frac{\partial x}{\partial z} \mathbf{e}_x + \frac{\partial y}{\partial z} \mathbf{e}_y + \frac{\partial z}{\partial z} \mathbf{e}_z, \quad (2.11.7)$$

$$\mathbf{e}_R = \frac{\partial x}{\partial R} \mathbf{e}_x + \frac{\partial y}{\partial R} \mathbf{e}_y + \frac{\partial z}{\partial R} \mathbf{e}_z, \quad (2.11.8)$$

$$\mathbf{e}_\varphi = \frac{\partial x}{\partial \varphi} \mathbf{e}_x + \frac{\partial y}{\partial \varphi} \mathbf{e}_y + \frac{\partial z}{\partial \varphi} \mathbf{e}_z, \quad (2.11.9)$$

one arrives at the the following basis vector system (substituting (2.11.1) and (2.11.2)),

$$\mathbf{e}_z = \begin{pmatrix} \frac{zR\sqrt{\pi}}{\sqrt{A(z)Z_0^2}} \cos(\varphi) \\ \frac{zR\sqrt{\pi}}{\sqrt{A(z)Z_0^2}} \sin(\varphi) \\ 1 \end{pmatrix}, \quad \mathbf{e}_\varphi = r(z) \begin{pmatrix} -\sin(\varphi) \\ \cos(\varphi) \\ 0 \end{pmatrix}, \quad \mathbf{e}_R = \sqrt{\frac{A(z)}{A_0}} \begin{pmatrix} \cos(\varphi) \\ \sin(\varphi) \\ 0 \end{pmatrix}. \quad (2.11.10)$$

The metric tensor $\mathbf{g}^{(exact)}$ then takes the following form (in components $i = 1, 2, 3$ corresponds to z, φ, R , respectively),

$$(g_{ij}^{(exact)}) = \begin{pmatrix} 1 + \frac{z^2 R^2 \pi}{A(z) Z_0^4} & 0 & \frac{Rz}{Z_0^2} \\ 0 & r(z)^2 & 0 \\ \frac{Rz}{Z_0^2} & 0 & \frac{A(z)}{A_0} \end{pmatrix}. \quad (2.11.11)$$

The metric tensor derived here is obviously not orthogonal, to achieve this an approximation is needed: the gas flow is always considered to be orthogonal to the cross section $A(z)$, meaning that \mathbf{e}_z is assumed to be perpendicular to $A(z)$. The metric can then be approximated by the orthogonal metric tensor \mathbf{g} ,

$$(g_{ij}) = \begin{pmatrix} 1 & 0 & 0 \\ 0 & r(z)^2 & 0 \\ 0 & 0 & \frac{A(z)}{A_0} \end{pmatrix}. \quad (2.11.12)$$

3 Numerical method

In this section the numerical method is discussed (strictly following Dorfi & Drury (1987)) , which is used to integrate the set of equations (2.10.11) - (2.10.15).

3.1 The grid equation

Galactic winds are described in this thesis by *magnetohydrodynamical equations* coupled with *time-dependent inner boundary conditions*. Such a flow is very likely to have features like shock-waves. To describe such locally restricted phenomenons with a sufficiently high number of grid points, the spatial grid has to be adjusted to the flow features. The grid equation discussed in this section ensures that the grid points are redistributing according to accuracy demands.

The flow structure in a galactic wind is due to shocks and variable boundaries permanently changing, the grid therefore must have the ability to change with time to assure the best resolution. More precisely, grid points must be concentrated in flow areas with steep gradients of certain quantities (like density, pressure, etc.), and in contrast should be able to spread in areas of flat gradients. These properties are achieved by solving the grid equation simultaneously to the set of CR hydrodynamic equations.

A so-called adaptive grid method can be found in Dorfi & Drury (1987). It is assumed that x_1, \dots, x_N are the grid points, where N describes the number of grid points. The question is how to distribute these grid points dependent on physical quantities. In areas of required high resolution, the points should be concentrated (with respect to an equidistant distribution) and if lower spatial resolution is enough to describe the flow, the points should be spread out (again w.r.t. an equidistant distribution). Hence the necessity arises to define measures for these two situations. If n_i is the actual distribution of grid points and R_i is the desired distribution, the easiest and straightforward way is

to say that n_i should be proportional to R_i ,

$$n_i \propto R_i, \quad (3.1.1)$$

where i is the index of the grid points. Unfortunately, this simple concept cannot be applied directly, because if n changes too fast, instabilities can occur. As a workaround, n_i is proportional to various smoothing operators multiplied with R_i , which assure moderate changes in n_i . The n_i are defined in the following way,

$$\Delta x_i := x_{i+1} - x_i, \quad (3.1.2)$$

$$n_i := \frac{X}{\Delta x_i}, \quad (3.1.3)$$

where X is a *natural length scale*, which depends on the problem to be solved. Defining the desired point concentration R_i is a little bit more complicated. Dorfi & Drury (1987) take R_i as the arc-length of a function f , or in general a ensemble of M functions (compare with Figure 3.1),

$$f_1, \dots, f_M. \quad (3.1.4)$$

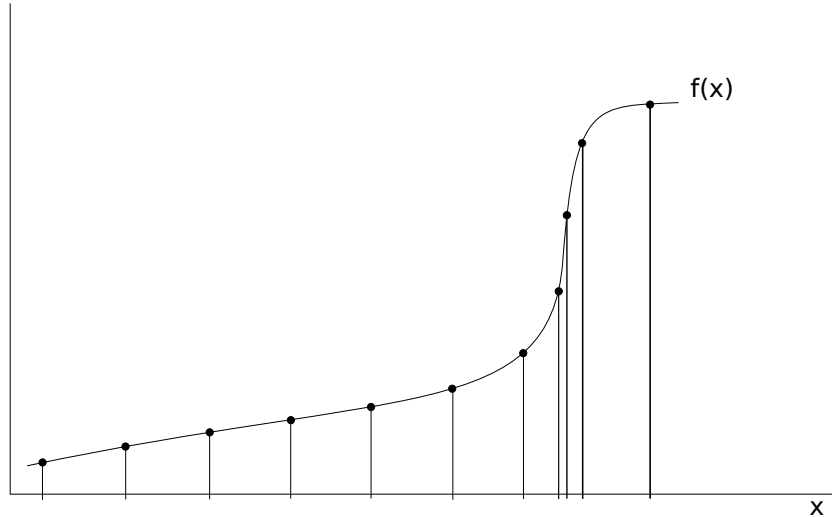


Figure 3.1: Visualization of the idea of equidistant arclength along a function $f(x)$. In the areas of steep gradients, the point distribution is much higher than in those of flat gradients.

Implementing this concept, the desired grid point concentration R_i takes the following

form,

$$f_{k,i} := f_k(x_i) , \quad (3.1.5)$$

$$\Delta f_{k,i} := f_{k,i+1} - f_{k,i} , \quad (3.1.6)$$

$$R_i := \sqrt{1 + \sum_{k=1}^M \frac{X_i}{F_k} g_k \frac{\Delta f_{k,i}}{\Delta x_i}} , \quad (3.1.7)$$

where g_k are chooseable weights assigned to the corresponding functions f_k and F_k is again a natural scale with respect to the function f_k .¹

The spatial smoothing which has been already mentioned above, can be implemented by introducing the following condition (see Dorfi & Drury (1987), p. 4),

$$\frac{\alpha}{\alpha + 1} \leq \frac{n_{i+1}}{n_i} \leq \frac{\alpha + 1}{\alpha} , \quad (3.1.8)$$

where α corresponds to the rigidity of the grid, meaning that $\alpha \gg 1$ is equivalent to a grid with a almost constant lattice parameter, which results in very small maximal allowed changes from n_i to n_{i+1} (compare with (3.1.8)). The value of α is chosen in a way which doesn't allow the grid changes greater than approximately 30%. Applying a function which obeys 3.1.8 and doing some more sophisticated manipulations to the resulting grid equation (for details, see LeVeque et al. (1998), p. 178), the spatial smoothing can be written as,

$$\tilde{n}_i = n_i - \alpha(\alpha + 1)(n_{i+1} - 2n_i + n_{i-1}) . \quad (3.1.9)$$

Furthermore, in addition to the spatial smoothing also a *temporal smoothing* must be applied. If the proportionality is chosen in the following way,

$$\hat{n}_i = \tilde{n}_i + \tau \frac{\tilde{n}_i - \tilde{n}_i^{(old)}}{\delta t} , \quad (3.1.10)$$

then the grid adjusts on a timescale τ and does not change much for variations shorter than τ (δt corresponds to the time-step). The value of the timescale is dependent on the considered problem, meaning that it must be much shorter than the shortest timescale

¹The scales F_k and X_i are necessary, because the variables f_k and x_i are physical variables with a dimension, further they can differ from each other by many orders of magnitudes. If the physical problem allows it, the scale functions can be set to unity.

of a process of interest.

Putting all together leads to the final form of the grid equation,

$$\frac{\hat{n}_{i-1}}{R_{i-1}} = \frac{\hat{n}_i}{R_i}. \quad (3.1.11)$$

The boundary conditions remain to be defined, in a way that the innermost grid point x_I and the outermost grid point x_O are fixed (these two points are defining the size of the computational domain). The boundary conditions for the grid equation can be specified by setting the grid point concentration gradients equal to zero at the boundaries,

$$\text{Inner boundary } (x = x_I): \begin{cases} x_N & = x_I \\ n_{N-2} & = n_{N-1} \end{cases}, \quad (3.1.12)$$

$$\text{Outer boundary } (x = x_O): \begin{cases} x_1 & = x_O \\ n_1 & = n_2 \end{cases}. \quad (3.1.13)$$

3.2 Artificial Viscosity

Astrophysical gases are often assumed to be ideal, that means that dissipation effects cannot occur. In the context of galactic winds, shock waves are (as already discussed) very likely to occur. In the case of ideal magnetohydrodynamics, these shock fronts will be infinitely thin and shown as discontinuities in density ρ and gas pressure p_g . In reality, astrophysical fluids are not perfect gases, saying that dissipative effects will occur due to molecular interactions like frictional forces between atoms and molecules. Viscosity is one of these dissipative processes like conversion from kinetic energy to thermal energy, which determines the thickness of a shock (e.g. compare with Mihalas & Mihalas (1999), p. 241). One problem in describing such dissipative processes with (magneto-)hydrodynamics is the microscopic length scales at which these processes occur (more precisely the length scale is of the order of the *mean free path* of the gas particles). Hydrodynamical equations are unfortunately averaged over all microscopic effects of the gas, a so called *continuous theory*, that means all processes which can be described with this theory have to have length scales much greater than the mean free path of the gas.

Applying numerics to the problem without introducing artificial viscosity would lead to numerical instabilities and other major problems in solving the equations, because the discontinuity (shock front) would be infinitesimally thin and could not be resolved within two neighbored grid points (compare with Figure 3.2).

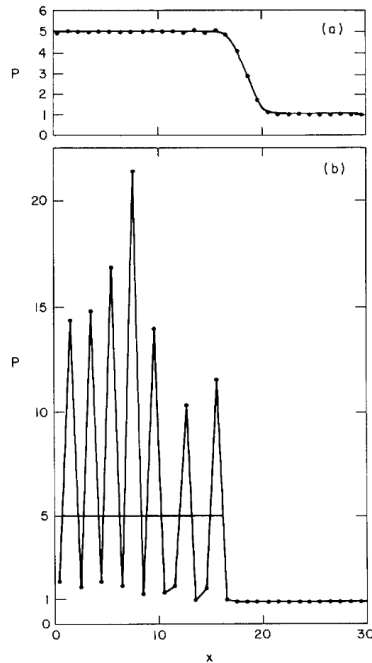


Figure 3.2: Shock front computed numerically (a) with artificial viscosity and (b) without applying artificial viscosity. The numerical instabilities in (b) can be seen very clearly (see Mihalas & Mihalas (1999) p. 281).

Taking into account dissipative effects can be effectively interpreted as solving *not* the ideal hydrodynamical equations, but the *Navier-Stokes equations* for viscous fluids. The question arises why the Navier-Stokes equations can't be solved from scratch instead. The answer is that a much more complicated treatment of these equations would be necessary. Applying the artificial viscosity only in regions where discontinuities can occur provides a useful workaround.

The shock fronts are broadened over a few grid cells due to locally applied artificial viscosity, which is implemented by introducing a so-called *viscous pressure tensor* \mathbf{Q} . This tensor should obey the following conditions (according to Tscharnuter & Winkler (1979)):

1. shock fronts should be broadened over a certain number of grid cells; in the case of an adaptive grid this varies spatially and temporally.

2. Homologous contractions of the gas should be calculated without influence of artificial viscosity.
3. Expanding regions of the flow should also be free of artificial viscosity.

A form of Q which obeys all of these conditions is the following one (basically derived by Vonneumann & Richtmyer (1950), but with an additional linear term introduced by Tscharnuter & Winkler (1979),

$$\mu_Q := -q_1 l_q c_s + q_2^2 l_q^2 \min(\nabla \cdot \mathbf{u}, 0) , \quad (3.2.1)$$

$$\mathbf{Q} = \mu_Q [\nabla \otimes \mathbf{u} - \frac{1}{3}(\nabla \cdot \mathbf{u})\mathbf{I}] . \quad (3.2.2)$$

In equation (3.2.2), q_1 and q_2 are weights for the linear and quadratic terms of \mathbf{Q} , respectively, \mathbf{I} is the unity tensor and the factor $1/3$ assures that \mathbf{Q} is traceless, which is equivalent to the condition of vanishing artificial viscosity in the case of homologous contractions. The parameter l_q is denoted as the *typical viscous length scale*, consequently the products $q_1 l_q$ and $q_2 l_q$ determine the amount of linear and quadratic viscosity, respectively. As already emphasized before, the thickness should be covered from a sufficient number of grid points, consequently l_q is spatially and temporally variable in the case of an adaptive grid. Cosmic-ray driven galactic winds are accelerated by CRs due to the *first-order Fermi mechanism*, this means that the thickness of the shock must be much smaller than the typical mean free path of CR particles l_{CR} (see Dorfi & Breitschwerdt (2012)),

$$l_q \ll l_{CR} = \frac{\kappa}{u_s} , \quad (3.2.3)$$

where u_s is the shock velocity. The formulation of \mathbf{Q} as in (3.2.2) is invariant, this means it can be applied to an arbitrary geometry. In the case of a fluxtube geometry, the metric tensor already has been derived (see 2.11.12). Following the scheme from Tscharnuter & Winkler (1979), the divergence $\nabla \cdot \mathbf{u}$ and the symmetrized vector gradient ϵ^m_l are defined in its invariant form as follows,

$$\nabla \cdot \mathbf{u} = u^k_{;k} , \quad (3.2.4)$$

$$\epsilon^m_l = g^{mk} u_{(k;l)} , \quad (3.2.5)$$

where the semicolon indicates the *covariant derivative* with respect to the k -th variable

and where $u_{(k;l)}$ is defined as follows,

$$u_{(k;l)} := \frac{1}{2}(u_{k;l} + u_{l;k}). \quad (3.2.6)$$

Applying the fluxtube geometry, $\nabla \cdot \mathbf{u}$ and ϵ^m_l can be written as (compare with Dorfi & Breitschwerdt (2012)),

$$\nabla \cdot \mathbf{u} = \frac{1}{A(z)} \frac{\partial(Au)}{\partial z}, \quad (3.2.7)$$

$$\epsilon^m_l = \begin{pmatrix} \frac{\partial u}{\partial z} & 0 & 0 \\ 0 & \frac{u}{2A} \frac{\partial A}{\partial z} & 0 \\ 0 & 0 & \frac{u}{2A} \frac{\partial A}{\partial z} \end{pmatrix}. \quad (3.2.8)$$

The quadratic part of the artificial viscosity $\mathbf{Q}^{(quadr)}$ then becomes to

$$\mathbf{Q}^{(quadr)} = \frac{1}{A} \frac{\partial(Au)}{\partial z} \times \begin{pmatrix} \frac{\partial u}{\partial z} - \frac{1}{3A} \frac{\partial(Au)}{\partial z} & 0 & 0 \\ 0 & \frac{u}{2A} \frac{\partial A}{\partial z} - \frac{1}{3A} \frac{\partial(Au)}{\partial z} & 0 \\ 0 & 0 & \frac{u}{2A} \frac{\partial A}{\partial z} - \frac{1}{3A} \frac{\partial(Au)}{\partial z} \end{pmatrix}. \quad (3.2.9)$$

This tensor is indeed traceless, which is equivalent to no artificial viscosity in the case of homologous contractions.

Viscous forces are clearly also influencing the gas flow, this is taken into account by introducing an additional term, the *viscous momentum transfer* \mathbf{u}_Q , which can be expressed as (for details see Mihalas & Mihalas (1999) p. 263, or compare with Dorfi & Breitschwerdt (2012)),

$$\mathbf{u}_Q = -\nabla \cdot \mathbf{Q}. \quad (3.2.10)$$

This viscous momentum transfer \mathbf{u}_Q takes the following form in the fluxtube geometry

(see Dorfi & Breitschwerdt (2012)),

$$\mathbf{u}_Q = \begin{pmatrix} \frac{1}{A^{3/2}} \frac{\partial}{\partial z} \left[A^{1/2} \mu_Q \rho \frac{\partial(Au)}{\partial z} \left(\frac{\partial u}{\partial z} - \frac{1}{3} \frac{\partial(Au)}{\partial z} \right) \right] \\ 0 \\ 0 \end{pmatrix}, \quad (3.2.11)$$

$$u_Q := \|\mathbf{u}_Q\| = \frac{1}{A^{3/2}} \frac{\partial}{\partial z} \left[A^{1/2} \mu_Q \rho \frac{\partial(Au)}{\partial z} \left(\frac{\partial u}{\partial z} - \frac{1}{3} \frac{\partial(Au)}{\partial z} \right) \right]. \quad (3.2.12)$$

Viscosity is, as already explained above, a dissipative process, therefore kinetic energy is dissipated into thermal energy. The *specific energy dissipation* is denoted as ϵ_Q and is defined in the following way,

$$\epsilon_Q = -\frac{1}{\rho} \mathbf{Q} \cdot (\nabla \otimes \mathbf{u}). \quad (3.2.13)$$

In the fluxtube geometry ϵ_Q is written as (see Dorfi & Breitschwerdt (2012)),

$$\epsilon_Q = -\frac{3}{2} \frac{\mu_Q}{A} \frac{\partial(Au)}{\partial z} \left[\frac{\partial u}{\partial z} - \frac{1}{3A} \frac{\partial(Au)}{\partial z} \right]^2. \quad (3.2.14)$$

Keeping in mind that $\nabla \cdot \mathbf{u} < 0$ in the areas of non-vanishing artificial viscosity, this formula for ϵ_Q ensures that $\epsilon_Q > 0$, even in the discretized version. Otherwise, negative viscous energy dissipation is not physical and leads to instabilities (see Dorfi & Breitschwerdt (2012) and Tscharnuter & Winkler (1979)). The momentum equation (2.10.12) and the energy equation for the gas component (2.10.13) also need to be extended by terms, which take the viscous momentum transfer \mathbf{u}_Q and the specific energy dissipation ϵ_Q into account,

$$\frac{\partial \rho \mathbf{u}}{\partial t} + \nabla \cdot (\rho \mathbf{u} \otimes \mathbf{u}) + \nabla (p_g + p_c + p_w) + \rho \nabla \phi - \mathbf{u}_Q = 0, \quad (3.2.15)$$

$$\frac{\partial E_g}{\partial t} + \nabla \cdot (E_g \mathbf{u}) + p_g \nabla \cdot \mathbf{u} - \rho \epsilon_Q = \Gamma - \Lambda. \quad (3.2.16)$$

3.3 Discretization of the physical equations

In this section the set of physical equations (2.10.11) - (2.10.15) and the simultaneously solved grid equation (3.1.11) are discretized. The equations will be first integrated over a finite volume, this is necessary to ensure the (numerical) conservation of energy, mass and momentum (see Dorfi & Breitschwerdt (2012)).

The computational domain (the space between inner boundary and outer boundary) first is discretized with use of the grid equation. The outermost grid point is denoted as $l = 1$, consequently the innermost grid point must have the index $l = N$. The unknown variables are defined on the grid in the following manner (see LeVeque et al. (1998), p. 277):

- *Scalars* like density ρ , volume ΔV and the unknown energy densities E_g , E_c and E_w are defined in the *middle (inside) of the grid cell*.
- *Vector quantities* like the velocity \mathbf{u} or all sorts of fluxes are defined at the *cell boundaries*.

A grid of this kind is called *staggered mesh* and can be imagined as two different grids shifted with respect to each other such that all quantities are defined at cell boundary of one of the two grids (compare with Figure 3.3).

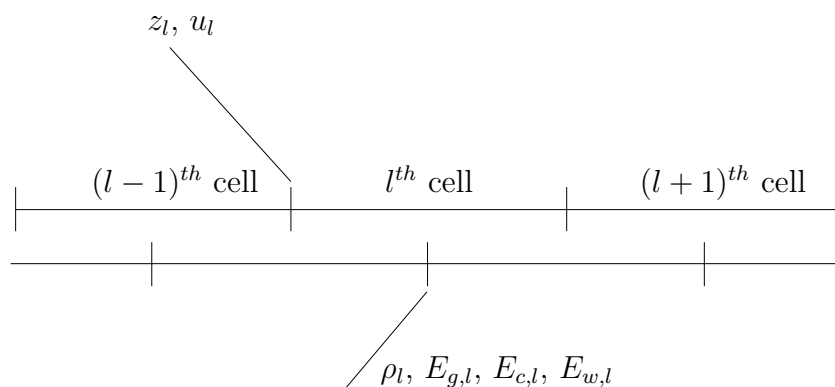


Figure 3.3: Schematic view of the staggered mesh used in this thesis. Some quantities are defined at grid border, and others in the middle of the cell.

Next the discretization of various operations (like integration over a volume and differentiations) are discussed in more detail. For this purpose, the *temporal operator* δ and

the *spatial difference* Δ are defined as follows (see Dorfi & Breitschwerdt (2012)),

$$\delta t = t^{(new)} - t^{(old)} , \quad (3.3.1)$$

$$\Delta x_l = x_{l-1} - x_l , \quad (3.3.2)$$

where the index l stands for the l -th grid cell and the superscripts (*new*) and (*old*) correspond to the quantities at the new time and the old time, respectively. Equations in conservative form have the following form (recalling equations (2.1.1) and (2.1.2)),

$$\frac{\partial}{\partial t} \int_{V(t)} dV U(\mathbf{x}, t) = \oint_{\partial V} dS_m F_m(\mathbf{x}, t) , \quad (3.3.3)$$

where $U(\mathbf{x}, t)$ is an arbitrary scalar function and $F_m(\mathbf{x}, t)$ is its corresponding flux function. The temporal variation of the quantity U in a finite volume V on the left hand side (the so called *volume term*) must be equal to the flux F_m through the surface of the volume ∂V on the right hand side (the so called *advection term*)², as it has been already pointed out earlier in this thesis. This global conservation of a quantity U can also be implemented in a discretized version of the equation, therefore it is necessary to write the equation in the volume-integrated form.

3.3.1 Discretization of the volume term

The volume term in the used numerical method is discretized in the following way,

$$\frac{\partial}{\partial t} \int_{V(t)} dV U \Rightarrow \frac{\delta \int_{V(t)} dV U}{\delta t} = \frac{1}{\delta t} \left[\left(\int_{V(t)} dV U \right)^{(new)} - \left(\int_{V(t)} dV U \right)^{(old)} \right] . \quad (3.3.4)$$

The integrals in (3.3.4) remain to get discretized. $V(t)$ is the volume of a certain grid cell, the time dependence arises from the fact, that an adaptive grid is used. The integral can be approximated in the discretized scheme as,

$$\int_{V(t)} dV U \Rightarrow U_l \Delta V_l . \quad (3.3.5)$$

The volume of the l -th grid cell ΔV_l has to be approximated as well. For this purpose one must recall, that a fluxtube geometry is used. Integrating of equation (2.11.1) over

²Temporal variation of the volume term is fully determined just by the advection term, if there are no sources or sinks.

one grid cell length (from z_l to z_{l+1}) leads to,

$$\int_{z_l}^{z_{l+1}} dz A_0 \left(1 + \frac{z^2}{Z_0^2} \right) = A_0 \left(\Delta z_l + \frac{\Delta z_l^3}{3Z_0^2} \right) =: \Delta V_l . \quad (3.3.6)$$

This formula suffices for being able to finally discretize the volume term as it is shown in the following expression,

$$\frac{\partial}{\partial t} \int_{V(t)} dV U \Rightarrow \frac{1}{\delta t} \left\{ \left[U_l A_0 \left(\Delta z_l + \frac{\Delta z_l^3}{3Z_0^2} \right) \right]^{(new)} - \left[U_l A_0 \left(\Delta z_l + \frac{\Delta z_l^3}{3Z_0^2} \right) \right]^{(old)} \right\} . \quad (3.3.7)$$

3.3.2 Discretization of the advection term

For the discretization of the advection term (right hand side of (3.3.3)) it is first necessary to rewrite the advection term as a volume integral again, using *Gauss' Theorem*,

$$\oint_{\partial V(t)} dS_m F_m(\mathbf{x}, t) = \int_{V(t)} dV \nabla \cdot \mathbf{F}(\mathbf{x}, t) . \quad (3.3.8)$$

In the fluxtube geometry, the divergence of a vectorial quantity $\nabla \cdot \mathbf{F}$ with \mathbf{F} defined as in (3.3.9) is given by (recalling equation (3.2.7)),

$$\mathbf{F} = \begin{pmatrix} F_z \\ 0 \\ 0 \end{pmatrix} , \quad (3.3.9)$$

$$\nabla \cdot \mathbf{F} = \frac{1}{A} \frac{\partial(A F_z)}{\partial z} = \frac{\partial(A F_z)}{\partial V} . \quad (3.3.10)$$

Equation (3.3.10) is discretized straightforward as follows,

$$\frac{\partial(A F_z)}{\partial V} \Rightarrow \frac{\Delta(A_l F_{z,l})}{\Delta V_l} , \quad (3.3.11)$$

consequently the final discretization of the advection term has the form,

$$\oint_{\partial V} dS_m F_m(\mathbf{x}, t) \Rightarrow \frac{\Delta(A_l F_{z,l})}{\Delta V_l} \Delta V_l = \Delta(A_l F_{z,l}) . \quad (3.3.12)$$

The aim of the next sections will be the discretization of the set of physical equations and of the grid equation.

3.3.3 Discretization of the continuity equation

The first equation is the continuity equation (2.10.11). Applying (3.3.7) and (3.3.12), this equation (in volume-integrated form) in its discretized form would look like the following expression,

$$\frac{\partial \rho}{\partial t} + \nabla \cdot (\rho \mathbf{u}) = 0 \Rightarrow \frac{\delta(\rho_l \Delta V_l)}{\delta t} + \Delta(A_l u_l \rho_l) = 0 . \quad (3.3.13)$$

In this form serious problems would arise if one tried to integrate this equation numerically. Two important facts are still not taken into account:

- ① The gas flow velocity \mathbf{u} is in the discretization scheme obviously always given with respect to the grid points. In the case of an adaptive grid the grid points also move inbetween the computational domain, in other words the grid moves itself. Consequently a *relative velocity* \mathbf{u}_{rel} must be defined.
- ② If shock waves are very likely to occur (e.g. in the case of galactic winds), the direction of the flow must be taken into account. Shocks only can influence areas *downstream* (in more detail only areas, which lie inbetween the *Mach-cone*). This means that quantities which are calculated in the middle of a cell (recall Figure 3.3) as mean values of the two grid points on the left and on the right of the cell, can cause non-physical results, because the mean values would be influenced by the shock front.

The relative velocity \mathbf{u}^{rel} as discussed in ① is defined in the following way and appears in every advection term (compare with Dorfi & Breitschwerdt (2012)),

$$\mathbf{u}_l^{rel} = \mathbf{u}_l - \mathbf{u}_{l,grid} \quad \xrightarrow{(1D \text{ fluxtube})} \quad u_l^{rel} = u_l - \frac{\delta z_l}{\delta t} , \quad (3.3.14)$$

where $\mathbf{u}_{l,grid}$ corresponds to the velocity of the grid at the l -th grid point. Knowing that and recalling the general conservation law (2.1.2), all physical equations in volume-integrated form in the case of an adaptive grid can be expressed as (see LeVeque et al. (1998), p. 280),

$$\frac{\partial}{\partial t} \int_{V(t)} dV U(\mathbf{x}, t) + \oint_{\partial V(t)} d\mathbf{S} U(\mathbf{x}, t) \mathbf{u}^{rel} - \int_{V(t)} dV (U_{source} - U_{sink}) = 0 . \quad (3.3.15)$$

To circumvent the problems discussed in ②, a special discretization of the advection terms is introduced, the so called *donor-cell advection scheme*. As already mentioned, because of the possibility of shock waves no quantities should be used for calculating differences of quantities, which are lying in the downstream region. Therefore it is necessary to use *forward differences* for the spatial discretization, if the relative flow velocity u_i^{rel} is outward directed, and otherwise the *backward differences* (see LeVeque (1992) p. 124-135, and compare with Figure 3.4),

$$\Delta f_l = \begin{cases} f_l - f_{l+1} & \text{(forward difference)} \\ f_{l-1} - f_l & \text{(backward difference)} \end{cases} . \quad (3.3.16)$$

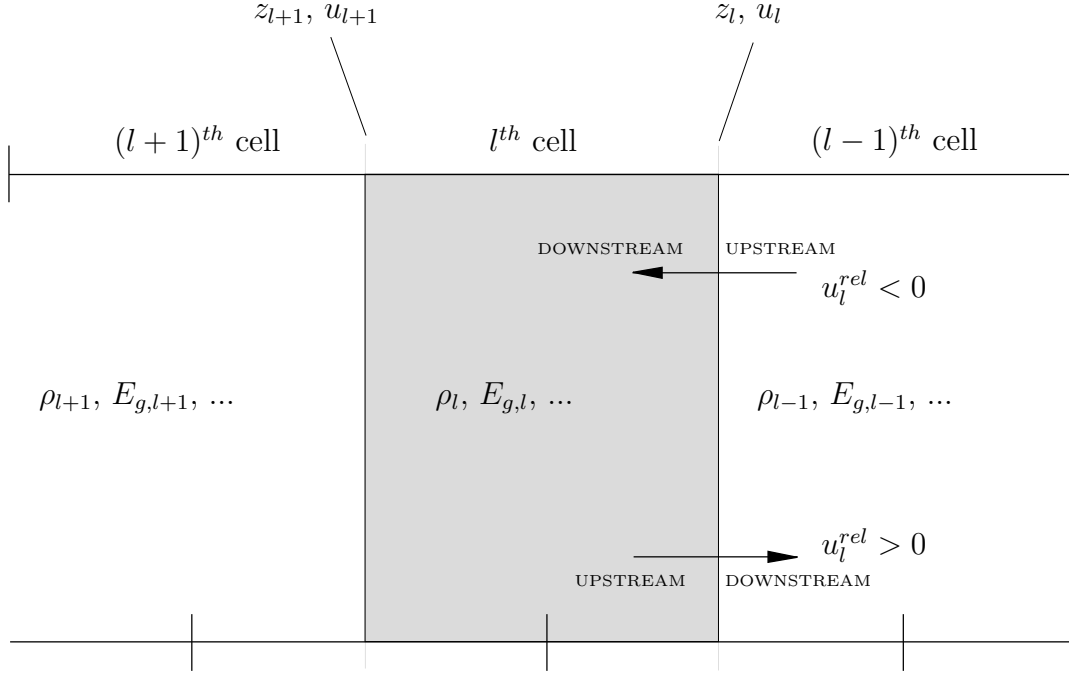


Figure 3.4: The donor-cell advection scheme is visualized here. If the relative velocity in the l -th cell u_l^{rel} is positive, then the flow is outward directed with respect to the cell, and vice versa. Clearly also the upstream and downstream regions depend on the flow direction.

In the case of the continuity equation, the only quantity which is calculated in the middle of the cell in the advection term is the density ρ (compare (2.3.1) and (3.3)). If one takes now the points discussed in ① and ② into account, the following expression for the advection term of the continuity equation is obtained,

$$\Delta(A_l u_l \rho_l) \Rightarrow \Delta(A_l u_l^{rel} \tilde{\rho}_l), \quad (3.3.17)$$

where $\tilde{\rho}_l$ is defined as follows,

$$\tilde{\rho}_l = \begin{cases} \rho_l & \text{if } u_l^{rel} > 0 \\ \rho_{l-1} & \text{if } u_l^{rel} < 0 \end{cases}. \quad (3.3.18)$$

The final discretized continuity equation then can be written as (compare with Dorfi & Breitschwerdt (2012)),

$$\frac{\delta(\rho_l \Delta V_l)}{\delta t} + \Delta(A_l u_l^{rel} \tilde{\rho}_l) = 0. \quad (3.3.19)$$

3.3.4 Discretization of the equation of motion

The next equation which will be discretized is the equation of momentum (2.4.1). To avoid confusion here, two different quantities must be distinguished. The *discretized momentum density* stored in the finite volume V_l is denoted as $\rho_l u_l$, while flux-related properties clearly need to include the relative velocity u_l^{rel} , because these quantities must take into account the movement of the cell border. For being able to discretize the equation of momentum, one needs to know how the gradient of a scalar function $f(z)$ is calculated in the fluxtube geometry defined in (2.11.1). The only thing which must be known here is that the covariant derivative reduces to the ordinary derivative for scalar functions, consequently one can write,

$$\nabla f(z) = \begin{pmatrix} \frac{\partial f(z)}{\partial z} \\ 0 \\ 0 \end{pmatrix}. \quad (3.3.20)$$

Furthermore one must take into account, that the momentum density $\rho_l u_l$ is a vector quantity and therefore defined at the grid boundary. Consequently all vector quantities in the equation of motion (e.g. the mass flux $\rho_l A_l u^{rel}$ or the gravitational force $\rho_l \nabla \phi$) should therefore also be defined at the grid boundary. This can be achieved by interpolating these vectors by calculating the mean values. This operation is denoted by a bar over the quantity as shown in the subsequent expression,

$$\bar{X}_l := \frac{1}{2}(X_l + X_{l+1}). \quad (3.3.21)$$

After collecting the recent results and applying the discretized versions of the volume term (3.3.7) and the advection term (3.3.12), the equation of momentum in volume-

integrated form becomes to (compare with Dorfi & Breitschwerdt (2012)),

$$\frac{\partial \rho \mathbf{u}}{\partial t} + \nabla \cdot (\rho \mathbf{u} \otimes \mathbf{u}) + \nabla (p_g + p_c + p_w) + \rho \nabla \phi - \mathbf{u}_Q = 0$$

(integration over volume ΔV_l and discretization)

$$\frac{\delta(\bar{\rho}_l u_l \Delta V_l)}{\delta t} + \Delta(\bar{A}_l u_l^{rel} \tilde{\rho}_l \tilde{u}_l) + \Delta(p_{g,l} + p_{c,l} + p_{w,l}) A_l + \bar{\rho}_l A_l \Delta \phi_l - u_{Q,l} \Delta V_l = 0 .$$

(3.3.22)

The discretized pre-factor of the artificial viscosity $\mu_{Q,l}$ (3.2.1) and the discrete artificial momentum transfer $u_{Q,l}$ (according to (3.2.12)) have the following form,

$$\mu_Q = -q_1 l_q c_s + q_2 l_q^2 \min(\nabla \cdot \mathbf{u}, 0)$$

(integration over volume ΔV_l and discretization)

$$\mu_{Q,l} = q_1 l_q c_{s,l} - q_2 l_q^2 \min\left(\frac{\Delta(A_l u_l)}{\Delta V_l}, 0\right) ,$$

(3.3.23)

$$(3.3.24)$$

$$u_Q = \frac{1}{A^{3/2}} \frac{\partial}{\partial z} \left[A^{1/2} \mu_Q \rho \frac{\partial(Au)}{\partial z} \left(\frac{\partial u}{\partial z} - \frac{1}{3} \frac{\partial(Au)}{\partial z} \right) \right]$$

(integration over volume ΔV_l and discretization)

$$u_{Q,l} \Delta V_l = -\frac{1}{A_l^{1/2}} \Delta \left[\bar{A}_l^{3/2} \mu_{Q,l} \rho_l \frac{\Delta(A_l u_l)}{\Delta V_l} \left(\frac{\Delta u_l}{\Delta z_l} - \frac{1}{3} \frac{\Delta(A_l u_l)}{\Delta V_l} \right) \right] .$$

(3.3.25)

The interpolated \bar{A}_l in the last expression is due to the fact, that all other quantities are defined at the grid cell boundary, and so it is straightforward to interpolate A_l to fit better to the other discretized quantities.

3.3.5 Discretization of the gas energy density equation

It is continued now with the discretization of the gas energy density equation (3.2.16). Applying the discretization of the volume term and the advection term as before and keeping in mind the numerical details for the advection term ① and ②, the following discretization is achieved,

$$\frac{\partial E_g}{\partial t} + \nabla \cdot (E_g \mathbf{u}) + p_g \nabla \cdot \mathbf{u} - \rho \epsilon_Q = \Gamma - \Lambda$$

(integration over volume ΔV_l and discretization)
 \implies

$$\frac{\delta(E_{g,l} \Delta V_l)}{\delta t} + \Delta(A_l u_l^{rel} \tilde{E}_{g,l}) + p_{g,l} \Delta(A_l u_l) - \epsilon_{Q,l} \rho_l \Delta V_l = \Gamma - \Lambda . \quad (3.3.26)$$

The artificial specific energy dissipation ϵ_Q (3.2.13) is discretized as follows (compare with Dorfi & Breitschwerdt (2012)),

$$\epsilon_Q = -\frac{3 \mu_Q}{2 A} \frac{\partial(Au)}{\partial z} \left[\frac{\partial u}{\partial z} - \frac{1}{3A} \frac{\partial(Au)}{\partial z} \right]^2$$

(integration over volume ΔV_l and discretization)
 \implies

$$\epsilon_{Q,l} \rho_l \Delta V_l = \frac{3}{2} \mu_{Q,l} \rho_l \Delta(A_l u_l) \left[\frac{\Delta u_l}{\Delta z_l} - \frac{1}{3} \frac{\Delta A_l u_l}{\Delta V_l} \right]^2 . \quad (3.3.27)$$

3.3.6 Discretization of the cosmic ray energy density equation

The next equation which is discretized, is the cosmic ray energy density equation (2.10.14). Analogously to the other equations the discretized form of this equation is given in the following expression,

$$\frac{\partial E_c}{\partial t} + \nabla \cdot (E_c (\mathbf{u} + \gamma_c \mathbf{v}_A)) + p_c \nabla \cdot \mathbf{u} - \mathbf{v}_A \cdot \nabla p_c = \nabla \cdot (\kappa \nabla E_c)$$

(integration over volume ΔV_l and discretization)
 \implies

$$\begin{aligned} \frac{\delta E_{c,l} \Delta V_l}{\delta t} + \Delta(A_l \tilde{E}_{c,l}(u_l^{rel} + \gamma_c v_{A,l})) + (\gamma_c - 1) E_{c,l} \Delta(A_l u_l) - (\gamma_c - 1) v_{A,l} \Delta E_{c,l} A_l \\ = \Delta \left(A_l \kappa \frac{\Delta E_{c,l}}{\Delta z_l} \right). \end{aligned} \quad (3.3.28)$$

3.3.7 Discretization of the wave energy density equation

The last physical equation left for discretization is the wave energy density equation or energy exchange equation (2.10.15), which has the following discretized form,

$$\begin{aligned} \frac{\partial E_w}{\partial t} + \nabla \cdot (E_w(\mathbf{u} + \mathbf{v}_A)) + p_w \nabla \cdot \mathbf{u} + \mathbf{v}_A \cdot \nabla p_w = 0 \\ \text{(integration over volume } \Delta V_l \text{ and discretization)} \end{aligned}$$

$$\begin{aligned} \frac{\delta E_{w,l} \Delta V_l}{\delta t} + \Delta(A_l \tilde{E}_{w,l}(u_l^{rel} + v_{A,l})) + (\gamma_w - 1) E_{w,l} \Delta(A_l u_l) - (\gamma_w - 1) v_{A,l} \Delta E_{w,l} A_l \\ = 0. \end{aligned} \quad (3.3.29)$$

3.4 Implicit method

Basically there exist two different approaches for solving a system of *time-dependent* differential equations, namely

- Explicit methods, and
- Implicit methods.

The major difference between implicit and explicit methods is the way how the solution at a later time is obtained. An explicit integration scheme uses the solution of the system at the old time for calculating the new solution. If the solution vector at the l -th grid point is denoted as \mathbf{X}_l , then in general an explicit discretization of a set of equation

would look like,

$$\mathbf{X}_l = (X_{l,1}, X_{l,2}, \dots, X_{l,M}) , \quad (3.4.1)$$

$$\mathbf{X} = (\mathbf{X}_1, \mathbf{X}_2, \dots, \mathbf{X}_N) , \quad (3.4.2)$$

$$\frac{\mathbf{X}^{(new)} - \mathbf{X}^{(old)}}{\delta t} = \mathcal{F}(\mathbf{X}^{(old)}) , \quad (3.4.3)$$

where N is the number of grid points and M the number of variables. The solution vector \mathbf{X} has after having a look at (3.4.2) the dimension $N \times M$. At the new time $\mathbf{X}^{(new)}$ can be obtained straightforward by simply writing,

$$\mathbf{X}^{(new)} = \mathbf{X}^{(old)} + \delta t \mathcal{F}(\mathbf{X}^{(old)}) . \quad (3.4.4)$$

This shows, that the new values are obtained by simply extrapolating the solution at the old time to the new time. The problem with explicit schemes is the strong dependence on the time step δt (see e.g. Feuchtinger (1989)). Solving differential equations numerically with an explicit method impose an upper limit on the time step δt (otherwise the numerical method is unstable), this condition is called *Courant-Friedrichs-Lewy (CFL)-condition* and reads as follows (see e.g. LeVeque et al. (1998), p. 52),

$$\delta t \leq \frac{\Delta z}{|u| + c_s} , \quad (3.4.5)$$

where c_s is the *speed of sound*. This condition is equivalent to the following condition (see LeVeque et al. (1998), p. 52):

The numerical domain of dependence must not be greater than the true domain of the system of differential equations. In the limit of $\delta t \rightarrow 0$ and $\Delta z \rightarrow 0$ the computational domain of dependence should change to the true domain of dependence.

It should be noted that the CFL-condition is only a *necessary* condition but not sufficient, this means that an explicit method cannot be stable, but a method with a satisfied CFL-condition *might* be convergent, but nothing can be said for sure without doing further stability analysis.

On the contrary, an implicit method solves the system of equations by using solutions from the old *and* the new time. This can be written in the following way,

$$\frac{\mathbf{X}^{(new)} - \mathbf{X}^{(old)}}{\delta t} = \mathcal{F}(\mathbf{X}^{(old)}, \mathbf{X}^{(new)}), \quad (3.4.6)$$

The problem of equations of the form (3.4.6) is, that such systems are in the most cases *nonlinear* and cannot be solved explicitly. Such systems of equations can be solved iteratively by root searching algorithms, e.g. by a *Newton-Raphson iteration*. For this purpose the system of equations at the current time (denoted by superscript (n)) and for a certain grid point l is rewritten as follows,

$$\mathcal{G}_{m,l}(\mathbf{X}^{(n)}) = 0, \quad m \in [1, M], \quad (3.4.7)$$

where $\mathcal{G}_{m,l}$ is a set of M equations per grid point l and $\mathbf{X}^{(n)}$ denotes the set of variables at the current time. The whole system of equations consists of $N \times M$ equations \mathcal{G} , because for every grid point there are M unknown variables. A solution at the new time (denoted by superscript $(n+1)$) must obey the same set of equations \mathcal{G}_m for every grid point l ,

$$\mathcal{G}_{m,l}(\mathbf{X}^{(n+1)}) = 0, \quad m \in [1, M]. \quad (3.4.8)$$

Due to the non-linearity of the equations \mathcal{G}_m , the system cannot be solved explicitly in general, but it can be computed iteratively to first order, by expanding it in a *Taylor series* around the solution at the new time $\mathbf{X}^{(n+1)}$. For every grid point l , the Taylor expansion looks like,

$$\mathcal{G}_{m,l}(\mathbf{X}^{(n+1)}) = \mathcal{G}_{m,l}(\mathbf{X}^{(n)}) + \underbrace{\frac{\partial \mathcal{G}_{m,l}}{\partial \mathbf{X}_l^{(n)}}}_{=\mathbf{J}} (\mathbf{X}_l^{(n+1)} - \mathbf{X}_l^{(n)}) = 0. \quad (3.4.9)$$

The term denoted by \mathbf{J} is the *Jacobi-matrix*. Applying this Taylor expansion for every grid point l make clear that \mathbf{J} has the dimension $(N \cdot M \times N \cdot M)$. Inverting that matrix allows one to rewrite equation (3.4.9) for every grid point l in the following way,

$$\delta \mathbf{X}_l = \mathbf{X}_l^{(n+1)} - \mathbf{X}_l^{(n)}, \quad (3.4.10)$$

$$\delta \mathbf{X}_l = -\mathbf{J}_{ml}^{-1} \mathcal{G}_{m,l}(\mathbf{X}^{(n)}). \quad (3.4.11)$$

This form (3.4.11) is used to iteratively solve the system of equations with a Newton-Raphson iteration. Repeating this procedure leads to a more accurate solution vector for the new time $\mathbf{X}^{(n)}$. The iteration is halted, if a certain accuracy ϵ is achieved (see LeVeque et al. (1998), p. 209),

$$\min \left(\frac{|\delta X_{m,l}|}{|X_{m,l}| + \eta_{m,l}} \right) \leq \epsilon . \quad (3.4.12)$$

The constants $\eta_{m,l}$ are introduced to circumvent problems, which arise if $|X_{m,l}|$ is zero.

3.4.1 Boundary Conditions

The boundary conditions of the set of discretized physical equations are specified together with the grid boundary conditions as defined in (3.1.13). As it will be clear in the next section 3.4.2, each variable in a cell is connected to the next two neighbouring cells on each side. This so-called *5-point stencil* clearly cannot be adopted for the boundaries, because otherwise the computational domain would be infinite.

There exists a huge amount of different possible boundary conditions, in this thesis there are two different types which are used:

- *Fixed boundary values:* The innermost ($l = N$) and outermost ($l = 1$) grid points are set to fixed value $\mathbf{X}_{bound,inner}$ and $\mathbf{X}_{bound,outer}$, respectively,

$$\Delta \mathbf{X}_1 = \Delta \mathbf{X}_N = 0 , \quad (3.4.13)$$

\Rightarrow

$$\mathbf{X}_1 - \mathbf{X}_{bound,outer} = 0 , \quad (3.4.14)$$

$$\mathbf{X}_N - \mathbf{X}_{bound,inner} = 0 . \quad (3.4.15)$$

- *Zero gradient for quantities at the boundary:* If the gradients should be zero e.g. at the outer boundary, this can be written as,

$$\left. \frac{\partial \mathbf{X}}{\partial z} \right|_{outer} = 0 , \quad (3.4.16)$$

\Rightarrow

$$\mathbf{X}_2 - \mathbf{X}_1 = 0 . \quad (3.4.17)$$

According to section 1.3, the Kompaneets approximation is used to calculate the *variable inner boundary values*. Two different situations are implemented:

- *No feedback of the galactic wind*: The quantities in the superbubble, especially ρ , E_g and E_c are *not influenced* by the galactic wind.
- *Non-vanishing feedback of the galactic wind*: The mass-flow as well as the CR flow will decrease the cosmic ray energy density E_c and also the density ρ in the cavity and therefore the gas energy density E_g .

In general the variable boundary conditions at the new time (superscript “(new)”) are computed in the following way (using the quantities in equation (1.3.22),

$$\mathbf{X}_{\text{bound,inner}}^{(\text{new})} = \begin{cases} \rho_{\text{bound,inner}}^{(\text{new})} & = \rho_{\text{bound,inner}}^{(\text{old})} + \rho_{\text{gain}} - \rho_{\text{loss}} \\ E_{g,\text{bound,inner}}^{(\text{new})} & = E_{g,\text{bound,inner}}^{(\text{old})} + E_{g,\text{gain}} - E_{g,\text{loss}} \\ E_{c,\text{bound,inner}}^{(\text{new})} & = E_{c,\text{bound,inner}}^{(\text{old})} + E_{c,\text{gain}} - E_{c,\text{loss}} \\ E_{w,\text{bound,inner}}^{(\text{new})} & = E_{w,\text{bound,inner}}^{(\text{old})} \end{cases}, \quad (3.4.18)$$

$$0 = u_N - u_{N-1}. \quad (3.4.19)$$

Equation (3.4.19) is equivalent to a vanishing velocity gradient at the inner boundary (compare with (3.4.16)). The other quantities ρ_N , $E_{g,N}$, $E_{c,N}$ and $E_{w,N}$ are set to fixed values (compare with (3.4.13)), which are variable in time according to the Kompaneets solution. Supernova explosions supply energy and generate CRs, in general all quantities which increase any quantity within the superbubble are denoted with subscript “*gain*”. On the other hand, the galactic wind will carry away a certain amount of energy and mass, therefore these parts are referred to with subscript “*loss*”.

New mass is inserted into the superbubble by various processes such as stellar winds, supernova explosions, etc. In starbursts this is a substantial and therefore a not negligible part of the overall mass in a superbubble. Coming back to the case of an ordinary superbubble created by explosions of a few stars of an OB-association, the part of mass injected by the stars or by galactic winds can be ignored with respect to the mass swept up by the shell (for details see e.g. Ellison & Meyer (1999)). Because of that, mass insertion is not taken into account in these calculation, $\rho_{\text{gain}} = 0$.

As already mentioned in section 1.3, the CR energy produced by a single supernova is approximately 10%. Further it is assumed, that the remaining 90% of all supernova

explosions are *completely thermalized* at the time the superbubble has grown to its final volume V_0 . Therefore the gas and CR energy density gains caused by supernova explosions are computed as follows,

$$E_{g,gain} = 0.9 \frac{E_{SN}}{V_0} , \quad (3.4.20)$$

$$E_{c,gain} = 0.1 \frac{E_{SN}}{V_0} . \quad (3.4.21)$$

Finally, the wave energy density E_w is assumed to be not influenced by supernova explosions.

In the case of no galactic wind feedback all quantities referring to mass loss or energy loss, are set to zero. Otherwise, the various loss terms can be determined in the following way. One result of the Kompaneets approximation is a physically motivated initial cross section of the fluxtube A_0 . The mass flux M_{loss} and the resulting mass density ρ_{loss} per timestep δt through this surface can be calculated as follows,

$$M_{loss} = \rho_{bound,in}^{(old)} A_0 u_N \delta t , \quad (3.4.22)$$

$$\rho_{loss} = \frac{M_{loss}}{V_0} . \quad (3.4.23)$$

Then the gas energy density loss per timestep $E_{g,loss}$ can be obtained by calculating,

$$E_{g,loss} = A_0 u_N \delta t \frac{0.9 E_{SN}}{V_0} . \quad (3.4.24)$$

The CR energy loss is determined by using the expression for the cosmic ray flux \mathbf{F}_c , equation (2.6.2),

$$F_{c,N} = \gamma_c (u_N + v_{A,N}) E_{c,bound,inner}^{(new)} - \kappa \frac{\Delta E_{c,N}}{\Delta z_N} . \quad (3.4.25)$$

Then the cosmic ray energy density loss per timestep $E_{c,loss}$ can be calculated as follows,

$$E_{c,loss} = A_0 u_N \delta t F_{c,N} . \quad (3.4.26)$$

3.4.2 Structure and Inversion of the Jacobi-Matrix

In this section the structure of the Jacobi matrix \mathbf{J} will be discussed. Further the inversion process is introduced schematically. More details to the inversion process can be found e.g. in LeVeque et al. (1998).

First the discretized physical equations and the grid equation (3.1.11) need to be considered in more detail. The discretized advection term of the equation of motion (3.3.22) has fully written out the following form,

$$\begin{aligned} \Delta(A_l u_l^{rel} \tilde{\rho}_l \tilde{u}_l) &= \overline{A_{l-1} u_{l-1}^{rel} \rho_{l-1}} \tilde{u}_{l-1} - \overline{A_l u_l^{rel} \tilde{\rho}_l} \tilde{u}_l \\ &= \frac{1}{2}(A_{l-1} u_{l-1}^{rel} \rho_{l-1} + A_l u_l^{rel} \tilde{\rho}_l) \tilde{u}_{l-1} - \frac{1}{2}(A_l u_l^{rel} \tilde{\rho}_l + A_{l+1} u_{l+1}^{rel} \rho_{l+1}) \tilde{u}_l. \end{aligned} \quad (3.4.27)$$

Recalling the donor-cell scheme (3.3.18), it is possible (in the case of $\mathbf{u}^{rel} < 0$) to obtain the following expression for the discretized advection term,

$$\Delta(\overline{A_l u_l^{rel} \tilde{\rho}_l} \tilde{u}_l) = \frac{1}{2}(A_{l-1} u_{l-1}^{rel} \rho_{l-2} + A_l u_l^{rel} \rho_{l-1}) u_{l-2} - \frac{1}{2}(A_l u_l^{rel} \rho_{l-1} + A_{l+1} u_{l+1}^{rel} \rho_l) u_{l-1} \quad (3.4.28)$$

In this form it is easy to see, that only quantities from the grid cells $(l-2)$, $(l-1)$, (l) , and $(l+1)$ are used.

The next equation which is considered in more detail is the grid equation. It is easy to see from the expressions (3.1.9), (3.1.10) and (3.1.11) that only variables are used for calculating the actual point distribution n_l , which are from the grid points $(l-2, l-1, l, l+1, l+2)$. All other discretized physical equations only have contributions from the current grid cell and its next neighbours. Hence, in general it can be said that only variables enter the discretized equations, which are defined at the grid points $(l-2, l-1, l, l+1, l+2)$. In other words, the resulting $(N \cdot M \times N \cdot M)$ -Jacobi-matrix is mostly filled with zeros, more precisely the structure of \mathbf{J} is *block-pentadiagonal* (compare LeVeque et al. (1998), p. 310). The system of equations (3.4.9) then can be written as

(using for the variables at each grid point \mathbf{X}_l the notation as introduced in (3.4.10)),

$$\begin{pmatrix} \mathbf{A}_{1,1} & \mathbf{A}_{1,2} & \mathbf{A}_{1,3} & & & & \\ \mathbf{A}_{2,1} & \mathbf{A}_{2,2} & \mathbf{A}_{2,3} & \mathbf{A}_{2,4} & & & \\ \mathbf{A}_{3,1} & \mathbf{A}_{3,2} & \mathbf{A}_{3,3} & \mathbf{A}_{3,4} & \mathbf{A}_{3,5} & & \\ \ddots & \ddots & \ddots & \ddots & \ddots & & \\ & \mathbf{A}_{l,l-2} & \mathbf{A}_{l,l-1} & \mathbf{A}_{l,l} & \mathbf{A}_{l,l+1} & \mathbf{A}_{l,l+2} & \\ & & \ddots & \ddots & \ddots & \ddots & \\ & & & \mathbf{A}_{N,N-2} & \mathbf{A}_{N,N-1} & \mathbf{A}_{N,N} & \end{pmatrix} \cdot \begin{pmatrix} \delta \mathbf{X}_1 \\ \delta \mathbf{X}_2 \\ \delta \mathbf{X}_3 \\ \vdots \\ \delta \mathbf{X}_l \\ \vdots \\ \delta \mathbf{X}_N \end{pmatrix} = - \begin{pmatrix} \mathcal{G}_{m,1}(\mathbf{X}^{(n)}) \\ \mathcal{G}_{m,2}(\mathbf{X}^{(n)}) \\ \mathcal{G}_{m,3}(\mathbf{X}^{(n)}) \\ \vdots \\ \mathcal{G}_{m,l}(\mathbf{X}^{(n)}) \\ \vdots \\ \mathcal{G}_{m,N}(\mathbf{X}^{(n)}) \end{pmatrix}. \quad (3.4.29)$$

where $\mathbf{A}_{l,l+1}$ are $(M \times M)$ -matrices and defined as,

$$\mathbf{A}_{l,l+1} = \frac{\partial \mathcal{G}_{m,l}}{\partial z_{m,l+1}} = \begin{pmatrix} \frac{\partial \mathcal{G}_{1,l}}{\partial z_{1,l+1}} & \frac{\partial \mathcal{G}_{1,l}}{\partial z_{2,l+1}} & \cdots & \frac{\partial \mathcal{G}_{1,l}}{\partial z_{M,l+1}} \\ \frac{\partial \mathcal{G}_{2,l}}{\partial z_{1,l+1}} & \frac{\partial \mathcal{G}_{2,l}}{\partial z_{2,l+1}} & \cdots & \frac{\partial \mathcal{G}_{2,l}}{\partial z_{M,l+1}} \\ \vdots & \vdots & & \vdots \\ \frac{\partial \mathcal{G}_{M,l}}{\partial z_{1,l+1}} & \frac{\partial \mathcal{G}_{M,l}}{\partial z_{2,l+1}} & \cdots & \frac{\partial \mathcal{G}_{M,l}}{\partial z_{M,l+1}} \end{pmatrix}. \quad (3.4.30)$$

The inversion of the system (3.4.29) can be done in several steps, including a forward elimination and a subsequent back-substitution. The procedure of inverting the matrix is explained now briefly:

1. The first line is multiplied with $\mathbf{A}_{1,1}^{-1}$ and solved for $\delta \mathbf{X}_1$. The resulting equation is given by,

$$\delta \mathbf{X}_1 = - \underbrace{\mathbf{A}_{1,1}^{-1} \mathbf{A}_{1,2}}_{:=\mathbf{U}_1} \delta \mathbf{X}_2 - \underbrace{\mathbf{A}_{1,1}^{-1} \mathbf{A}_{1,3}}_{:=\mathbf{V}_1} \delta \mathbf{X}_3 - \underbrace{\mathbf{A}_{1,1}^{-1} \mathcal{G}_{m,1}(\mathbf{X}^{(n)})}_{:=\mathbf{w}_1}. \quad (3.4.31)$$

2. The result of step 1 is substituted into the second line and then the procedure is repeated for every line of the system (3.4.29) such that the correction vectors \mathbf{X}_l

can be written in the form,

$$\delta \mathbf{X}_l = \mathbf{U}_l \delta \mathbf{X}_{l+1} + \mathbf{V}_l \delta \mathbf{X}_{l+2} + \mathbf{w}_l . \quad (3.4.32)$$

3. The next step is to take the *boundary conditions* of the system into account. If the boundary conditions are adopted as it has been explained in section 3.4.1, then due to the outer boundary conditions the set of variables \mathbf{X}_0 and \mathbf{X}_{-1} do not occur and because of the inner boundary conditions the set of variables \mathbf{X}_{N+1} and \mathbf{X}_{N+2} vanish. This leads straightforward to the following results,

$$\mathbf{A}_{1,-1} = \mathbf{A}_{1,0} = 0 , \quad (3.4.33)$$

$$\mathbf{A}_{N,N+1} = \mathbf{A}_{N,N+2} = 0 . \quad (3.4.34)$$

Including these vanishing sub-matrices, it is possible to define *iteration formulas* for the expressions \mathbf{U}_l , \mathbf{V}_l and \mathbf{w}_l in (3.4.32), namely (see LeVeque et al. (1998), p. 311),

$$\mathbf{U}_l = \mathbf{Y}_l [(\mathbf{A}_{l,l-2} \mathbf{U}_{l-2} + \mathbf{A}_{l,l-1}) \mathbf{V}_{l-1} + \mathbf{A}_{l,l+1}] , \quad (3.4.35)$$

$$\mathbf{V}_l = \mathbf{Y}_l \mathbf{A}_{l,l+2} , \quad (3.4.36)$$

$$\mathbf{w}_l = \mathbf{Y}_l \left[-\mathcal{G}_{m,l}(\mathbf{X}^{(n)}) - (\mathbf{A}_{l,l-2} \mathbf{U}_{l-2} + \mathbf{A}_{l,l-1}) \mathbf{w}_{l-1} - \mathbf{A}_{l,l-2} \mathbf{w}_{l-2} \right] , \quad (3.4.37)$$

where \mathbf{Y}_l is defined as follows,

$$\mathbf{Y}_l = [(\mathbf{A}_{l,l-2} \mathbf{U}_{l-2} + \mathbf{A}_{l,l-1}) \mathbf{U}_{l-1} + \mathbf{A}_{l,l-2} \mathbf{V}_{l-2} + \mathbf{A}_{l,l}]^{-1} . \quad (3.4.38)$$

4. The starting values \mathbf{U}_1 , \mathbf{V}_1 and \mathbf{w}_1 are already given by (3.4.31), thus it is possible to proceed until the last grid point $l = N$. By recalling the inner boundary conditions (3.4.34) and taking a closer look at (3.4.36) and (3.4.35), it is easy to see that,

$$\mathbf{V}_{N-1} = \mathbf{V}_N = 0 \quad \Rightarrow \quad \mathbf{U}_N = 0 . \quad (3.4.39)$$

Consequently, $\delta \mathbf{X}_N = \mathbf{w}_N$ follows directly from equation (3.4.32).

5. With $\mathbf{V}_{N-1} = 0$ and known $\delta \mathbf{X}_N$ the recursion formula (3.4.32) can be used to

calculate $\delta\mathbf{X}_{N-1}$,

$$\delta\mathbf{X}_{N-1} = U_{N-1}\delta\mathbf{X}_N + \mathbf{w}_{N-1} . \quad (3.4.40)$$

These two values are sufficient to fully apply (3.4.32) to calculate by backward recursion all remaining corrections $\delta\mathbf{X}_l$.

After the inversion of the Jacobi-matrix \mathbf{J} , the corrections are applied to calculate the new solution vector $\mathbf{X}^{(n+1)}$. If the accuracy of the solution not sufficient, the inversion procedure is repeated, until the condition (3.4.12) is obeyed or if it is clear, that no solution can be found, because the Newton-Raphson iteration diverges.

4 Initial Model

The implicit nature of the discretized equations (3.3.19) - (3.3.29) makes it necessary to already have a *full solution*, when starting the calculations (see LeVeque et al. (1998), p. 283). This can be seen by recalling that the solution at the new time is obtained by a Newton-Raphson iteration. Therefore it is necessary that the *convergence radius* of the new solution incorporates the initial solution. Creating such an initial model can be very complicated, in the case of galactic winds it can be done in a rather simple way.

4.1 Steady-state Initial Model

In Breitschwerdt et al. (1991) the time dependence on the physical equations (2.10.11) - (2.10.15) has been dropped, this enables one to find analytic expressions for the density ρ , the velocity u and the pressures (equivalent to energy densities) p_g , p_c and p_w . Without further discussions (for details see Breitschwerdt et al. (1991)) the time-independent galactic wind equations have the following form (taking the assumptions and simplifications in section 2.8 and the fluxtube geometry into account),

$$\rho u A = \text{const.} , \quad (4.1.1)$$

$$\frac{dp_g}{dz} = \gamma_g \frac{p_g}{\rho} \frac{d\rho}{dz} , \quad (4.1.2)$$

$$\frac{dp_c}{dz} = \gamma_c \frac{p_c}{\rho} \left(\frac{M_A + \frac{1}{2}}{M_A + 1} \right) \frac{d\rho}{dz} , \quad (4.1.3)$$

$$\frac{dp_w}{dz} = \frac{1}{2(M_A + 1)} \left[(3M_A + 1) \frac{p_w}{\rho} \frac{d\rho}{dz} - \frac{dp_c}{dz} \right] , \quad (4.1.4)$$

$$\frac{1}{u} (u^2 - c_*^2) \frac{du}{dz} = c_*^2 \frac{1}{A} \frac{dA}{dz} - \frac{\partial \phi}{\partial z} , \quad (4.1.5)$$

where ϕ is the gravitational potential as defined in (2.9.4). The *compound sound speed* c_* and the *Alfvén Mach number* M_A are defined as follows,

$$M_A = \frac{|u|}{|v_A|}, \quad (4.1.6)$$

$$c_* = \gamma_g \frac{p_g}{\rho} + \gamma_c \frac{p_c}{\rho} \frac{\left(M_A + \frac{1}{2}\right)^2}{(M_A + 1)^2} + \frac{p_w}{\rho} \frac{(3M_A + 1)^2}{(M_A + 1)}. \quad (4.1.7)$$

This set of equation has several types of solutions, which can be represented and characterized by a *flow topology chart*. Such a flow topology is shown in Figure 4.1.

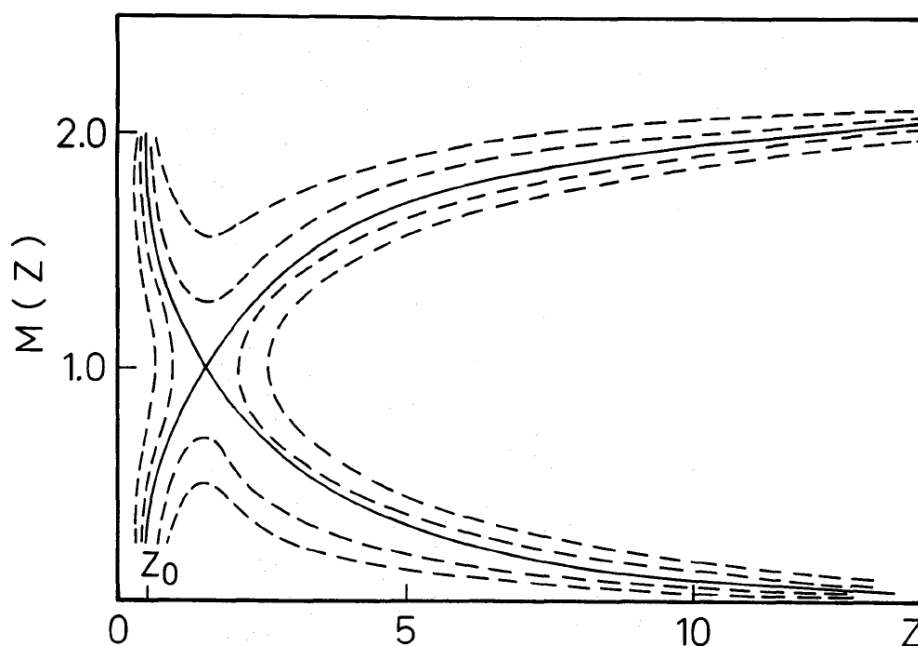


Figure 4.1: *Flow topology of a galactic wind as described in the time independent equations given above (adiabatic galactic winds). The galactic wind flow is characterized by the increasing full line (from Breitschwerdt et al. (1991)).*

In Figure 4.1, it can be seen that the galactic wind solution must go through the *critical point* (X-type singularity), otherwise no outflow of the gas is possible. Integral curves below the critical point correspond to solutions, which are denoted as *Breeze solutions*. At the critical point, the solution has a *subsonic - supersonic transition* ($M_A > 1$ for $z/z_0 > 1$). Therefore, because of the definition of a critical point (e.g. in Jordan & Smith (2007)) it is required, that the left-hand-side (LHS) and RHS of equation (4.1.5) vanish simultaneously, which results in the following conditions for the existence of a

galactic wind,

$$u^2 = c_*^2, \quad (4.1.8)$$

$$c_*^2 \frac{1}{A} \frac{dA}{dz} = \frac{\partial \phi}{\partial z}. \quad (4.1.9)$$

There are two possibilities for solving the system of time-independent equations with including the conditions (4.1.8) and (4.1.9):

- *Guessing the critical point* and then integrating inwards and outwards. The disadvantage of this integration method is, that the inner and outer boundary conditions need to be matched, this requires a good guess of the critical point.
- *Direct integration* and then trying to find the critical point by integration and subsequent iterative variation of the velocity at the inner boundary u_0 . The second approach is easier to implement and has therefore been used by the authors of Breitschwerdt et al. (1991) to calculate the initial models, which are used as initial models for the implicit scheme.

The density profile, the velocity profile as well as the energy profiles for E_g , E_c and E_w , which are obtained by the integration of the steady-state equations, is shown in Figure 4.2. The inner and outer boundary conditions of this calculation are given by (compare with section 3.4.1),

$$\text{(inner boundary conditions)} = \begin{cases} u_N - u_{N-1} = 0 & , \text{ (vanishing velocity gradient)} \\ \rho_N - X_{bound,inner}^\rho = 0 & , \text{ (fixed value)} \\ E_{g,N} - X_{bound,inner}^{E_g} = 0 & , \text{ (fixed value)} \\ E_{c,N} - X_{bound,inner}^{E_c} = 0 & , \text{ (fixed value)} \\ E_{w,N} - X_{bound,inner}^{E_w} = 0 & , \text{ (fixed value)} \end{cases} , \quad (4.1.10)$$

$$\text{(outer boundary conditions)} = \begin{cases} u_1 - u_2 = 0 & , \text{ (vanishing velocity gradient)} \end{cases} . \quad (4.1.11)$$

Furthermore no diffusion is used in this model ($\kappa = 0$).

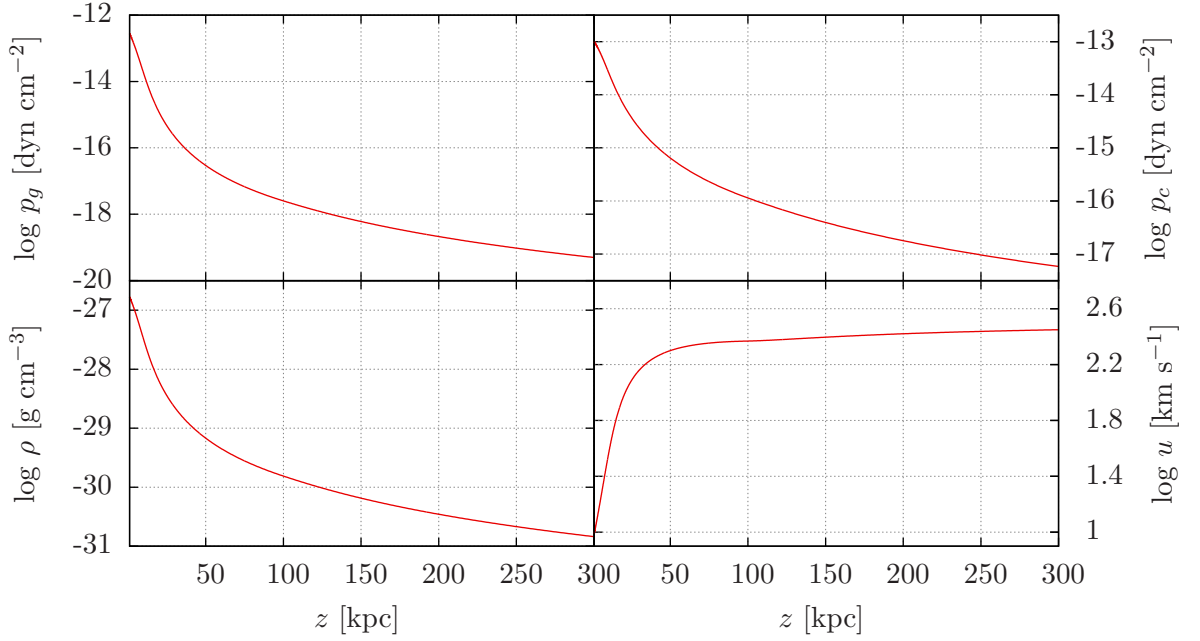


Figure 4.2: Initial profiles for ρ , u , p_g and p_c , based on the integration of the steady-state equation as it has been done by Breitschwerdt et al. (1991).

This initial model can be used to start a simulation of time-dependent galactic winds by varying the inner and/or outer boundary conditions.

The steady-state initial model used in the further calculations (see section 5) has the following values at the inner boundary and is denoted as **Model A**:

$$\left\{ \begin{array}{ll} p_{g,inner} & = 2.76 \cdot 10^{-13} \text{ dyn cm}^{-2} \quad (\text{initial gas pressure } p_g \text{ at inner boundary}) , \\ p_{c,inner} & = 1.00 \cdot 10^{-13} \text{ dyn cm}^{-2} \quad (\text{initial CR pressure } p_c \text{ at inner boundary}) , \\ p_{w,inner} & = 3.98 \cdot 10^{-16} \text{ dyn cm}^{-2} \quad (\text{initial wave pressure } p_g \text{ at inner boundary}) , \\ \rho_{inner} & = 1.67 \cdot 10^{-27} \text{ g cm}^{-3} \quad (\text{initial density } \rho \text{ at inner boundary}) , \\ u_{inner} & = 1.11 \cdot 10^1 \text{ km s}^{-1} \quad (\text{initial gas velocity } u \text{ at inner boundary}) . \end{array} \right. \quad (4.1.12)$$

4.2 Pseudo-Variation of Boundaries

From the practical point of view it is very inconvenient, if one always has to repeat this procedure as soon as different starting parameters are required (e.g. a different compu-

tational domain, different boundary values \mathbf{X}_{bound} or a different diffusion coefficient κ). Therefore it would be nice to be able to iterate from one initial model to another step by step. Indeed this can be done by so-called *pseudo-variations of boundary values*. These variations of variables are non-physical and only have a numerical significance.

In the following examples the various effects of different pseudo-variations are illustrated and briefly motivated. Some features of a astrophysical problem could occur outside of the computational domain, therefore it would be convenient to just 'drag' the innermost or outermost grid point to the desired position, while the adaptive grid adjusts to the varying size of the computational domain. Because the grid equation is simultaneously solved with the physical equations, this can be done without any major problems, as long as the rate at which the inner or outer boundaries are moved remains sufficiently small for obtaining a convergent Newton-Raphson iteration. In the following example (see Figure 4.3), the outer boundary z_1 has been moved from 300 kpc to 1000 kpc.

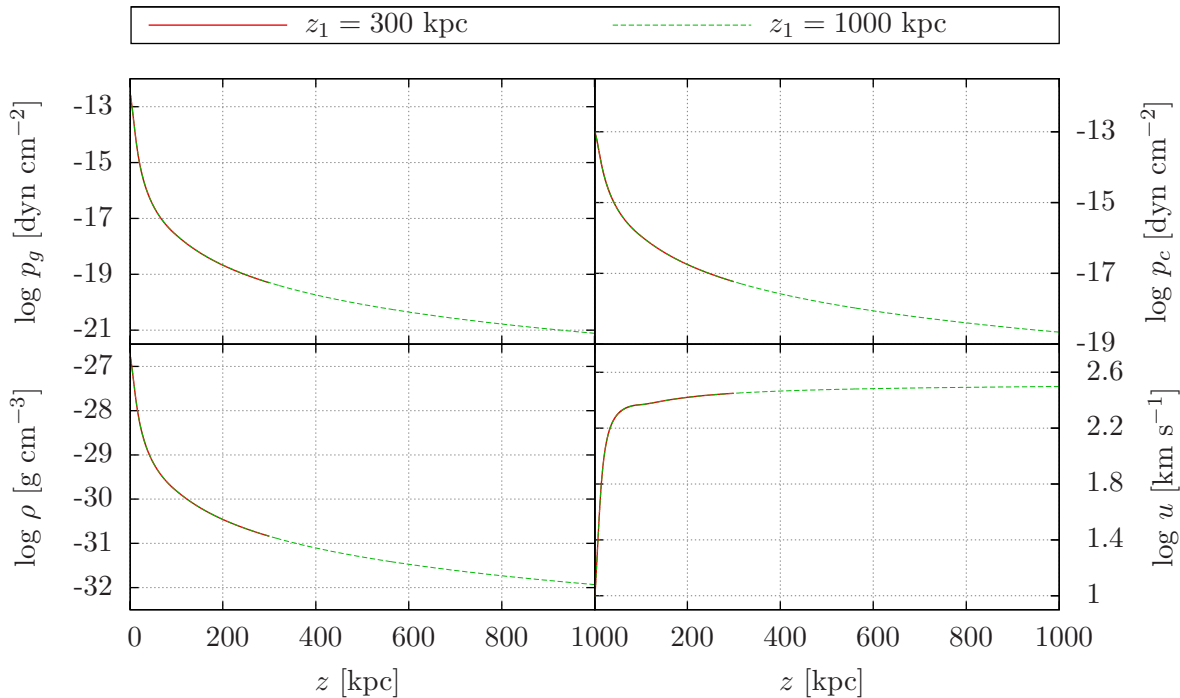


Figure 4.3: Variations of ρ , u , p_g and p_c with distance z from the galactic plane. The outermost grid-point has moved from 300 kpc to 1000 kpc.

Because the velocity gradient $\frac{\partial u}{\partial z}$ is nearly vanishing at $z = 300$ kpc as well as at $z = 1000$ kpc, the new velocity profile is virtually indistinguishable from the original profile. The other variables are not constrained at the outer boundary and therefore

have values according to the flow profile.

4.3 Quasi-hydrostatic initial model

An often used pseudo-variation (at least in this thesis) is the attempt to construct a *quasi-hydrostatic* initial model. The usual strategy is to take a starting solution, which already corresponds to a galactic wind. Based on this a time-dependent variable boundary condition is applied to study the behaviour of the flow. From the physical point of view it is better to let the galactic wind evolve into a hydrostatically stratified halo (see section 1.1). For this purpose it is necessary to reduce the flow velocity as much as possible, this can be achieved by reducing the wind-driving pressures p_g and p_c (equivalently E_g and E_c). The following parameters were used for obtaining profiles as shown in Figure 4.4,

$$\text{variations} = = \begin{cases} p_{g,inner}^{(old)} = 2.76 \cdot 10^{-13} \text{ dyn cm}^{-2} & \Rightarrow p_{g,inner}^{(new)} = 2.76 \cdot 10^{-14} \text{ dyn cm}^{-2} \\ p_{c,inner}^{(old)} = 1.00 \cdot 10^{-13} \text{ dyn cm}^{-2} & \Rightarrow p_{c,inner}^{(new)} = 1.00 \cdot 10^{-14} \text{ dyn cm}^{-2} \\ p_{w,inner}^{(old)} = 3.98 \cdot 10^{-16} \text{ dyn cm}^{-2} & \Rightarrow p_{w,inner}^{(new)} = 4.00 \cdot 10^{-17} \text{ dyn cm}^{-2} \end{cases} . \quad (4.3.1)$$

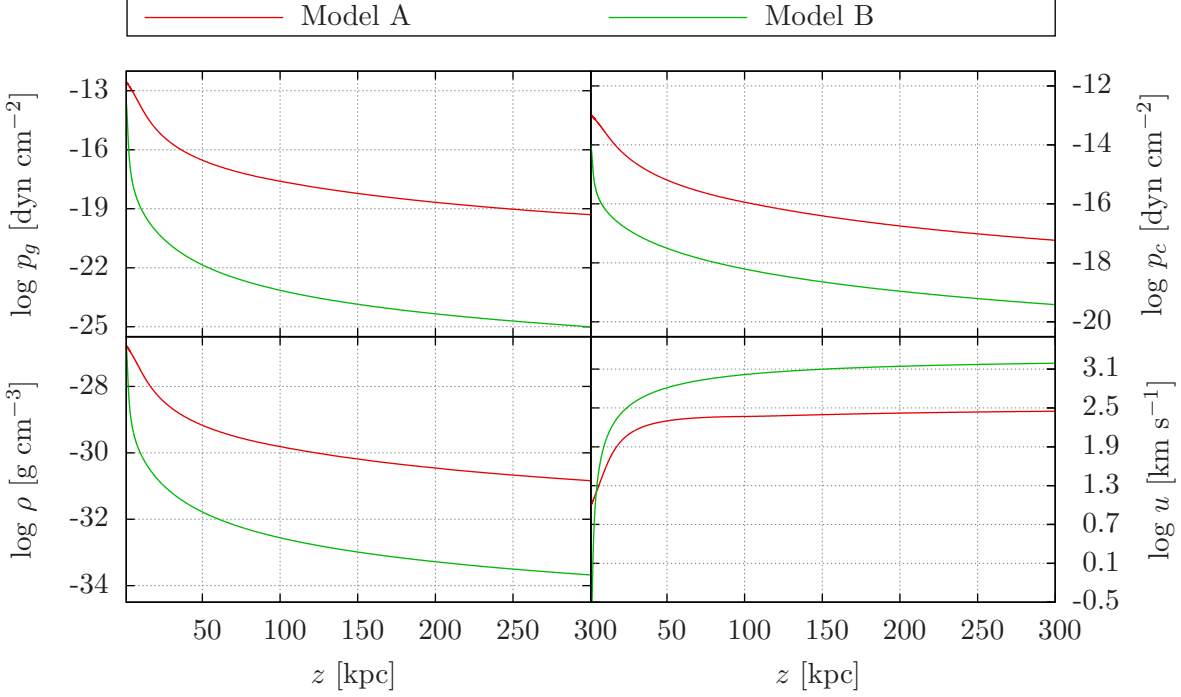


Figure 4.4: Variations of ρ , u , p_g and p_c with distance z from the galactic plane (old profiles black, new profiles red), if the pressures are adopted like in (4.3.1). Note that the velocity u at the inner boundary drops significantly.

In Figure 4.4 one can see that in the inner region ($0 - 20$ kpc) the velocity is very low, which results in a very low mass flow. Consequently few material is advected along the fluxtube, which results in steeply falling pressure gradients. The following initial parameters are used in later time-dependent calculations as initial model and are denoted as **Model B**:

$$\left\{ \begin{array}{ll} p_{g,inner} & = 2.76 \cdot 10^{-14} \text{ dyn cm}^{-2} \quad (\text{initial gas pressure } p_g \text{ at inner boundary}), \\ p_{c,inner} & = 1.00 \cdot 10^{-14} \text{ dyn cm}^{-2} \quad (\text{initial CR pressure } p_c \text{ at inner boundary}), \\ p_{w,inner} & = 4.00 \cdot 10^{-17} \text{ dyn cm}^{-2} \quad (\text{initial wave pressure } p_g \text{ at inner boundary}), \\ \rho_{inner} & = 1.67 \cdot 10^{-27} \text{ g cm}^{-3} \quad (\text{initial density } \rho \text{ at inner boundary}), \\ u_{inner} & = 0.28 \text{ km s}^{-1} \quad (\text{initial gas velocity } u \text{ at inner boundary}). \end{array} \right. \quad (4.3.2)$$

Taking the momentum equation (2.4.1) for a stationary wind $\left(\frac{\partial}{\partial t} = 0\right)$ and identifying

F with the gravitational force (see section 2.9), one arrives at the following expression,

$$\nabla [\rho \mathbf{u} \otimes \mathbf{u} + p \cdot \mathbf{I}] = -\rho \nabla \phi \quad (4.3.3)$$

In the hydrostatic case $u = 0$ (in 1D fluxtube geometry) this would simplify to a well known equation,

$$\frac{dp}{dz} = -\rho \frac{d\phi}{dz} \quad (4.3.4)$$

Obviously, the velocity terms are modifying the pressure profile and the density profile. The reason of creating a initial configuration like **Model B** is, that the wind should feel no wind structure very close to the superbubble. Therefore the relative deviation of the pressure gradients (at the inner boundary) with respect to the hydrostatic case are shown below in Table 4.1.

		Model A	Model B
scaleheight h_z [kpc]		5.86	1.50
$dp(z = 1\text{kpc})/dz$	[dyn cm ⁻³]	$-2.084 \cdot 10^{-35}$	$-2.074 \cdot 10^{-35}$
$-\rho d\phi(z = 1\text{kpc})/dz$	[dyn cm ⁻³]	$-2.078 \cdot 10^{-35}$	$-2.060 \cdot 10^{-35}$
relative deviation		0.003	0.006
$dp(z = h_z)/dz$	[dyn cm ⁻³]	$-9.676 \cdot 10^{-36}$	$-9.549 \cdot 10^{-36}$
$-\rho d\phi(z = h_z)/dz$	[dyn cm ⁻³]	$-7.915 \cdot 10^{-36}$	$-8.042 \cdot 10^{-36}$
relative deviation		0.22	0.19

Table 4.1: Comparison of thermal and kinetic energy at the inner boundary for **Model B**.

Because virtually no mass is transported in the case of **Model B**, the gas pressure is not the important contribution to the overall pressure, in fact the gas is accelerated very quickly up to very high velocities (always having in mind, that the wind is fast but extremely light). This is the reason, why the approximation of having a hydrostatic initial model only can be applied very close to the inner boundary (which was the intention). For **Model B**, the model keeps slightly more accurate at the point of h_z , this is because the velocities are initially lower and therefore the hydrostatic approximation is better obeyed. Hence **Model B** is sometimes referred to as *quasi-hydrostatic* initial model (at least close to the inner boundary).

5 Results

In this section the results are presented, which are obtained with the numerical method described in section 3. The dependence of the solutions on the diffusion coefficient κ will be discussed as well as the effect of different time-dependent inner boundary conditions (especially boundary conditions with and without feedback of the wind, see section 3.4.1). A point of particular interest is the evolution of the shock-fronts, which are very likely to occur when multiple supernovae are providing the initial energies to drive a galactic wind (see section 1.3 for details), since these shock-fronts are assumed to re-accelerate CRs due to the First-Order Fermi mechanism (section 1.2.3 for details, see also Dorfi & Breitschwerdt (2012)) and hence are pushing the wind further outwards.

5.1 Flow structure

5.1.1 Flow features

The major purpose of the galactic-wind simulations in this thesis is the investigation of flow features caused by variation of the inner boundaries. Using the Kompaneets approximation described in 1.3 and 3.4.1, a supernova explosion leads to an *immediate increase* in the gas pressure p_g and the cosmic ray pressure p_c . This increases the *sound speed* c_s , which can be calculated (for an ideal gas) in the following well known way,

$$c_s := \sqrt{\gamma_g \frac{p_g}{\rho}}. \quad (5.1.1)$$

Thus a perturbation propagating at sound speed is steepening while moving through the flow, because the perturbation propagates faster for a higher pressure p_g (see Figure 5.1 for a schematic view of this process). The resulting perturbations are then propagating as *shock waves* along the fluxtube and heating up the medium. In addition to these so-called *forward shocks* it can be shown, that also a shock-wave arises, which travels inward

in direction of the shocked medium, a so-called *reverse shock* (see e.g. in Lozinskaia & Lozinskaia (1992) or also in Dorfi & Breitschwerdt (2012)).

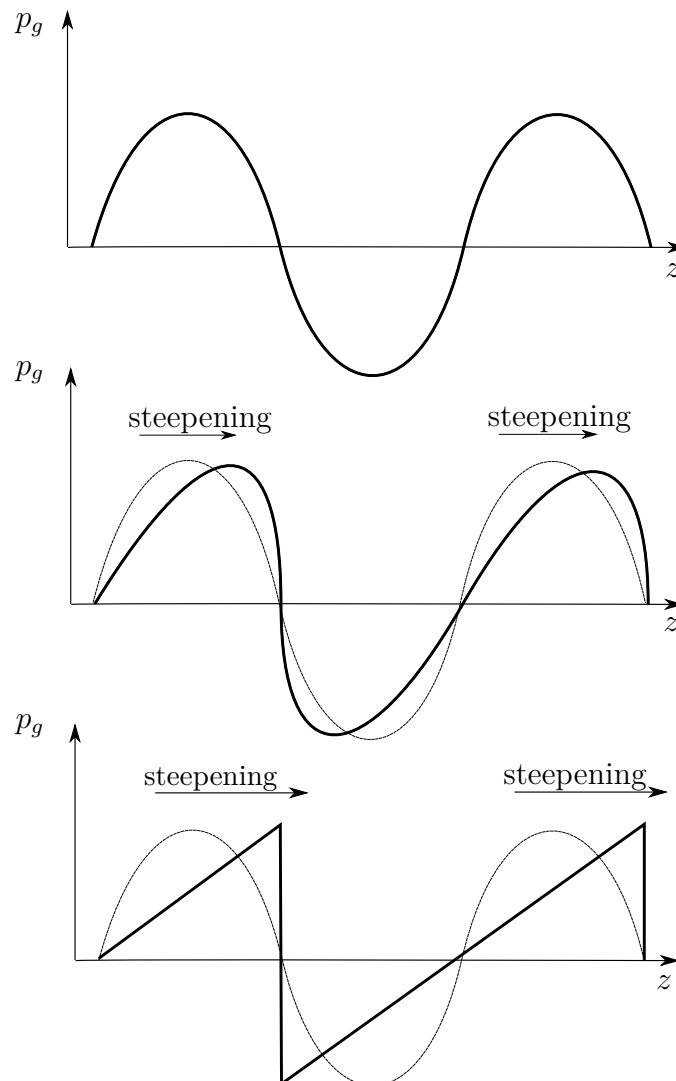


Figure 5.1: Schematic view of building up a shock wave. In the upper panel an ordinary acoustic perturbation is propagating with sound speed c_s into the medium. Due to the higher pressure at the peaks the perturbation is propagating faster there. This leads to a steepening and a supersonic propagation of the disturbance (shock).

In the case of a sequence of supernova explosions, several shock fronts will build up at the inner boundary and then propagate with supersonic speed $u_{S,1}$ with respect to the upstream region (in the shock frame), in other words the Mach-number of the shock $M_1 > 1$, and has subsonic speed $u_{S,2}$ in the downstream region, consequently $M_2 < 1$. Therefore each forward shock will catch up with the shock in front of it, until they are merging.

The galactic wind structure has been calculated for the two initial models **Model A** and **Model B** with the parameter sets (4.1.12) and (4.1.12), respectively. In the following shown example, two different plot regions will be distinguished, namely the *inner region* and the *outer region* of the galactic wind. In the inner region (from 1.0–1.6 kpc) the different subsequent shock waves can be seen and its representation in the various gas and density profiles as well as in the wind velocity profile. When the shock propagates, the shock waves will merge to a *single strong shock wave* propagating through the medium and accelerating the out-streaming gas. Furthermore the geometrical expansion due to the fluxtube geometry will smear the flow structures, therefore it makes sense to also observe the large-scale behaviour (from 1.0 – 300 kpc) of the galactic wind.

In this section *no mass loss* is considered, especially $E_{g,loss} = E_{c,loss} = \rho_{loss} = 0$ (see section 3.4.1 for details).

The plots for the inner region have been performed by using $N = 2000$ grid points for a better resolution and lower dissipation of the shocks. Due to numerical difficulties (see section 6.1) it has not been able to achieve acceptable timesteps for the calculations of the outer region. Hence these simulations have been performed for $N = 1000$ grid points, which is sufficient for getting the overall structure of the galactic wind.

Parameters for the results shown in this section with a diffusion coefficient of $\kappa = 10^{29}$ $\text{cm}^2 \text{s}^{-1}$ are given in the table 5.1 (the g_i are *weights* assigned to one of the variables $i = \{\rho, u, p_g, p_c, p_w, z\}$, see section 3.1).

	N	l_q	τ	q_1	q_2	g_ρ	g_u	g_{p_g}	g_{p_c}	g_{p_w}	g_z
Model A (inner region)	2000	z	$1.0 \cdot 10^8$	0	10^{-3}	1	0	1	1	0.1	0
Model B (inner region)	2000	z	$1.0 \cdot 10^8$	0	10^{-3}	1	0	1	1	0.1	0
Model A (outer region)	1000	z	$1.0 \cdot 10^6$	0	10^{-3}	1	0	1	0	0	0
Model B (outer region)	1000	z	$1.0 \cdot 10^8$	0	10^{-3}	1	0	0.1	1	1	0

Table 5.1: Numerical parameters (described in section 3.1 and section 3.2) used for the simulations of the galactic wind for $\kappa = 10^{29} \text{ cm}^2 \text{ s}^{-1}$ and no mass loss.

Then the inner boundaries are varied according to the Kompaneets approximation (see section 1.3), and the results are presented in the subsequent plots 5.2 and 5.3, comparing

the results for the two different starting models **Model A** and **Model B**.

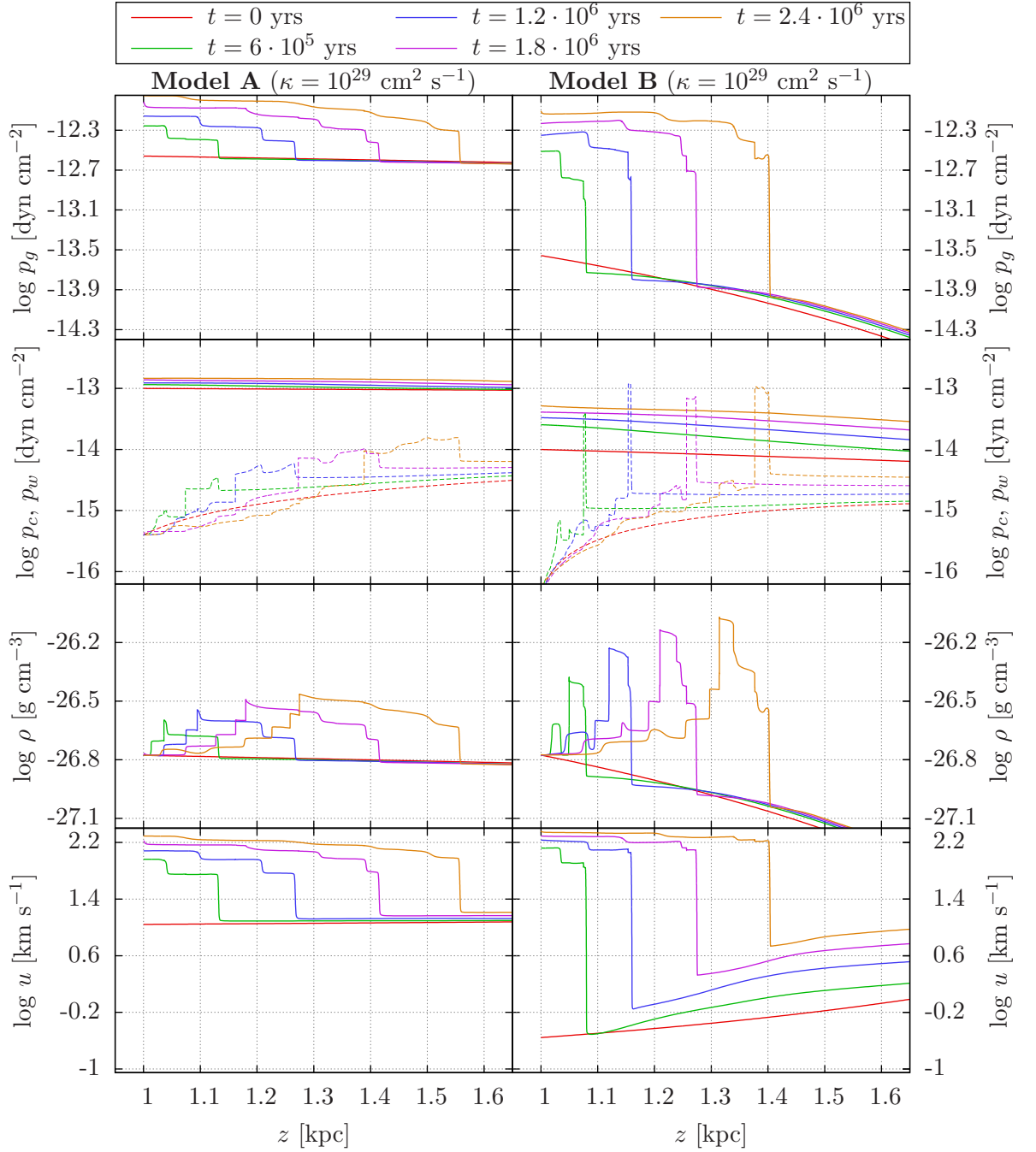


Figure 5.2: Various pressure profiles p_g , p_c and p_w as well as the density profile ρ and the gas velocity profile u at five different times (see legend) for the two different models **Model A** and **Model B**. The CR pressure profile and the wave pressure profiles (dashed lines) are shown in the same plot, because of their interaction with each other (see section 1.2).

Various interesting things can be seen in these plots, first of all the quite dominant forward shocks. This features can be seen in every profile plotted in figure 5.2. The shock waves result (as already explained above in this section) from a sudden increase in gas pressure and CR pressure at the inner boundary. The major difference between the two models is the typical time inbetween two shock waves merge. This can be seen e.g. in the gas pressure profile, where the shock fronts are clearly still separated in **Model A**, but not so in **Model B**, which reveals a stronger merged shock already.

The density profiles in Figure 5.2 reveal both forward shocks and reverse shocks, which is expected in the presence of strong shocks, since then the gas is compressed. The forward shocks are propagating outwards along the fluxtube, therefore the density on the LHS of the forward shocks is higher (downstream in the system of the shock). On the other hand the reverse shocks tend to run inwards (but are effectively convected outwards), consequently the gas is compressed on the RHS of the reverse shocks. Note that in the density profiles in **Model B** the forward and reverse shock velocities do not differ as much as they do in **Model A**. This can be verified by comparing the position of the forward and reverse shocks in Figure 5.2 (in **Model A** the distance between the two shock fronts is larger than it is in **Model B**). The gas pressure p_g at the inner boundary for **Model B** is considerably lower than in **Model A** (compare 4.1.12 and 4.3.2), therefore the speed of sound c_s defined in (5.1.1) is also lower, which leads to lower shock velocities in **Model B** (compare with Figure 5.2) with the assumption of equally strong shocks in **Model A** and **Model B**. Consequently the forward and reverse shocks do propagate slower through the medium and hence are not able to get as much distance between them as they would do with higher velocities.

The wave pressure profiles in Figure 5.2) show best how the first-order Fermi mechanism works. It has been already pointed out in Dorfi & Breitschwerdt (2012), that in the vicinity of shock waves particle acceleration due to the first-order Fermi mechanism is very effective. These particles themselves resonantly excite waves, which increase the wave pressure p_w . The process can be seen very clearly in the above figure, at least for the forward shocks. The reverse shocks are at this early propagation time still quite weak but will build up, as they proceed down the density gradients of the halo gas. As soon as the reverse shocks have built up to strong shocks, the same particle acceleration and wave excitation processes occur for forward and reverse shocks. This is also a justification of taking a closer look at the wind structure for later times, which is done

in the next plot, Figure 5.3.

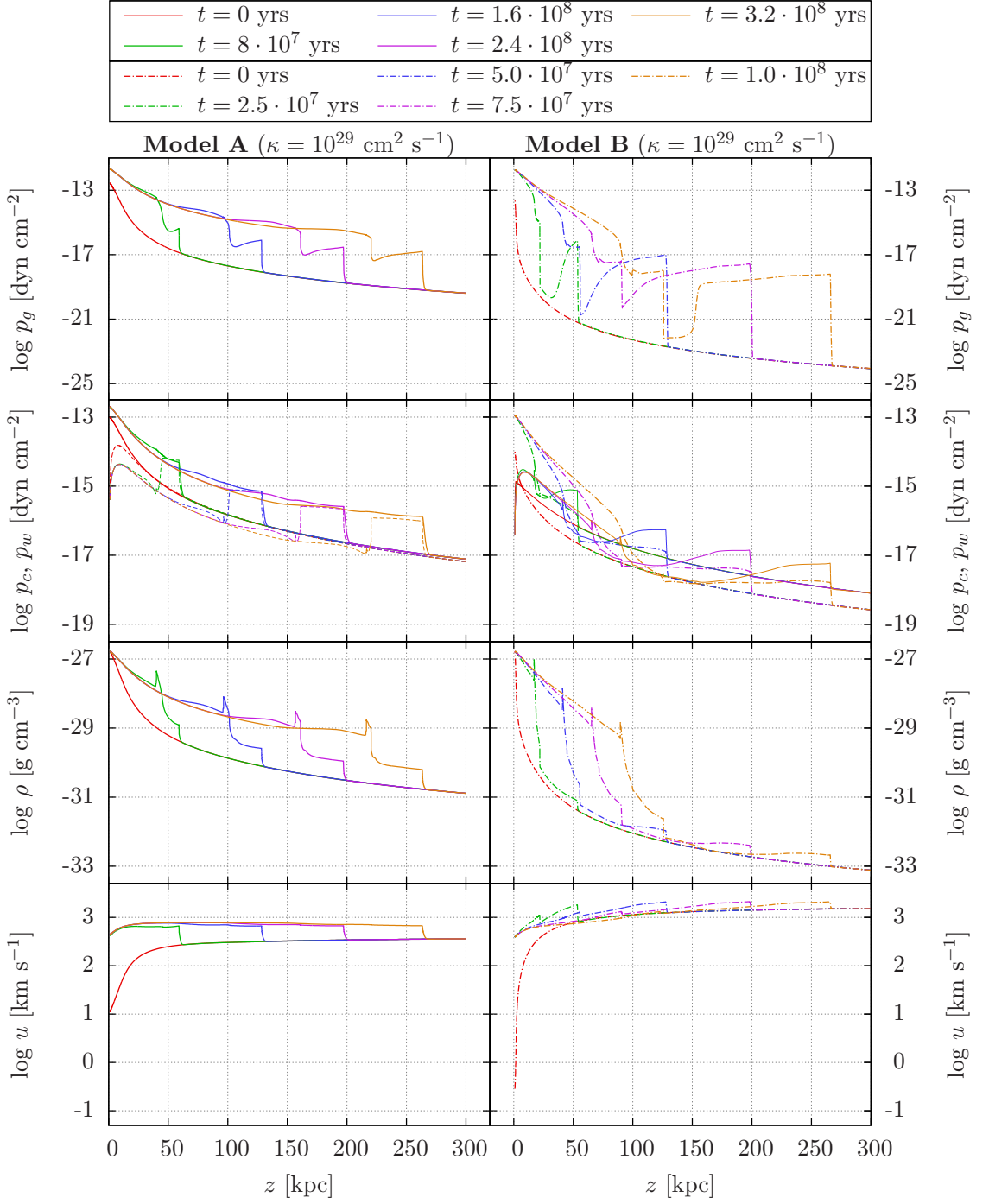


Figure 5.3: Various pressure profiles p_g , p_c and p_w as well as the density profile ρ and the gas velocity profile u at five different times (see legend) for the two different models **Model A** and **Model B**. The CR pressure profile and the wave pressure profiles (dashed line for **Model A**, full line for **Model B**) are again shown in the same plot.

The steepening of the forward shock can be seen best in the gas pressure profiles of Figure 5.3. The shock propagates at higher speed through the medium, which is straightforward to understand, since due to the hydrostatic initial model (**Model B**) there are much steeper density and pressure gradients. This can be seen by looking at the different times for the models which are plotted in Figure 5.3, e.g. the forward shocks in the rightmost curve (orange) are nearly at the same position above the galactic mid-plane (approximately $z = 265$ pc), although the shock in **Model A** needed $3.2 \cdot 10^8$ years and the shock in **Model B** only needed $1.0 \cdot 10^8$ years.

The position of the reverse shock is best visible in the density profile, where one can even see (at least in **Model B**), that the reverse shock is propagating backwards (with respect to the contact discontinuity). The contact discontinuity can be identified as the second very steep increase (shock-like structure) in the density profile, e.g. in the rightmost (orange) curve at approximately $z = 125$ pc. It is also remarkable that the shock velocities for **Model B** in Figure 5.3 seem to differ much more for forward and reverse shock, than it can be expected from Figure 5.2. This can be explained once more by taking the strong density gradients into account, which are present for **Model B** and will let the shocks speed up and get stronger which leads straightforward to more different shock propagation velocities.

The cosmic ray pressure profile only shows the presence of the forward shock, but no clear evidence of the reverse shock. This is simply due to the fact, that the diffusion coefficient is chosen sufficiently high to smear this feature in this plot, which is the case for both initial models. In the wave pressure profile the position of both shock fronts can be determined. In **Model A** as well as in **Model B** somewhat spiky features can be seen on the left of the forward shock structure, e.g. in **Model A** at approximately at $z = 220$ kpc in the rightmost (orange) curve. This quite weak feature (compared to the forward shock) nevertheless shows, that also the reverse shock is a site of resonant wave excitation caused by particle acceleration.

The velocity profiles show in both models the same structure, although the features are stronger and therefore better to see in **Model B**. As already shown in Dorfi & Breitschwerdt (2012), the velocity profile points out the importance of a forward shock to drive a galactic wind. The velocity increases at the inner boundary in **Model A** over more than one order of magnitude, in **Model B** even more than two orders of

magnitude. The velocity profile in **Model B** also justifies the assumption of speaking about a quasi-hydrostatic initial model. As one can see, the innermost curve (red dot-dashed line) reveals that the wind transports virtually no material outside because of the very low initial velocity, hence one can say that the halo gas is approximately at rest.

5.2 Dependence on the diffusion coefficient

In this section the flow features discussed in section 5.1.1 are compared to those obtained when different diffusion coefficients κ are chosen. In general varying the diffusion coefficient has the following effect on the overall structure of the galactic wind:

- If the diffusion coefficient κ is increased, more CRs can escape from the confinement to the Alfvén waves (see section 1.2.2). If purely advective winds were considered ($\kappa = 0 \text{ cm}^2 \text{ s}^{-1}$), then the topology of the wind structure would be determined such that the wind *must* flow through the critical point (for details see Breitschwerdt et al. (1991); Dorfi & Breitschwerdt (2012)), whereas in the case of diffusion this condition is not so strong anymore and the wind topology is slightly modified (compare with Figure 5.4).

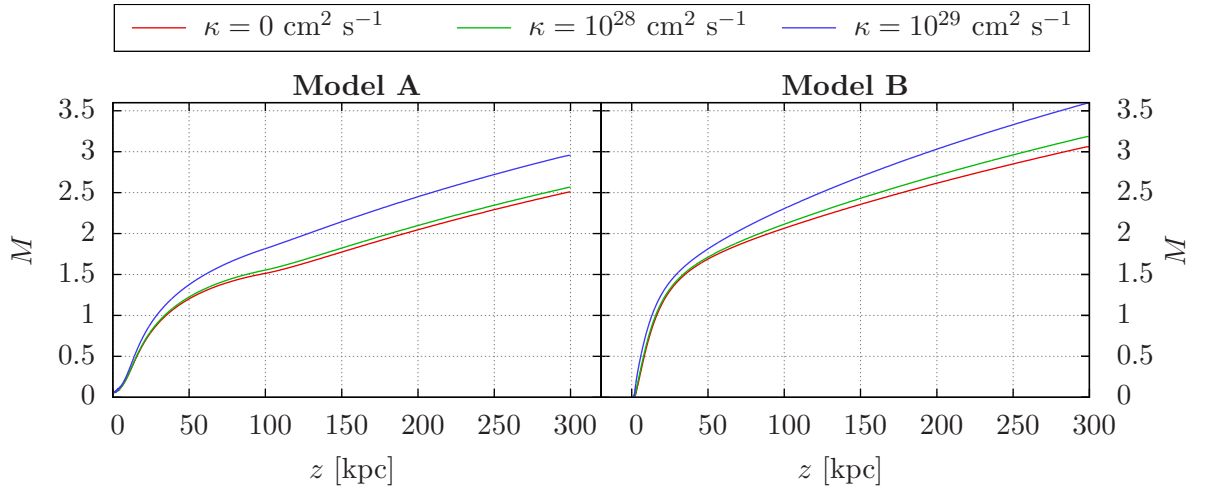


Figure 5.4: The flow topology (Machnumber - distance plot) for **Model A** and **Model B** and for three different diffusion coefficients.

The dependence on steady-state galactic wind solutions on the diffusion coefficient κ has already been subject of interest in Dorfi & Breitschwerdt (2012) and is shown and

discussed there in more detail. In this thesis it will be discussed how the time-dependent flow features like shocks are modified by different values of κ . Therefore the simulations shown in Figures 5.2 and 5.3 are repeated with two different values of κ , namely $\kappa_1 = 0 \text{ cm}^2 \text{ s}^{-1}$ (Figures 5.7 and 5.8) and $\kappa_2 = 10^{28} \text{ cm}^2 \text{ s}^{-1}$ (Figures 5.5 and 5.6).

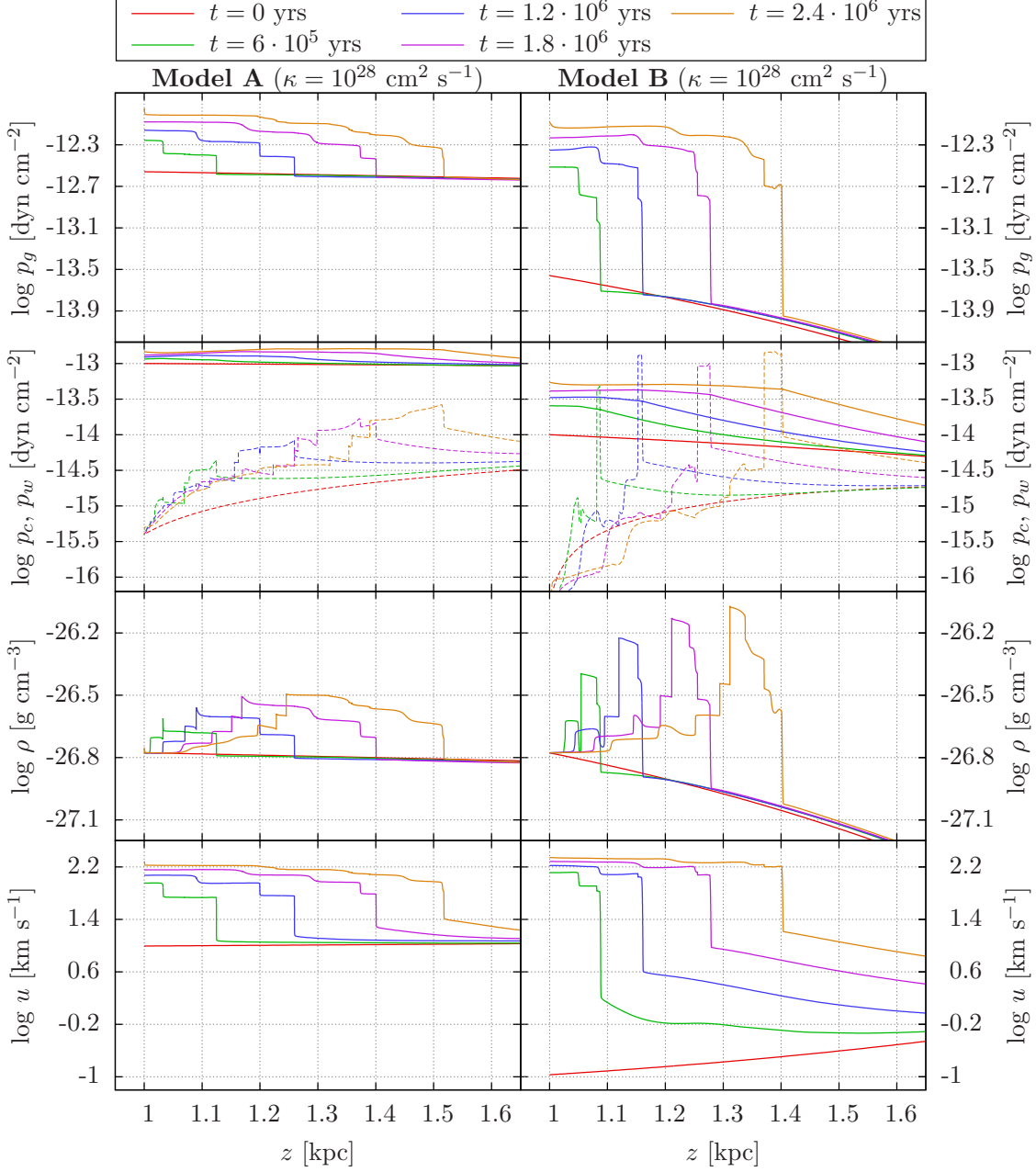


Figure 5.5: Various pressure profiles p_g , p_c and p_w as well as the density profile ρ and the gas velocity profile u at five different times (see legend) for the two different models **Model A** and **Model B**. The forward shock can be also seen in the CR pressure profile (a knee).

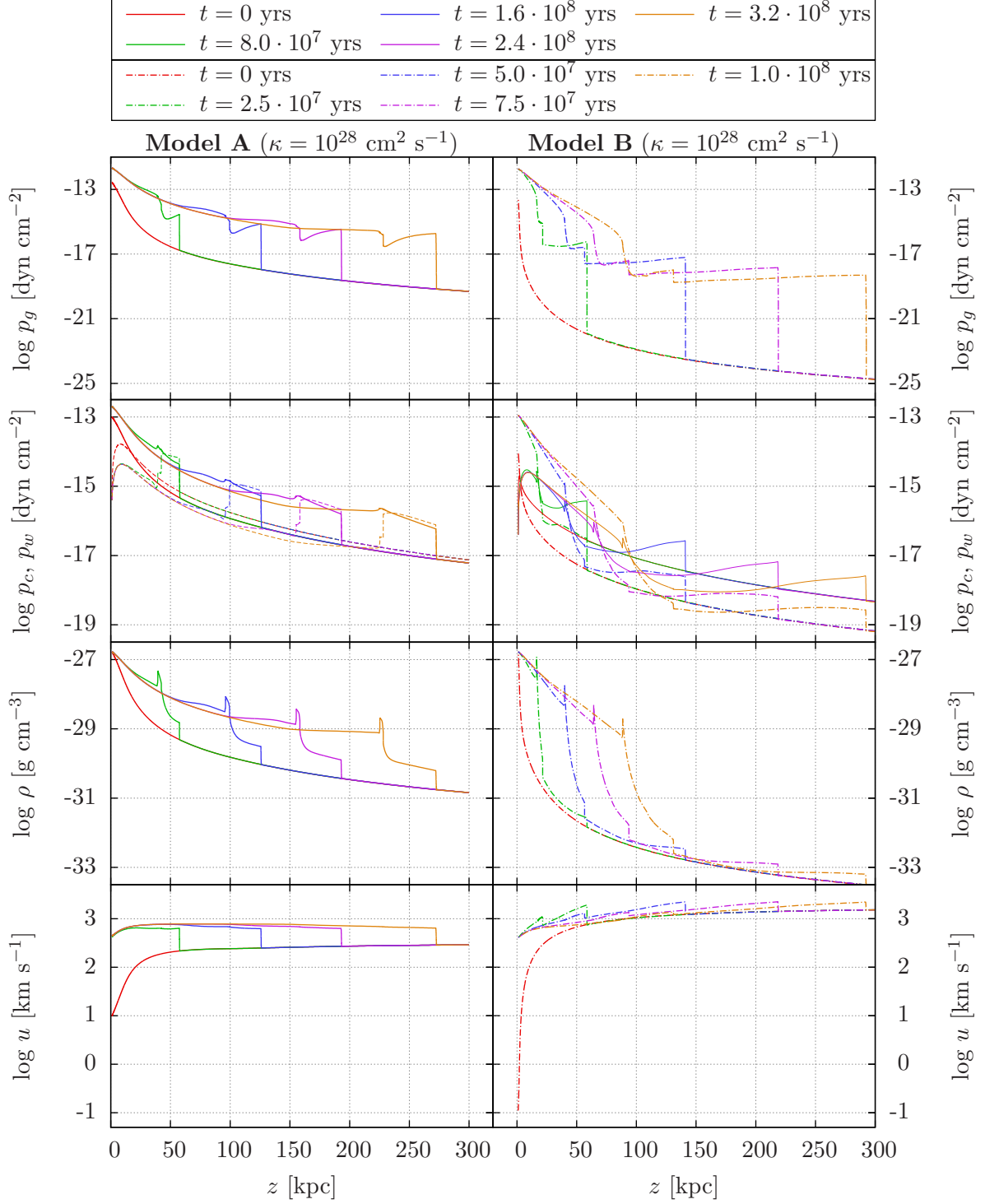


Figure 5.6: Various pressure profiles p_g , p_c and p_w as well as the density profile ρ and the gas velocity profile u at five different times (see legend) for the two different models **Model A** and **Model B**. The reverse shock becomes visible in the CR pressure profile of both models (e.g. in the rightmost orange curve for **Model A** at approximately 225 kpc).

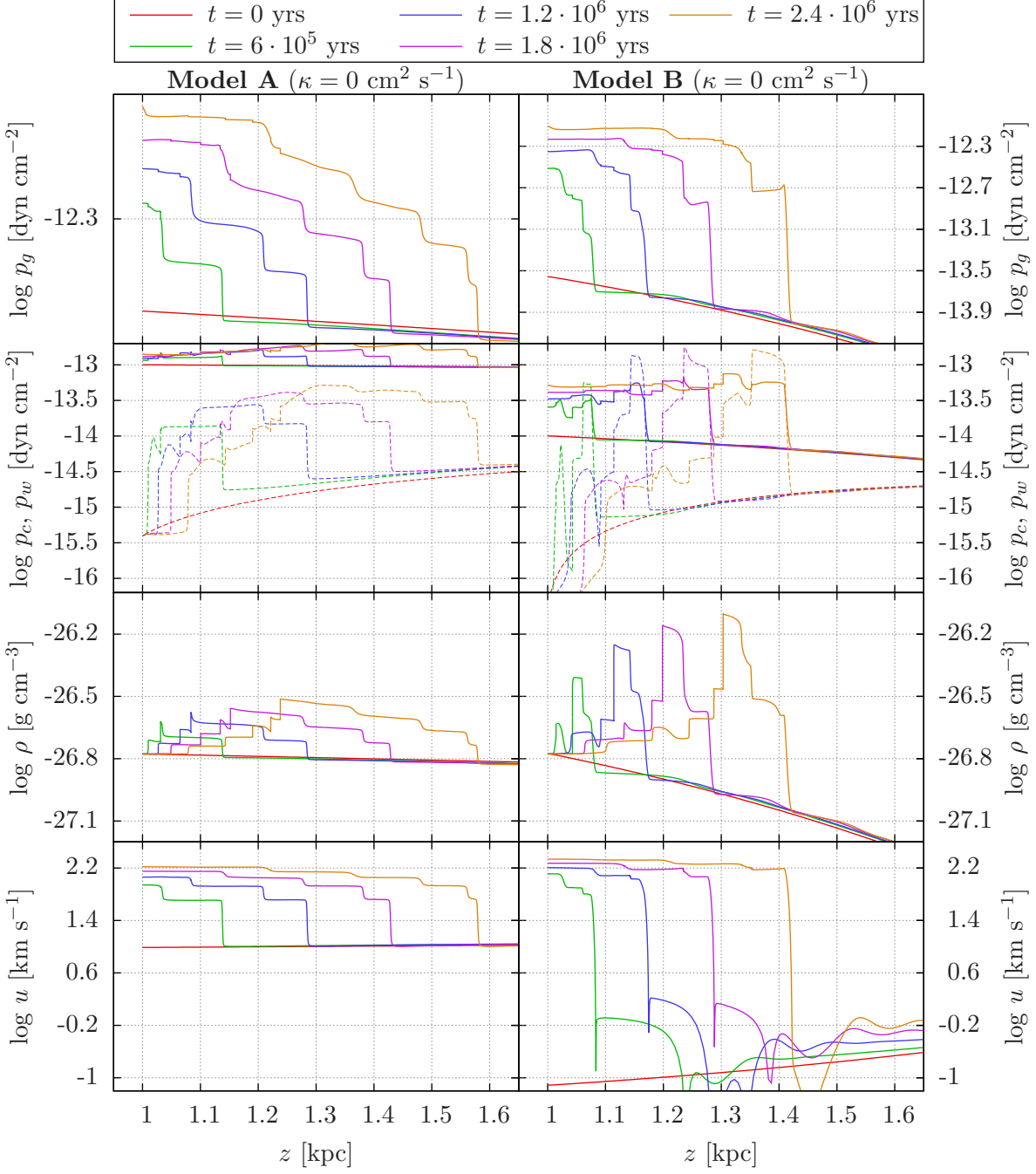


Figure 5.7: Various pressure profiles p_g , p_c and p_w as well as the density profile ρ and the gas velocity profile u at five different times (see legend) for the two different models **Model A** and **Model B**. The CR pressure profile and the wave pressure profiles (dashed lines) are again shown in the same plot.

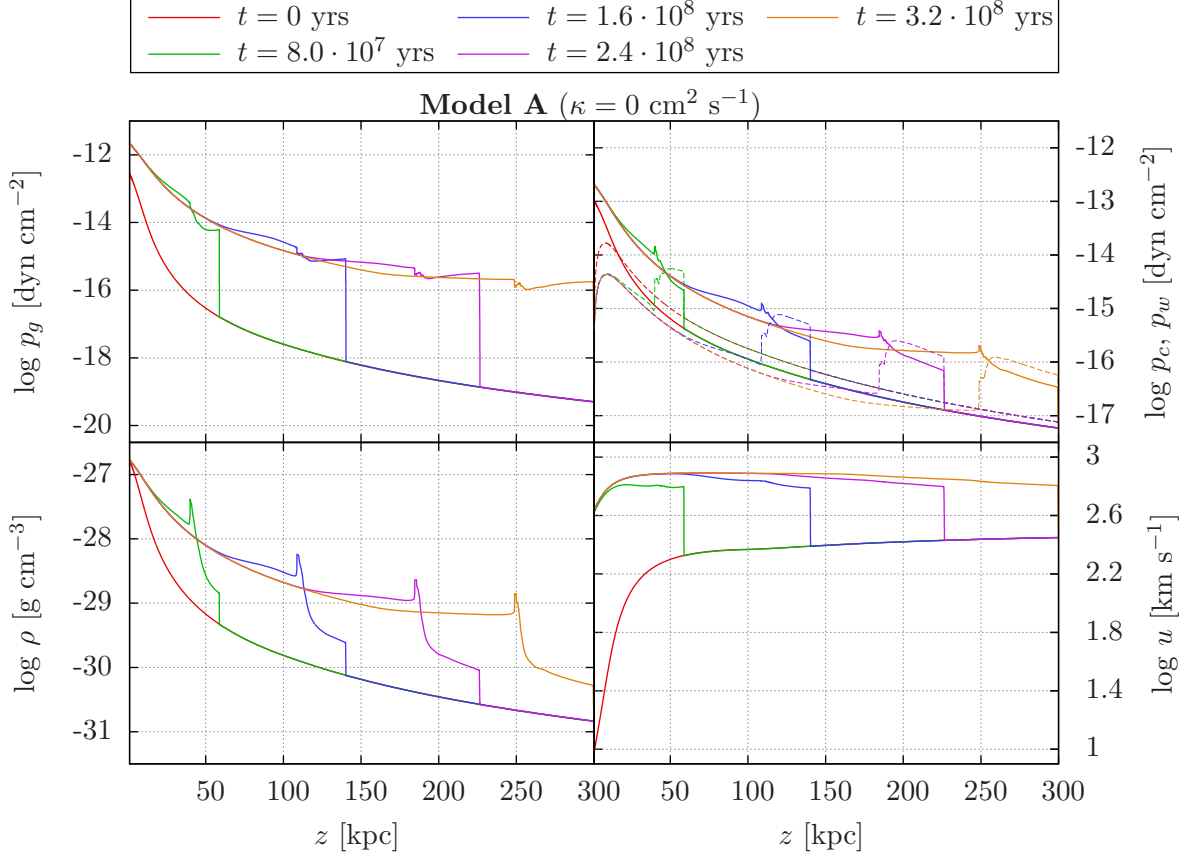


Figure 5.8: Various pressure profiles p_g , p_c and p_w as well as the density profile ρ and the gas velocity profile u at five different times (see legend) for **Model A**. The CR pressure profile and the wave pressure profile (dashed line) reveal a structure which is not flat anymore (compared to Figure 5.3).

The parameters which are used to produce the results shown in the Figures 5.5 - 5.7 are given in Tables 5.2 and 5.3.

	N	l_q	τ	q_1	q_2	g_ρ	g_u	g_{p_g}	g_{p_c}	g_{p_w}	g_z
Model A (inner region)	2000	z	$1.0 \cdot 10^7$	0	10^{-4}	1	0	1.1	1	0.4	0
Model B (inner region)	2000	z	$1.0 \cdot 10^8$	0	10^{-3}	1	0	1	1	0.01	0
Model A (outer region)	1000	z	$1.0 \cdot 10^6$	0	10^{-3}	1	0	1	0	0	0
Model B (outer region)	1000	z	$1.0 \cdot 10^8$	0	10^{-3}	1	0	1	1	0.01	0

Table 5.2: Numerical parameters used for the simulations of the galactic wind for $\kappa = 10^{28} \text{ cm}^2 \text{ s}^{-1}$ and no mass loss.

	N	l_q	τ	q_1	q_2	g_ρ	g_u	g_{p_g}	g_{p_c}	g_{p_w}	g_z
Model A (inner region)	2000	z	$1.0 \cdot 10^7$	0	10^{-3}	1	0	1	0.1	0	0
Model B (inner region)	2000	z	$1.0 \cdot 10^8$	0	10^{-3}	1	0	1	0.1	0.1	0
Model A (outer region)	1000	z	$1.0 \cdot 10^6$	0	10^{-3}	1	0	1.1	0.7	0.01	0

Table 5.3: Numerical parameters used for the simulations of the galactic wind for $\kappa = 0 \text{ cm}^2 \text{ s}^{-1}$ and no mass loss.

Note that the outer region plot for **Model B** and a diffusion coefficient $\kappa = 0 \text{ cm}^2 \text{ s}^{-1}$ is missing. That is because of numerical difficulties which have occurred while trying to run a simulation for these initial conditions and parameters (see also section 6.1).

In the case of diffusion, the so-called *characteristic diffusion length scale* L is of particular interest when investigating the effects of diffusion in galactic winds. This scale is a measure for the range in which diffusion can influence the galactic flow. L is proportional to the main free path of CR particles l_{CR} (see equation (3.2.3), hence

$$L \propto l_{CR} = \frac{\kappa}{u_s} . \quad (5.2.1)$$

Taking characteristic values for the flow velocity u for the inner 10 kpc ($u_{char} \approx 400 \text{ km s}^{-1}$ for **Model A** and **Model B**, compare with Figures 5.3 and 5.6), one obtains the following characteristic diffusion lengths L ,

$$L \approx 0.8 \text{ kpc} \quad (\text{for } \kappa = 10^{29} \text{ cm}^2 \text{ s}^{-1}) , \quad (5.2.2)$$

$$L \approx 0.08 \text{ kpc} \quad (\text{for } \kappa = 10^{28} \text{ cm}^2 \text{ s}^{-1}) . \quad (5.2.3)$$

Hence, all flow features smaller than this L will be smeared in the CR pressure profile and are not visible in the plots. Therefore it is not surprising, that in the inner region plot for $\kappa = 10^{29} \text{ cm}^2 \text{ s}^{-1}$ (see Figure 5.2) no structures are noticeable. Although still not immediately to see, the forward shock structure can be seen in the CR pressure profile for $\kappa = 10^{28} \text{ cm}^2 \text{ s}^{-1}$ in Figure 5.5 (a knee at the site of the forward shock).

Differences can also be seen in the plots of the CR pressure for the outer region (compare Figure 5.3 and Figure 5.6). The reverse shock becomes visible for $\kappa = 10^{28} \text{ cm}^2 \text{ s}^{-1}$, which is due to the same arguments as before: The reverse shock structure is of the order of approximately 1 kpc, as well as the diffusion length L , consequently this feature

is strongly influenced by diffusion, more precisely the diffusion will cause a smearing of the reverse shock.

Clearly, in the case of no diffusion ($\kappa = 0 \text{ cm}^2 \text{ s}^{-1}$), only advection is responsible for the flow features. Consequently, no features are smeared in the CR pressure profile and every single shock front caused by the sequential explosion of supernovae can be distinguished and identified (see Figure 5.7). Another remarkable flow feature can be seen in the velocity profile for **Model B** and no diffusion in Figure 5.7. The structures which can be seen in this plot are probably *physical instabilities* caused by the different propagation speeds from gas component compared to waves and CRs (see section 1.2 for details).

5.2.1 Time evolution of shock fronts

Another important question is the investigation of the time evolution of the propagating shock fronts for being able to derive a *typical merging timescale* τ_{merge} as well as a *typical merging scaleheight* z_{merge} . This is important in the context of particle acceleration due to the first-order Fermi mechanism, if the shocks merge in short times and distances to form very strong shocks with high compression ratios and in this way ensure ongoing particle acceleration.

In this section the time evolution of the shock fronts and its dependence on the two different initial models (**Model A** and **Model B**) is discussed. Furthermore the dependence on the diffusion coefficient κ is discussed and values for τ_{merge} and z_{merge} are derived. In Figure 5.9 the time evolution of the first five shocks is shown for the two initial models and for three different diffusion coefficients κ . The time axis is normalized to the time interval between two supernova explosions $dt = 4.8 \cdot 10^5$ years (see section 1.3, especially parameter set 1.3.22)).

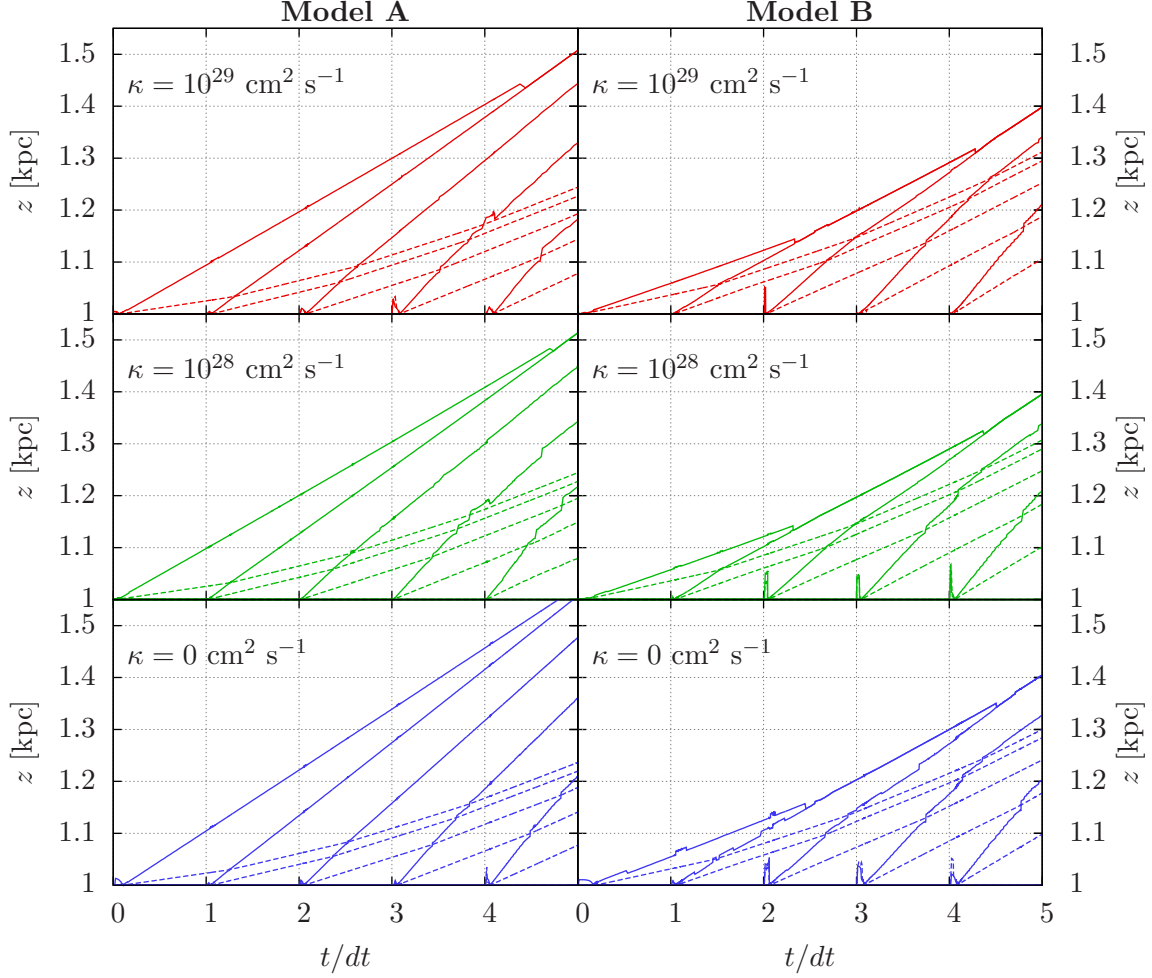


Figure 5.9: The timeevolution (distance z plotted against time t/dt , where dt is the time interval between two supernova explosions) for the first five shocks is shown here. One can see, that the shocks will converge after a certain time and practically merge to one single shock-front. The full lines correspond to the forward shocks created by each supernova explosion, the dashed lines are showing the time evolution of the reverse shocks.

The non-smooth variations in the time evolution tracks of the shock fronts occur, because the program which logs the shock fronts, can temporarily lose track of the shocks, especially when a forward shock passes a reverse shock (see for example in the upper left plot for the fourth forward shock at $t/dt \approx 4$).

The first thing which can be seen immediately is that the forward shock fronts will *merge* to one single strong shock front, which is the expected result and has been already discussed in the beginning of section 5.1.1. Note that for **Model A** the first two forward

shocks merge for all diffusion coefficients discussed in this thesis at least below a height of $z \approx 1.6$ kpc, which is very close to the inner boundary. For **Model B**, the shocks will merge even faster, namely below the height $z \approx 1.2$ kpc. The reason for the lower merging scaleheight z_{merge} in **Model B** comes from the fact, that the shocks run into a highly rarefied medium (even compared to initial **Model A**) with a strong density gradient which causes a further steepening of the shocks. The shock velocities u_S can be used to determine the Mach number and give information on how strong the shock is. If the assumption of an ideal gas is made (as it is in this case, see section 1.2 for further details), then there is another way of determining the shock Mach number. Elementary thermodynamics and the assumption of an ideal gas lead to the following expression (see e.g. Longair (2011), p. 317 for further details),

$$\frac{p_2}{p_1} = \frac{2\gamma M_1^2 - (\gamma - 1)}{(\gamma + 1)}. \quad (5.2.4)$$

This can be reordered to obtain an expression for M_1 dependent on the pressure ratio $\frac{p_2}{p_1}$,

$$M_1 = \sqrt{\frac{p_2}{p_1} \frac{\gamma + 1}{2\gamma} + \frac{\gamma - 1}{2\gamma}}, \quad (5.2.5)$$

where p_1 and p_2 are the gas pressure before and after the shock, respectively, and M_1 denotes the Mach number of the shock front with respect to the gas upstream and $\gamma = \frac{5}{3}$ is the adiabatic index of the medium. The pressure ratios as well as the corresponding shock Mach numbers (the first five shocks for **Model A** and **B**) are listed in Table 5.4, if the gas pressure is increased at every time interval dt according to the quantities derived for the Kompaneets approximation in section 1.3.

In Table 5.4 one can see by looking at the Mach numbers, that apart from the first shock for **Model B** the shocks are not strong shocks close to the inner boundary. This is the reason why only the first five shock fronts are considered here; the subsequent shocks are already very weak and are therefore of minor physical relevance. Apart from that, it is difficult to track such weak shocks, because these features underlie a numerical dissipation and are going to vanish after a certain simulation time.

A cosmic ray driven galactic wind needs high energy CRs for being able to propagate into the halo, therefore it is necessary to have strong shocks which accelerate the par-

		Model A	Model B
1. shock	$p_1^{(1)}$ [dyn cm ⁻²]	$2.76 \cdot 10^{-13}$	$2.76 \cdot 10^{-14}$
	$p_2^{(1)} = p_1^{(2)}$ [dyn cm ⁻²]	$4.15 \cdot 10^{-13}$	$1.67 \cdot 10^{-13}$
	$p_1^{(1)}/p_2^{(1)}$	1.50	6.05
	$M_1^{(1)}$	1.18	2.24
2. shock	$p_2^{(2)} = p_1^{(3)}$ [dyn cm ⁻²]	$5.55 \cdot 10^{-13}$	$3.06 \cdot 10^{-13}$
	$p_2^{(2)}/p_1^{(2)}$	1.33	1.83
	$M_1^{(2)}$	1.13	1.29
3. shock	$p_2^{(3)} = p_1^{(4)}$ [dyn cm ⁻²]	$6.94 \cdot 10^{-13}$	$4.46 \cdot 10^{-13}$
	$p_2^{(3)}/p_1^{(3)}$	1.25	1.46
	$M_1^{(3)}$	1.09	1.17
4. shock	$p_2^{(4)} = p_1^{(5)}$ [dyn cm ⁻²]	$8.33 \cdot 10^{-13}$	$5.85 \cdot 10^{-13}$
	$p_2^{(4)}/p_1^{(4)}$	1.20	1.31
	$M_1^{(4)}$	1.08	1.12
5. shock	$p_2^{(5)}$ [dyn cm ⁻²]	$9.73 \cdot 10^{-13}$	$7.24 \cdot 10^{-13}$
	$p_2^{(5)}/p_1^{(5)}$	1.17	1.23
	$M_1^{(5)}$	1.06	1.09

Table 5.4: Pressure ratio and Mach number of the shock fronts for the two initial models for the first five shock fronts.

ticles due to the first-order Fermi mechanism (see section 1.2.3). These shocks should form at an early stage of the wind to provide a sufficient amount of high energy particles to drive the wind. Fortunately, the first five shocks for the initial **Model A** merge at a height below ≈ 5 kpc, which is very close to the inner boundary (estimate made by extrapolation of the shock front evolutions). The shocks for **Model B** merge even faster, which one can see very clear in Figure 5.9. It has been already discussed in Dorfi & Breitschwerdt (2012), that the merged shock becomes very strong due to the steep density gradient and is therefore able to accelerate cosmic ray particles up to the energies needed for driving the galactic wind.

The time evolution of the galactic winds in the outer region (up to $z = 300$ kpc) is virtually indistinguishable for different diffusion coefficients κ and is shown in Figure 5.10.

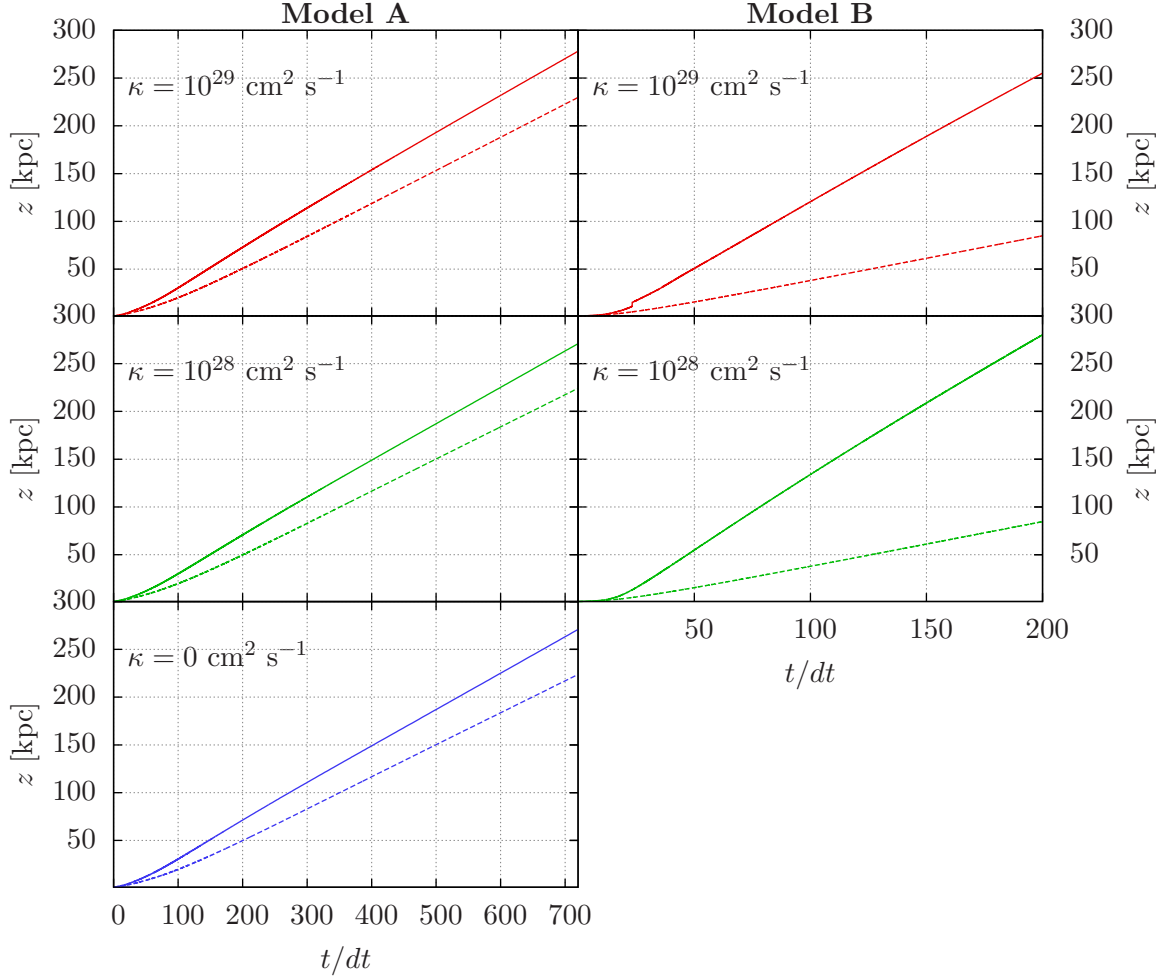


Figure 5.10: The time evolution (distance z plotted against time t/dt , where dt is the time interval between two supernova explosions) for the merged forward and reverse shock is shown here for both initial models. The global time evolution of the shocks only varies very slightly (virtually indistinguishable with the naked eye) in the diffusion coefficient κ . The shock fronts separate much more for **Model B**, which is the expected result and can also be seen in Figures 5.3 and 5.6.

Note that in Figure 5.10 the time evolution of the galactic wind with $\kappa = 0 \text{ cm}^2 \text{ s}^{-1}$ for initial **Model B** is missing, which is due to the same reasons as in section 5.2. The bigger separation between the forward shock and the reverse shock in **Model B** is due to the higher shock velocities (with respect to **Model A**). Consequently the forward shock is much faster and the reverse shock runs inward with higher speed, resulting in a slower outward-directed convection.

The shock speed tends to an asymptotic value very fast, which can be seen clearly in

Figure 5.10. In the inner region (1.0 – 1.6 kpc) the velocity evolution of the shock velocities (for the first three shocks) is plotted in Figure 5.11.

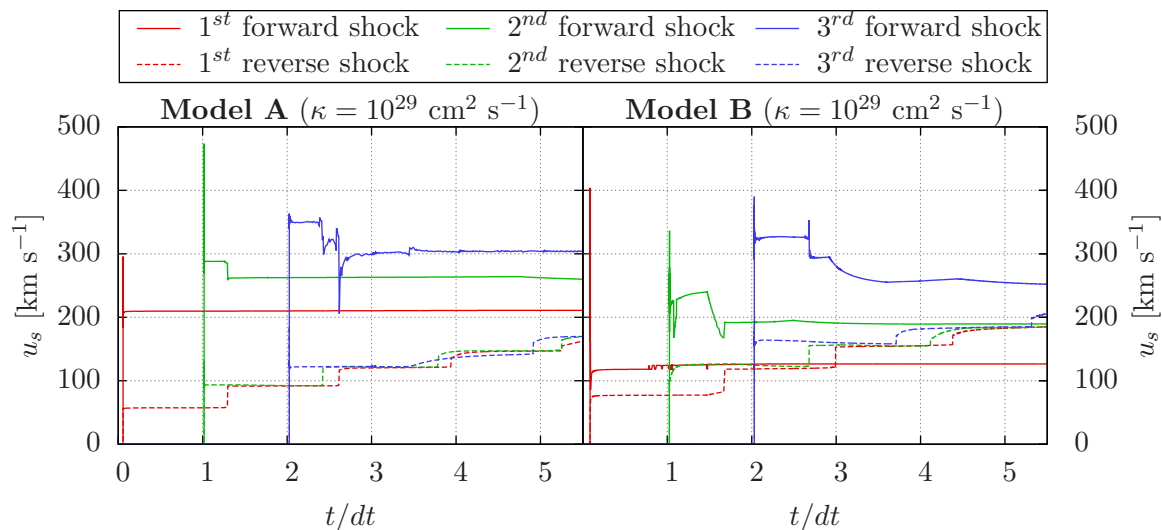


Figure 5.11: The shock front velocities are plotted for $\kappa = 10^{29} \text{ cm}^2 \text{ s}^{-1}$ (the qualitative behaviour for $\kappa = 0 \text{ cm}^2 \text{ s}^{-1}$ and $\kappa = 10^{28} \text{ cm}^2 \text{ s}^{-1}$ does not differ much from the shown plot) and for both initial models.

One can see in Figure 5.11, that the forward shocks and reverse shocks *exchange kinetic energy*; this can be seen very clearly e.g. in the velocity evolution of the second forward and the first reverse shot in the left plot (green full and red dashed line): When these shocks meet each other at $t \approx 1.2 dt$ (compare with 5.9, time evolutions for $\kappa = 10^{29} \text{ cm}^2 \text{ s}^{-1}$) then the forward shock slows down a bit, consequently the reverse shock receives the energy and gains speed. This behaviour is observable every time, a reverse shock meets a forward shock. Note that the inaccuracies in the velocity plots are purely from numerical origin. Every time a supernova explodes the corresponding shock waves are weaker than the shock before, therefore the grid equation (see section 3.1 for details) does not allocate so much points to properly describe the shock wave. Consequently every subsequent shock suffers from an increasing numerical dissipation, which results in inaccuracies in describing the time evolution and velocities of the shock wave.

The asymptotic velocities $u_{s,\infty}$ of the forward and reverse shocks (compare with Figure 5.10) are listed below in Table 5.5. The forward shock velocities in **Model B** are much higher than in **Model A**, which is due to the steeper density gradients (compare also with Figures 5.10). Although in the inner region close to the galactic disk the shock velocities of **Model B** are lower than for **Model A** (see Figure 5.9, the shock accelerates

		Model A	Model B
$\kappa = 10^{29} \text{ cm}^2 \text{ s}^{-1}$	$u_{s,\infty}$ [km s ⁻¹] (forward shock)	795	3180
	$u_{s,\infty}$ [km s ⁻¹] (reverse shock)	701	943
$\kappa = 10^{28} \text{ cm}^2 \text{ s}^{-1}$	$u_{s,\infty}$ [km s ⁻¹] (forward shock)	780	3065
	$u_{s,\infty}$ [km s ⁻¹] (reverse shock)	683	940
$\kappa = 0 \text{ cm}^2 \text{ s}^{-1}$	$u_{s,\infty}$ [km s ⁻¹] (forward shock)	777	—
	$u_{s,\infty}$ [km s ⁻¹] (reverse shock)	683	—

Table 5.5: Asymptotic shock velocities for the forward and reverse shocks and for both initial models. Because of the missing plot for $\kappa = 0 \text{ cm}^2 \text{ s}^{-1}$ and initial **Model B** the asymptotic velocities couldn't be determined.

much faster, which leads to the results which can be seen here. The asymptotic behaviour has been already explained by Dorfi & Breitschwerdt (2012), who explain it by assuming that the galactic wind is similar to a stella wind type. which propagates to a certain distance z_s ,

$$z_s \propto t^{\frac{3}{5+\beta}}, \quad (5.2.6)$$

where β is the exponent of the density profile, especially $\rho \propto z^\beta$. If one makes the assumption that the asymptotic wind speed is reached rather fast, which is indeed the case (compare with Figure 4.3 or 5.3), then the density profile $\rho(z)$ can be written as follows (with help of equation 2.11.1),

$$\rho(z) \propto (u(z) A(z))^{-1} \propto z^{-2}, \quad (5.2.7)$$

where $u(z)$ is the galactic wind velocity profile. Consequently $\beta = -2$, which leads to $z_s \propto t$. If the shock speed u_s is determined by differentiation one obtains,

$$u_s = \frac{dz_s}{dt} = \text{const.} \quad (5.2.8)$$

5.3 Feedback of the wind on the superbubble

The next step in obtaining a more physical insight in the physics of galactic winds is the consideration of the feedback of the galactic wind on the superbubble in the galactic mid-plane. The wind transports mass, which results in a mass loss in the superbubble

(approximated by the Kompaneets solution, see section 1.3). Hence, quantities like density ρ and the pressure components p_g and p_c will decrease at the inner boundary due to mass loss in the superbubble. In summary a superposition of two effects will then determine the boundary conditions:

- the increase of p_g and p_c due to the explosion of supernovae, and
- the decrease of p_g , p_c and ρ due to the mass loss of the superbubble caused by the galactic wind.

Therefore, referring to section 3.4.1, the loss terms $E_{g,loss}$, $E_{c,loss}$ and ρ_{loss} are *non-vanishing* terms and contribute in determining the boundary conditions (in contrast to the sections before).

The numerical parameters which have been used for the computation, are listed in Table 5.6.

	N	l_q	τ	q_1	q_2	g_ρ	g_u	g_{p_g}	g_{p_c}	g_{p_w}	g_z
Model A (inner region)	2000	z	$1.0 \cdot 10^8$	0	10^{-4}	1	0	1	1	0.1	0
Model B (inner region)	2000	z	$1.0 \cdot 10^8$	0	10^{-3}	1	0	1	1	0.1	0
Model A (outer region)	1000	z	$1.0 \cdot 10^6$	0	10^{-3}	1	0	1	0	0	0
Model B (outer region)	1000	z	$2.0 \cdot 10^8$	0	10^{-3}	1	0	0.1	1	0.1	0

Table 5.6: Numerical parameters used for the simulations of the galactic wind for $\kappa = 10^{29} \text{ cm}^2 \text{ s}^{-1}$ and with mass loss.

The following simulations have been calculated with $\kappa = 10^{29} \text{ cm}^2 \text{ s}^{-1}$ and are shown in 5.12. The inner region plot does not really differ from the corresponding simulation without mass loss (compare with Figure 5.2). This is because the shock propagation time t is still pretty short ($t = 2.4 \cdot 10^6$ years), but the mass loss \dot{M} obviously is proportional to the elapsed time and the wind velocity u , especially $\dot{M} \propto t \cdot u$. Furthermore the mass loss rate is time-dependent, because the wind velocity u also changes in time, as well as the gas density ρ . Hence it is evident that the effects of a wind feedback on the superbubble become visible at *longer propagation times* and an outer region plot also makes sense (shown in Figure 5.13), as it reveals the changes to the flow topology by the wind feedback.

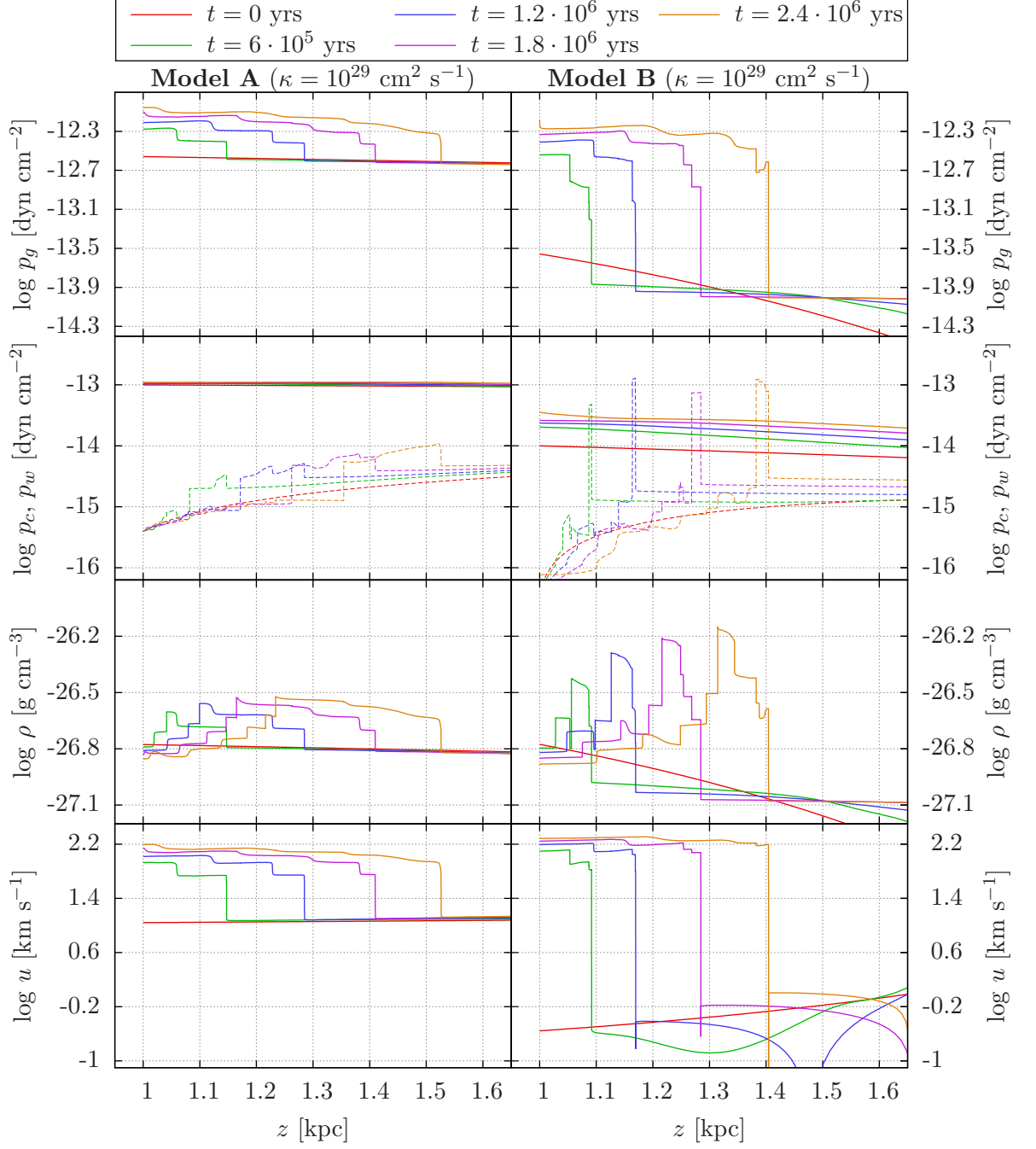


Figure 5.12: Various pressure profiles p_g , p_c and p_w as well as the density profile ρ and the gas velocity profile u at five different times (see legend) for the two different models **Model A** and **Model B** as well as wind feedback on the superbubble. The CR pressure profile and the wave pressure profiles (dashed lines) are shown in the same plot.

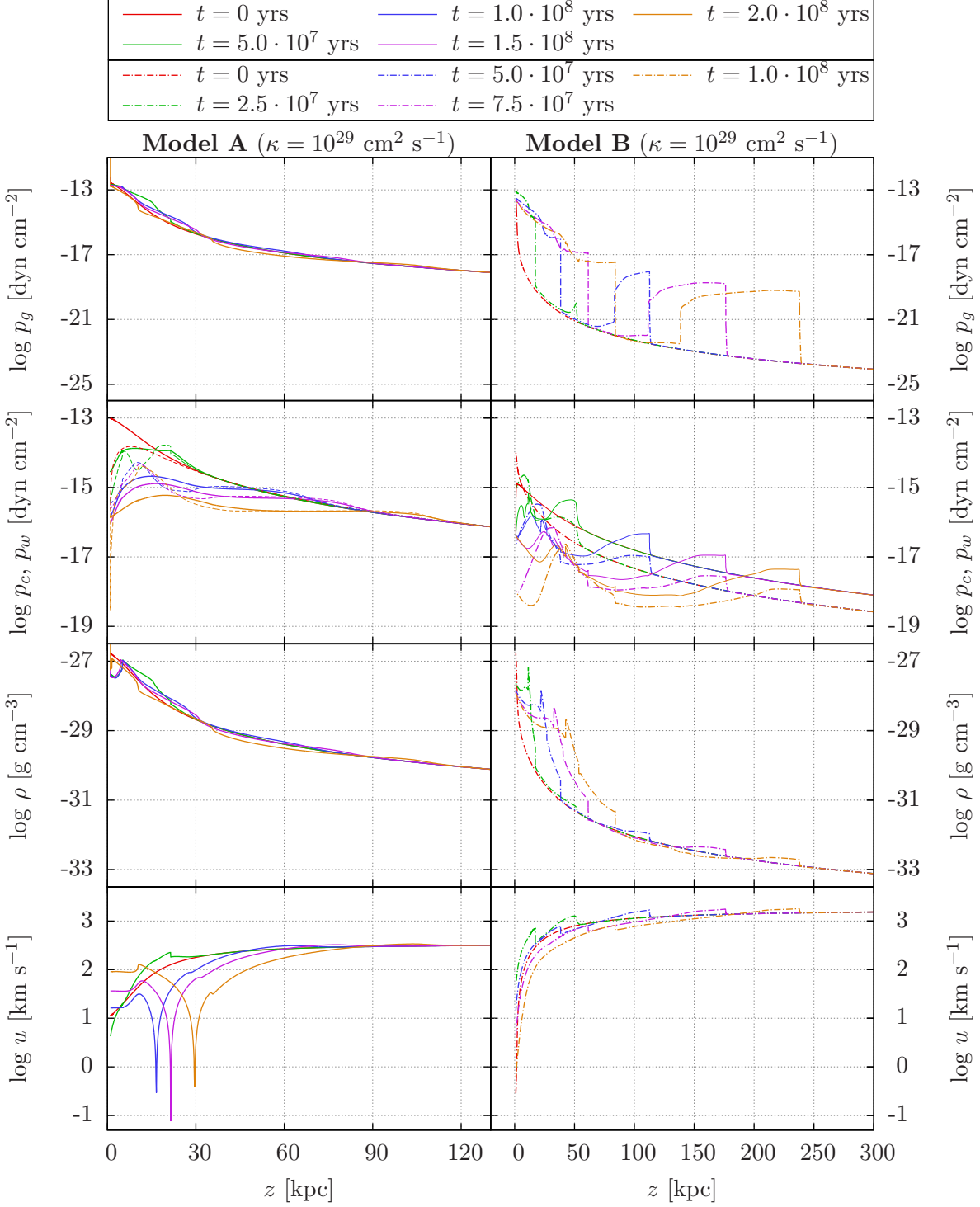


Figure 5.13: Various pressure profiles p_g , p_c and p_w as well as the density profile ρ and the gas velocity profile u at five different times (see legend) for the two different models **Model A** and **Model B**. The CR pressure profile and the wave pressure profiles (dashed lines) are again shown in the same plot.

Some interesting, different features (with respect to simulations without feedback, compare e.g. with Figure 5.3) can be seen here. Steep cosmic ray pressure gradients are forming near the inner boundary for both initial models. These gradients lead to the conclusion that the diffusion is not sufficient to compensate the advective losses of the CRs in the superbubble, more precisely this means that the advective part of the cosmic ray flux in equation (2.6.2) is much higher than the diffusive part, which would tend to flatten the gradient but is not strong enough to succeed. The simulation program has been written in a way, that it does not allow lower values for p_c than 10^{-18} dyn cm $^{-2}$. The reason for this is, that lower values don't have any physical relevance, because even the most depleted superbubble gets penetrated by an certain amount of extragalactic CRs and has therefore a certain very low cosmic ray pressure component. This explains, why the CR pressure profile is fixed at the inner boundary at $p_c = 10^{-18}$ dyn cm $^{-2}$ for **Model B** (look at the orange dot-dashed line).

Another feature can be seen in the velocity plots for **Model A**. The wind velocity nearly vanishes at some distance (e.g. at $z \approx 30$ kpc for **Model A** and $t = 2.0 \cdot 10^8$ years), which seems to be a feature caused by a combination of two phenomena: first the reverse shock, which accelerates the gas component, and second the steep positive CR pressure gradient which is the dominant pressure contribution and causes the gas component to slow down. Together these features could explain (in a heuristic, simplified manner) the slow velocity peaks. Note that the simulation terminated for **Model A** after approximately $t = 2.0 \cdot 10^8$ years, which is probably because of those peaks in the velocity profile. It also is possible that the wind cannot propagate any further because of too flat gradients in the CR pressure profile (which is the case, compare with Figure 5.13).

It is also remarkable, that the wind is able to propagate further outwards for **Model B** (compared to **Model A**). The reasons are very likely the steeper gradients of the undisturbed medium, which allow the wind to speed up more (as it has been discussed in section 5.2.1) and then is able to blow further out. One can see that the gas velocity u of the wind also slows down in **Model B**, and the shock fronts become weaker when propagating in time. This goes on, until the shock fronts are 'eaten up' and the galactic wind terminates.

The time evolution of the shock fronts is shown in Figure 5.14. Note that the time evolution in the inner region will not be plotted here, since the effects of the wind

feedback are not really visible in this region.

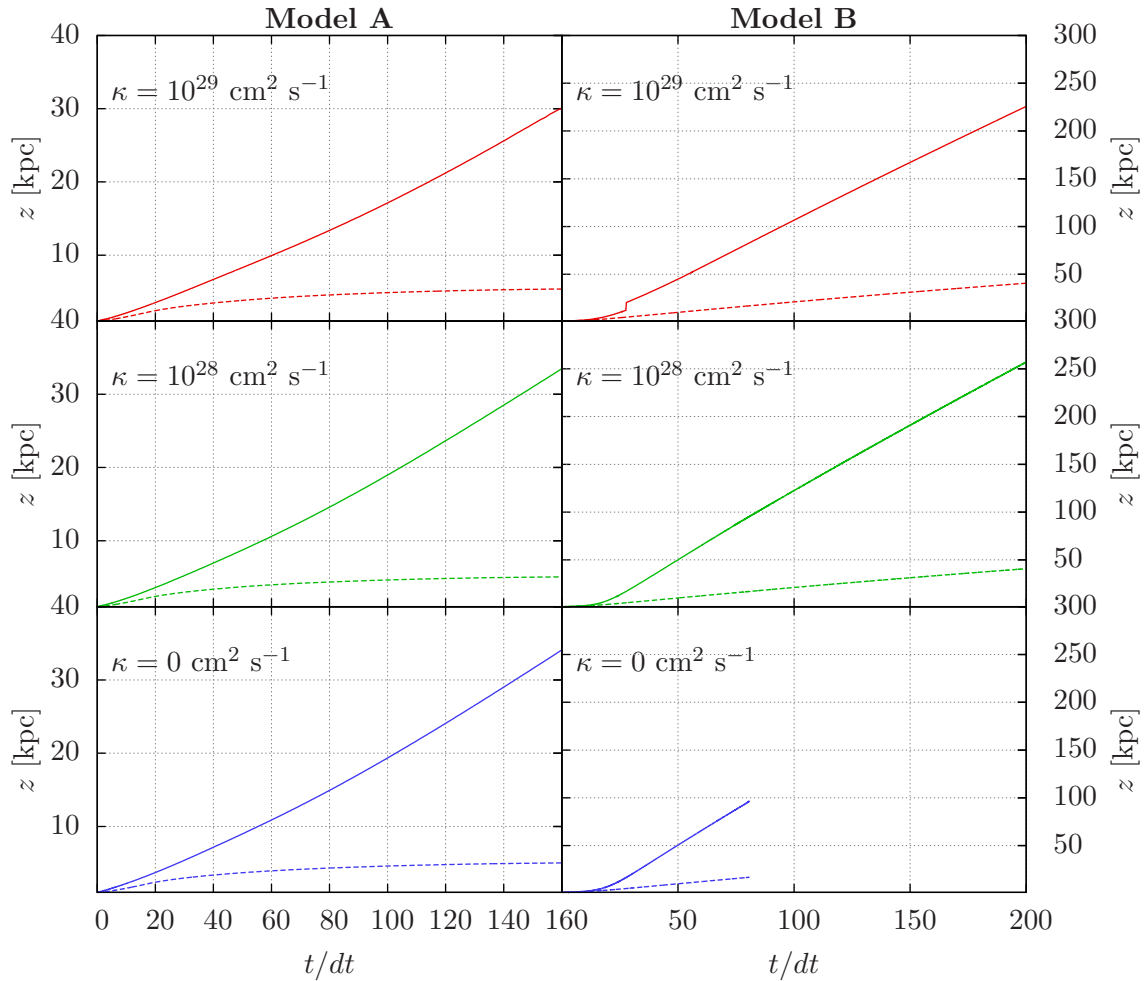


Figure 5.14: The evolution of the shock fronts is plotted here for three different diffusion coefficients κ and for galactic wind feedback for both initial models A and B.

One can see in Figure 5.14, that the reverse shocks for **Model A** slow down until they don't really move anymore. This can be explained by looking at the velocity plots of Figure 5.13 again. There the velocity drops significantly in the region of the reverse shocks, this means that the shock is not so fast convected with the flow anymore and therefore slows down (since the reverse shock tends to run inward). In contrast to this behaviour the reverse shocks for **Model B** still show the same behaviour as they do in simulations without mass loss and are propagated outwards with the flow. The only difference compared to the simulation without mass loss is the slower propagation of the reverse shocks (compare with Figure 5.10). It is also noticeable that there are virtually

no differences between the simulations with different diffusion coefficient (which is the reason why the flow features for $\kappa = 10^{28} \text{ cm}^2 \text{ s}^{-1}$ and $\kappa = 0 \text{ cm}^2 \text{ s}^{-1}$ are not shown in this section, since no additional features can be seen in these simulations).

6 Numerical difficulties and conclusion

In this section the numerical difficulties which occurred during the simulations are discussed briefly. Furthermore the results presented in section 5 are summarized and some conclusions are derived.

6.1 Numerical difficulties

During the simulations some difficulties occurred. One problem which arises for every computational simulation of an astrophysical problem (not only for the simulations made in this thesis) are the issue of the many orders of magnitudes of the quantities which need to be covered. In the case of an implicit simulation code this results in problems while inverting the Jacobi matrix (for details, see section 3). It can occur, that during the inversion some values leave their value range (even for double precision), which emphasises the necessity of *matrix preconditioning* (see e.g. LeVeque et al. (1998) for further details). Nevertheless the matrix keeps bad preconditioned and this can lead to errors while inverting. Furthermore note that no straightforward matrix inversion method of the well known linear algebra packages (like LAPACK, BLAS, ...) is able to invert a *pentadiagonal block-matrix* effectively (at least as far as we know).

Another difficulty comes from the fact that the numerical program works with an iteration process to find the solution at the new time (a Newton-Raphson iteration). The simulations performed here deal with variable boundary conditions, which makes it necessary to not vary instantaneously, but with built in smoothing functions. But, as one can understand, this is a conflict of interests: On the one hand, the variations should be rather quick for simulation a supernova explosion, on the other hand the program will not be able to deal with such variations, since then the iteration will not find any convergent solution. Especially for the hydrostatic inner boundary conditions (**Model B**, see sections 3.4.1 and 5) the differences between the undisturbed medium and the onset wind are rather big, which made it difficult to fine-tune the parameters in a way

of getting good results.

Last but not least it can be said that doing simulations with an implicit code require a good understanding of the underlying physics and the code. Furthermore the parameters need lots of fine-tuning and nursing and requires experience in doing such simulations, since a slightly different parameter can result in a non-invertible (singular) matrix.

6.2 Conclusions

Various authors have already discussed the importance of CRs for the evolution of galactic winds. This thesis can be seen as a further investigation of galactic winds, as it has been done by Dorfi & Breitschwerdt (2012). They have concluded that the observed cosmic ray energies (energies between the 'ankle' and the 'knee') could be explained by acceleration of cosmic ray particles in shock waves due to the first-order Fermi mechanism (see section 1.2.3 for further details).

Further it has been shown in magnetohydrodynamical 3D-simulations (de Avillez & Breitschwerdt (2005)), that winds can occur even in thick disks where they normally wouldn't be expected to exist. This comes from the mechanism, that a locally thermalized region (e.g. a superbubble) in the disk can push aside the surrounding halo material and then start to stream into the outer halo, while still accelerating due to pressure and density gradients. When the wind has propagated sufficiently far away from the galactic disk, the cosmic ray pressure contribution becomes dominant and drives the wind further outward.

This thesis (among others) deals with the modulation of such wind structures by the *star formation rate*. If a group of massive stars in an OB-association blows up as subsequent supernovae, they probably will form a superbubble. The disk-halo connection is implemented as it has been done by Dorfi & Breitschwerdt (2012), namely by varying the inner boundary conditions (see section 3.4.1). In contrast to Dorfi & Breitschwerdt (2012), this thesis simulates a sequence of supernovae (as it is in an OB-association) by an incremental increase of the inner boundary conditions. It is investigated how these shock waves evolve in time as well as the behaviour when two shocks meet each other. An emphasis lies on the determination of the scale above the galactic midplane, at which the shock fronts merge and form a single strong shock. This is interesting in

the context of wind acceleration by CRs, because the observed energy spectra reveal that CRs are already at high energies close to the disk, which is only possible with a further acceleration mechanism (in this thesis as well as in Dorfi & Breitschwerdt (2012) this mechanism is assumed to be the first-order Fermi mechanism). Another focus lies on the investigation of time-dependent flow features. Multiple shock structures as well as contact discontinuities become visible in the various pressure and density profiles. Furthermore all galactic wind simulations are performed for two different initial models. First, the inner boundaries of an already existing wind are varied and its effect on the wind is investigated. A more physical initial situation is the absence of a wind before the superbubble expands out of the disk. Hence an initial model is used, which approximately imitates this situation.

Moreover the attempt of physically better motivated inner boundaries has been made. The qualitative effect of varying inner boundaries on the galactic wind can be investigated by just increasing them by a certain value (as it has been done by Dorfi & Breitschwerdt (2012)), but this value is completely arbitrary and has no support from the physical processes involved. The Kompaneets approximation (explained in section 1.3) solves this problem in a highly approximative, but elegant and simple way. As mentioned before in this work, a higher level of accuracy makes no sense, since the underlying physical model itself comes with rough approximations.

Finally, the work and results obtained in this thesis is summarized now:

- the Kompaneets approximation is used to model the superbubble and to obtain physically motivated values for the gas pressure p_g , the cosmic ray pressure p_c and the density ρ ,
- variations of the inner boundary lead to characteristic flow features, more precisely *forward shocks*, *reverse shocks* and *contact discontinuities* which propagate along the density gradient outward with respect to the galactic disk,
- subsequent forward shock waves will merge to a single, strong shock wave, which then further steepens while running down the density gradient,
- the merging scaleheight $z_{scale} \approx 5$ kpc, which is very close to the disk and hence is supporting the theory of early accelerated CRs, which then drive the wind outwards,

- the effect of galactic feedback on the superbubble is investigated; it is revealed that the forward shocks get weaker and weaker then, until the wind is not able to blow out further and terminates. In the case of a hydrostatic halo model (more realistic than the modulation of an existing wind) the shocks are able to blow further outwards.
- the effect of the diffusion coefficient κ is investigated. Higher diffusion leads to flattened flow features and a flatter cosmic ray pressure profile.

Bibliography

- J.E. Anderson. *Magnetohydrodynamic Shock Waves*. MIT Press Classics. MIT Press, 1963. ISBN 9780262511599. URL <http://books.google.at/books?id=hH7IGwAACAAJ>.
- W. I. Axford, E. Leer, & G. Skadron. The acceleration of cosmic rays by shock waves. In *International Cosmic Ray Conference*, volume 11 of *International Cosmic Ray Conference*, pages 132–137, 1977.
- A. R. Bell. The acceleration of cosmic rays in shock fronts. I. *MNRAS*, 182:147–156, January 1978.
- E. G. Berezhko & H. J. Völk. Kinetic theory of cosmic ray and gamma-ray production in supernova remnants expanding into wind bubbles. *A&A*, 357:283–300, May 2000.
- E. G. Berezhko & H. J. Völk. Theory of cosmic ray production in the supernova remnant RX J1713.7-3946. *A&A*, 451:981–990, June 2006. doi: 10.1051/0004-6361:20054595.
- G. S. Bisnovatyi-Kogan & S. A. Silich. Shock-wave propagation in the nonuniform interstellar medium. *Reviews of Modern Physics*, 67:661–712, July 1995. doi: 10.1103/RevModPhys.67.661.
- R. D. Blandford & J. P. Ostriker. Particle acceleration by astrophysical shocks. *ApJ*, 221:L29–L32, April 1978. doi: 10.1086/182658.
- R. Boomsma, T. A. Oosterloo, F. Fraternali, J. M. van der Hulst, & R. Sancisi. Extraplanar H I in the starburst galaxy NGC 253. *A&A*, 431:65–72, February 2005. doi: 10.1051/0004-6361:20041715.
- D. Breitschwerdt, J. F. McKenzie, & H. J. Voelk. Galactic winds. I - Cosmic ray and wave-driven winds from the Galaxy. *A&A*, 245:79–98, May 1991.
- D. Breitschwerdt, M. A. de Avillez, & V. Baumgartner. Modeling the Local Warm/Hot Bubble. *THE LOCAL BUBBLE AND BEYOND II: Proceedings of the International*

- Conference. *AIP Conference Proceedings, Volume 1156, pp. 271-279 (2009).*, 1156: 271–279, August 2009. doi: 10.1063/1.3211826.
- J. A. Burke. Mass flow from stellar systems-I. Radial flow from spherical systems. *MNRAS*, 140:241, 1968.
- C. J. Cesarsky. Cosmic-ray confinement in the galaxy. *ARA&A*, 18:289–319, 1980. doi: 10.1146/annurev.aa.18.090180.001445.
- M. A. de Avillez & D. Breitschwerdt. Global dynamical evolution of the ISM in star forming galaxies. I. High resolution 3D simulations: Effect of the magnetic field. *A&A*, 436:585–600, June 2005. doi: 10.1051/0004-6361:20042146.
- E. A. Dorfi & D. Breitschwerdt. Time-dependent galactic winds. I. Structure and evolution of galactic outflows accompanied by cosmic ray acceleration. *A&A*, 540:A77, April 2012. doi: 10.1051/0004-6361/201118082.
- E. A. Dorfi & L. O. Drury. Simple adaptive grids for 1-D initial value problems. *Journal of Computational Physics*, 69:175–195, March 1987. doi: 10.1016/0021-9991(87)90161-6.
- D. Downes & R. Guesten. Radio studies of galactic structure. *Mitteilungen der Astronomischen Gesellschaft Hamburg*, 57:207–232, 1982.
- M. Ehle, W. Pietsch, R. Beck, & U. Klein. ROSAT PSPC X-ray observations of the nearby spiral galaxy M 83. *A&A*, 329:39–54, January 1998.
- D. C. Ellison & J.-P. Meyer. The Origin of the Present Day Cosmic Rays (II). In R. Ramaty, E. Vangioni-Flam, M. Cassé, & K. Olive, editors, *LiBeB Cosmic Rays, and Related X- and Gamma-Rays*, volume 171, page 207, 1999.
- J. Everett. The pressure's on: Cosmic-ray pressure in galactic winds. University Lecture, "http://www.cmso.info/cmsopdf/CMSO_gen_mtg_apr09/Everett_winds-SF09.pdf", 2009. [Online; accessed 07-June-2012].
- J. E. Everett, E. G. Zweibel, R. A. Benjamin, D. McCammon, L. Rocks, & J. S. Gallagher, III. The Milky Way's Kiloparsec-Scale Wind: A Hybrid Cosmic-Ray and Thermally Driven Outflow. *ApJ*, 674:258–270, February 2008. doi: 10.1086/524766.

- ENRICO Fermi. On the origin of the cosmic radiation. *Phys. Rev.*, 75:1169–1174, Apr 1949. doi: 10.1103/PhysRev.75.1169. URL <http://link.aps.org/doi/10.1103/PhysRev.75.1169>.
- M. Feuchtinger. Strahlungshydrodynamische Modellrechnungen für Sterne am asymptotischen Riesenast, Diplomarbeit, University of Vienna, 1989.
- K. A. Innanen. Models of Galactic Mass Distribution. *Ap&SS*, 22:393–411, June 1973. doi: 10.1007/BF00647434.
- F. M. Ipavich. Galactic winds driven by cosmic rays. *ApJ*, 196:107–120, February 1975. doi: 10.1086/153397.
- H. E. Johnson & W. I. Axford. Galactic Winds. *ApJ*, 165:381, May 1971. doi: 10.1086/150903.
- D.W. Jordan & P. Smith. *Nonlinear Ordinary Differential Equations: An Introduction for Scientists and Engineers*. Oxford applied and engineering mathematics. Oxford University Press, 2007. ISBN 9780199208258. URL http://books.google.at/books?id=FmIS_OUEAUAC.
- F. D. Kahn. Dynamics of the galactic fountain. In F. D. Kahn, editor, *Investigating the Universe*, volume 91 of *Astrophysics and Space Science Library*, pages 1–28, 1981.
- F. D. Kahn. Introduction to fountains, wind, infall - and magnetic fields and dynamo mechanisms. In H. Bloemen, editor, *The Interstellar Disk-Halo Connection in Galaxies*, volume 144 of *IAU Symposium*, pages 1–11, 1991.
- F. D. Kahn. The Galactic Fountain. In D. Breitschwerdt, M. J. Freyberg, & J. Truemper, editors, *IAU Colloq. 166: The Local Bubble and Beyond*, volume 506 of *Lecture Notes in Physics*, Berlin Springer Verlag, pages 483–494, 1998. doi: 10.1007/BFb0104770.
- A. S. Kompaneets. A Point Explosion in an Inhomogeneous Atmosphere. *Soviet Physics Doklady*, 5:46, July 1960.
- G. F. Krymskii. A regular mechanism for the acceleration of charged particles on the front of a shock wave. *Akademiia Nauk SSSR Doklady*, 234:1306–1308, June 1977.
- K. Kulpa-Dybeł, K. Otmianowska-Mazur, B. Kulesza-Żydzik, M. Hanasz, G. Kowal, D. Wóltański, & K. Kowalik. Global Simulations of the Magnetic Field Evolution in

- Barred Galaxies Under the Influence of the Cosmic-ray-driven Dynamo. *ApJ*, 733:L18, June 2011. doi: 10.1088/2041-8205/733/2/L18.
- R.J. LeVeque. *Numerical Methods for Conservation Laws*. Lectures in Mathematics ETH Zürich. Birkhäuser Verlag, 1992. ISBN 9783764327231. URL <http://books.google.at/books?id=3WhqLPcMdPsC>.
- R.J. LeVeque, D. Mihalas, E.A. Dorfi, E. Müller, O. Steiner, & A. Gautschy. *Computational Methods for Astrophysical Fluid Flow: Saas-Fee Advanced Course 27. Lecture Notes 1997 Swiss Society for Astrophysics and Astronomy*. Saas-Fee Advanced Courses. Springer, 1998. ISBN 9783642084126. URL <http://books.google.at/books?id=emgMkgAACAAJ>.
- M.S. Longair. *High Energy Astrophysics*. Cambridge University Press, 2011. ISBN 9780521756181. URL <http://books.google.at/books?id=KGe3FVbDNk4C>.
- T.A. Lozinskaia & T.A. Lozinskaia. *Supernovae and Stellar Wind in the Interstellar Medium*. Translation Series. American Institute of Physics, 1992. ISBN 9780883186596. URL <http://books.google.at/books?id=dMfSPaPdlbwC>.
- C. R. Lynds & A. R. Sandage. Evidence for an Explosion in the Center of the Galaxy M82. *ApJ*, 137:1005, May 1963. doi: 10.1086/147579.
- D. P. Maciejewski W., Cox. Supernova remnant in a stratified medium: Explicit, analytical approximations for adiabatic expansion and radiative cooling. *Nature*, 452(7189): 826–827, April 1998. ISSN 0028-0836. doi: 10.1038/452826a. 10.1038/452826a.
- W. G. Mathews & J. C. Baker. Galactic Winds. *ApJ*, 170:241, December 1971. doi: 10.1086/151208.
- D. Mihalas & B.W. Mihalas. *Foundations of Radiation Hydrodynamics*. Dover Books on Physics. Dover, 1999. ISBN 9780486409252. URL http://books.google.at/books?id=f75C_GN9KZwC.
- M. Miyamoto & R. Nagai. Three-dimensional models for the distribution of mass in galaxies. *PASJ*, 27:533–543, 1975.
- E. N. Parker. The Dynamical State of the Interstellar Gas and Field. *ApJ*, 145:811, September 1966. doi: 10.1086/148828.
- G. Ramberger. Galaktische Winde, Diplomarbeit, University of Vienna, 2008.

- D.D. Schnack. *Lectures in Magnetohydrodynamics: With an Appendix on Extended MHD*. Lecture Notes in Physics. Springer, 2009. ISBN 9783642006876. URL <http://books.google.com/books?id=Ebon7NTbL0EC>.
- L. I. Sedov. Examples of Gas Motion and Certain Hypotheses on the Mechanism of Stellar Outbursts. *Reviews of Modern Physics*, 30:1077–1079, July 1958. doi: 10.1103/RevModPhys.30.1077.
- J. Skilling. Cosmic ray streaming. I - Effect of Alfvén waves on particles. *MNRAS*, 172: 557–566, September 1975.
- K.S. Stowe. *An Introduction to Thermodynamics And Statistical Mechanics*. Cambridge University Press, 2007. ISBN 9780521865579. URL <http://books.google.com/books?id=BCuNTP07A10C>.
- W. M. Tscharnuter & K.-H. A. Winkler. A method for computing selfgravitating gas flows with radiation. *Computer Physics Communications*, 18:171–199, 1979. doi: 10.1016/0010-4655(79)90111-5.
- S. Veilleux, G. Cecil, & J. Bland-Hawthorn. Galactic Winds. *ARA&A*, 43:769–826, September 2005. doi: 10.1146/annurev.astro.43.072103.150610.
- J. Vonneumann & R. D. Richtmyer. A Method for the Numerical Calculation of Hydrodynamic Shocks. *Journal of Applied Physics*, 21:232–237, March 1950. doi: 10.1063/1.1699639.

Daniel Steiner

Curriculum Vitae



Personal Data

Birth Date	October 24, 1986 , <i>Linz, Austria.</i>
Nationality	Austria.
Confession	Roman Catholic.
Parents	Wilhelm Alexander Steiner Barbara Maria Steiner , <i>maiden name: Wolfmayr.</i>
Brothers and Sisters	one sister , <i>24 years old.</i>
Civil Status	unmarried.

Education

1992–1996	Volksschule , <i>Niederwaldkirchen.</i>
1996–2000	Hauptschule , <i>Niederwaldkirchen.</i>
2000–2005	HTBLA , <i>Neufelden</i> , Emphasis on Betriebsinformatik, Matura with evaluation 'good'.
2006–2010	University of Vienna , <i>Study program 'Bachelor Astronomy'</i> , Graduating with excellence.
2007–2010	University of Vienna , <i>Study program 'Bachelor Physics'</i> , Graduating with excellence.
2010–2012	University of Vienna , <i>Study program 'Master Astronomy'</i> , Graduating with excellence.
2010–2012	University of Vienna , <i>Study program 'Master Physics'</i> .

Additional information

- Stay abroad from 2009 July to 2010 January in Chile as an Exchange Student (attended courses in Physics and Astronomy)